6-2023

THE MOBILITY OF LONG-LIVED RADIOISOTOPES AND THEIR BURIAL IN THE MARINE ENVIRONMENT

Neil Redmond

THE MOBILITY OF LONG-LIVED RADIOISOTOPES AND THEIR BURIAL IN THE MARINE ENVIRONMENT

by

Neil Redmond

A Dissertation
Submitted to the Graduate School,
the College of Arts and Sciences
and the School of Ocean Science and Engineering
at The University of Southern Mississippi
in Partial Fulfillment of the Requirements
for the Degree of Doctor of Philosophy

Committee:

Dr. Christopher T. Hayes, Committee Chair
Dr. Alan M. Shiller
Dr. Davin J. Wallace
Dr. Denis A. Wiesenburg
Dr. Franco Marcantonio

August 2023

Published by the Graduate School

ABSTRACT

Marine sediments record chemical signals that reflect past environmental conditions. It is important to establish how these signals are created and whether they may be altered over time so that they can be useful for reconstructing ocean history. Measurements of uranium isotopes are used as a novel proxy for sedimentary diagenetic processes (Chapter 2). Because ^{234}U can be ejected from mineral lattice during the decay of ^{238}U, it creates a pool of U in porewater that is potentially mobilized and then deposited elsewhere in the core. We found that alpha-recoiled ^{234}U is sensitive to differences in sediment redox condition and will diffuse from core segments of low reducing capacity and reprecipitate at core segments deposited during glacial-interglacial transitions where organic matter delivery was higher. While our data is consistent with this model, calculations suggest there is also an additional source of excess ^{234}U at deglacial segments that is unaccounted for. Dissolved water column measurements of ^{230}Th and ^{231}Pa were taken in the open North Pacific (Chapter 3) along the 152° meridian and at the northern Mid-Atlantic Ridge (Chapter 4). These elements are prone to strong scavenging by marine particles, although, because of their differing solubilities, they are distributed by marine processes to different degrees. In the Pacific, ^{230}Th and ^{231}Pa were used to investigate the primary processes driving particle scavenging including productivity fronts, hydrothermal activity, and benthic resuspension. Strong regional contrasts in scavenging intensity were evaluated for potential impact to ^{230}Th as a paleoceanographic proxy of burial flux. It was found that hydrothermally influenced waters significantly impacted the expected ^{230}Th transport between the Equatorial Particle Veil and subtropical gyres, which creates potential uncertainties in ^{230}Th reconstructions

over areas of the equatorial Pacific. This is one example of recent research showing how the distal effects of hydrothermal scavenging are potentially significant throughout basin-scales. For the Mid-Atlantic, we employ a novel strategy to predict background scavenging as a reference to infer the degree of scavenging by hydrothermal plumes. ^{230}Th and ^{231}Pa can be explained by dispersal of hydrothermal particles and were dependent on the timescale of dispersal vs. mixing with seawater.

ACKNOWLEDGMENTS

First, I would like to thank my adviser Dr. Christopher Hayes for his guidance and mentorship through this program. I would like to thank the University of Southern Mississippi and the Division of Marine Science. I would like to thank all members of the Hayes/Shiller lab group for our work together. I would like to thank Melissa Gilbert for expertise with the ICP-MS. I would like to thank my committee members for their efforts and feedback. I would like to thank our colleagues at the Anderson lab group at LDEO, the Th/Pa team at UMN, and many coauthors who have made these projects possible. I would like to thank the National Science Foundation for funding these projects and the GEOTRACES program for samples and project management.

DEDICATION

To my baby daughter Elena, my wife Gianna, and the family who worked to make this happen.

TABLE OF CONTENTS

LIST OF TABLES

LIST OF ILLUSTRATIONS

CHAPTER I – PREFACE ON THE PALEOCEANOGRAPHIC IMPLICATIONS FOR THE MOBILITY OF LONG-LIVED RADIONUCLIDES

1.1 Introduction

1.1.1 Radiochemical Systems as Paleoceanographic Proxies

This dissertation focuses on U, Th, and Pa as a series of interrelated, long-lived radioisotopes. Although each chapter will examine part of this system in isolation, these elements are controlled by the same global, rock cycle processes before predominantly taking differing roles in the marine environment (Broecker & Peng, 1982; Hester et al., 2007). An understanding of each part of these radioactive chains affects our understanding of the others and, in a way, helps to apply our knowledge of these systems to the large-scale geochemical system.

U is among the rarer elements on Earth and yet, this low abundance is important to a wide array of geochemical processes. Of U's three natural isotopes, ^{238}U and ^{235}U are primordial, incorporated into Earth's crustal composition during planetary accretion, and ^{234}U is a natural decay product of ^{238}U (Hester et al., 2007). U primarily enters the marine system by weathering of continental material and due to its solubility, becomes a long-lived, trace component of sea salt found in roughly the same concentration everywhere in the ocean's oxygenated waters (Anderson & Burckle, 2009; Ku et al., 1997). Global inputs and outputs of U are stable over long geologic periods (its residence time is ~400 kyr) (Esat & Yokoyama, 2006) meaning that for many paleoceanographic applications, U concentrations and its isotopes can be treated as relatively constant. This consistency carries over to two of its isotope's long-lived daughters, ^{230}Th and ^{231}Pa, in that, the decay of ubiquitous U produces predictable inputs of daughter isotopes into the ocean

(Andersen et al., 2010; Bourdon et al., 2003; Delanghe et al., 2002; Robinson et al., 2004; Weyer et al., 2008). The parent-daughter U isotope systems are unique in that they can inform us both about the rate and the timescale of the processes for which they are involved (Henderson & Anderson, 2003). In the time between entering the marine system and leaving it by burial or decay, the extreme difference in solubility between U, Th, and Pa separates these elements, causing them to be buried on differing timescales and by differing environmental processes. For example, the burial of U is primarily a result of precipitation as low oxygen bottom waters overlies sediment (Henderson & Anderson, 2003), so changes to sedimentary U can reflect burial changes on the timescale of bottom ventilation (Francois et al., 1993; Hayes et al., 2014). Alternatively, ^{230}Th and ^{231}Pa are predominantly buried via scavenging, or the adsorption of elements onto sinking marine particles (Bourdon et al., 2003; Broecker & Peng, 1982; Goldberg, 1954). Their extreme "stickiness" results in relatively quicker burial, less than 200 years (Anderson et al., 1983; Bacon & Anderson, 1982), and is sensitive to changes in ocean particles on timescales of this magnitude. The relative solubility between these elements can separate them even when their general chemistry is very similar. For example, Pa is slightly more soluble than Th, leading to the expectation that Th will generally bury in place whereas Pa can mobilize to a degree (Henderson & Anderson, 2003; Hester et al., 2007). This difference in mobility between Th and Pa can affect their relative distribution, which is potentially useful in showing certain environmental processes such as boundary scavenging (Bacon et al., 1976; Spencer et al., 1981) and overturning circulation. Ultimately, when we turn to marine sediment as an archive of these processes, the

differences between elements and how they are affected by environmental parameters is expressed by the distributions we measure.

1.1.2 Element Solubility and Mobility

In this dissertation, we discuss processes which alter the flux of elements in or out of a system in the context that these fluxes ultimately affect the dynamics of their burial. The general timeframe for the rearrangement of U and its daughters from continental crust to oceanic crust is relatively short compared to its lifetime within each of these reservoirs (Broecker & Peng, 1982). In a way, the mineralization of these elements during formation or precipitation "lock" them into place and as part of Earth's crust, the opportunities to vary spatially due to environmental processes become limited. It is in this context, elements are released by the weathering and runoff of continental rocks, have a brief period in which these elements are shifted around by marine processes, and are again locked as oceanic sediment (Bruland et al., 2014; Hester et al., 2007). During this period between release and burial, we expect a combination of each element's solubility and marine processes to play a hand in redistributing these elements (Bruland et al., 2014; Henderson & Anderson, 2003), which is the foundation for using these elements as paleoproxies (Bourdon et al., 2003; Broecker & Peng, 1982; Hester et al., 2007). We often find that, on the basin-scale, multiple environmental processes are responsible for distribution of these radioelements. Each can broadly be categorized as (1) processes that change the relative solubility of the elements such as scavenging by ocean particles for Th/Pa or redox state for U, or (2) processes that control the rate of redistribution such as circulation or diffusive dispersal. The relationship between these factors is important because it acts as a push-and-pull, the solubility ultimately determines the downstream

extent elements can be redistributed before burial. Can we relate the degree an element mobilizes in the marine environment to physical processes controlling its distribution?

1.1.3 The Effects of Solubility and Redistribution at Different Scales

In this dissertation, we analyze marine mobilization at various scales for the suite of U, Th, and Pa. In Chapter 2, we observed a Southern Ocean core with anomalously high ratios of $^{234}U/^{238}U$ within and near deglacial transitions with areas of low $^{234}U/^{238}U$ surrounding them. These features are at least in part explained by ^{234}U being alpha-recoiled into sediment pore water, becoming soluble and free to mobilize in solution, diffusing meters through the core, and burying where stronger reducing conditions lower its solubility. In Chapter 3, we first use the distributions of ^{230}Th and ^{231}Pa in the Pacific basin to isolate different environmental processes that change the scavenging, and thereby solubility, of the elements by changes in particle concentration and composition. We identified that the distribution of these elements is mostly determined by biogenic particle input with overprinting effects from hydrothermal and benthic influences. We examine where ^{230}Th is potentially mobilized due to a strong contrast in concentration because of this feature and analyze potential paleoceanographic consequences. In Chapter 4, we use a novel method to predict ^{230}Th and ^{231}Pa distribution from our expectation from multiple environmental effects at the Mid-Atlantic Ridge, using the difference between modeled and observed distributions to infer the effects of hydrothermal particles. We found that the mixing time and dispersal of hydrothermal particles is an important control on ^{230}Th distribution within the axial valley. These controls are ultimately important for how depleted waters leak into the greater Atlantic, potentially causing hydrothermal scavenging effects to extend far from the ridge.

1.2 Works Cited

Andersen, M. B., Stirling, C. H., Zimmermann, B., & Halliday, A. N. (2010). Precise determination of the open ocean 234U/238U composition. *Geochemistry, Geophysics, Geosystems*, *11*(12). https://doi.org/10.1029/2010GC003318

Anderson, B. E., & Burckle, L. H. (2009). Rise in Atmospheric CO 2. *Science*, *323*(March), 1443–1448.

Anderson, R. F., Bacon, M. P., & Brewer, P. G. (1983). Removal of 230Th and 231Pa from the open ocean. *Earth and Planetary Science Letters*, *62*(1), 7–23.

Bacon, M. P., & Anderson, R. F. (1982). Distribution of Thorium Isotopes Between Dissolved and Particulate Forms in The Deep Sea. *Journal of Geophysical Research*, *87*(1), 2045–2056. https://doi.org/10.1029/JC087iC03p02045

Bacon, M. P., Spencer, D. W., & Brewer, P. G. (1976). 210Pb/226Ra and 210Po/210Pb disequilibria in seawater and suspended particulate matter. *Earth and Planetary Science Letters*, *32*, 277–296.

Bourdon, B., Turner, S., Henderson, G. M., & Lundstrom, C. C. (2003). Introduction to U-series geochemistry. In *Uranium-series Geochemistry* (Vol. 52, pp. 1–21). De Gruyter Mouton. https://doi.org/10.2113/0520001

Broecker, W. S., & Peng, T.-H. (1982). *Tracers in the Sea*.

Bruland, K. W., Middag, R., & Lohan, M. C. (2014). *Controls of Trace Metals in Seawater*. http://www.agu.org/eos_elec/97025e.html

Delanghe, D., Bard, E., & Hamelin, B. (2002). New TIMS constraints on the uranium-238and uranium-234 in seawaters from the main ocean basins and the Mediterranean Sea. *Marine Chemistry*, *80*, 79–93.

Esat, T. M., & Yokoyama, Y. (2006). Variability in the uranium isotopic composition of the oceans over glacial–interglacial timescales. *Geochimica et Cosmochimica Acta*, *70*(16), 4140–4150.

Francois, R., Bacon, M. P., Altabet, M. A., & Labeyrie, L. D. (1993). Glacial/interglacial changes in sediment rain rate in the SW Indian Sector of subantarctic Waters as recorded by 230Th, 231Pa, U, and δ15N. *Paleoceanography*, *8*(5), 611–629.

Goldberg, E. D. (1954). Marine Geochemistry 1. Chemical Scavengers of the Sea. *The Journal of Geology*, *62*(3), 249–265.

Hayes, C. T., Martínez-García, A., Hasenfratz, A. P., Jaccard, S. L., Hodell, D. A., Sigman, D. M., Haug, G. H., & Anderson, R. F. (2014). A stagnation event in the deep south atlantic during the last interglacial period. *Science*, *346*(6216), 1514–1517. https://doi.org/10.1126/science.1256620

Henderson, G. M., & Anderson, R. F. (2003). The U-series toolbox for paleoceanography. *Uranium-Series Geochemistry*, *52*, 493–531. https://doi.org/10.2113/0520493

Hester, R. E., Harrison, R. M., Swarzenski, P. W., Corbett, D. R., Smoak, J. M., & Mckee, B. A. (2007). The use of U–Th series radionuclides and transient tracers in oceanography: An overview. In *Chemistry in the Marine Environment* (pp. 33–54). The Royal Society of Chemistry. https://doi.org/10.1039/9781847550453-00033

Ku, T., Knauss, K., & Mathieu, G. (1997). Uranium in open ocean: concentration and isotopic composition. *Deep Sea Research*, *24*, 1005–1017.

Robinson, L. F., Belshaw, N. S., & Henderson, G. M. (2004). U and Th concentrations

and isotope ratios in modern carbonates and waters from the Bahamas. *Geochimica et Cosmochimica Acta*, *68*(8), 1777–1789. https://doi.org/10.1016/j.gca.2003.10.005

Spencer, D. W., Bacon, M. P., & Brewer, P. G. (1981). Models of the distribution of 210Pb in a section across the North Equatorial Atlantic Ocean. *Journal of Marine Research*, *39*, 119–138.

Weyer, S., Anbar, A. D., Gerdes, A., Gordon, G. W., Algeo, T. J., & Boyle, E. A. (2008). Natural fractionation of 238U/235U. *Geochimica et Cosmochimica Acta*, *72*, 345–359.

CHAPTER II – ANOMALOUS $^{234}U/^{238}U$ ISOTOPIC COMPOSITION IN SOUTHERN OCEAN SEDIMENTS

2.1 Abstract

Uranium is a redox-sensitive trace element that under certain sedimentary conditions will reflect changes in past biological productivity and/or deep ocean ventilation. The U concentration of pelagic sediment derives from authigenic U (aU) and detrital U. The U isotopic composition ($^{234}U:^{238}U$ activity ratio, $\delta^{234}U$ or the per mil deviation from secular equilibrium) of these two sources is fairly well constrained, leading to the expectation that $\delta^{234}U$ in pelagic sediment should be predictable with knowledge of the fraction of these two components. However, U records potentially reflect post-depositional changes, which ultimately complicate interpretation of U as a paleoredox proxy. $\delta^{234}U$ provides an avenue to explore U mobility during diagenesis; however, this relationship is relatively unexplored in deep ocean sediment. We present $\delta^{234}U$ of bulk U for a 504-kyr record of South Atlantic core ODP 1094, a record that has exhibited sensitivity to bottom water formation with minimal ^{238}U remobilization due to redox changes. We use a mixing model to predict sedimentary $\delta^{234}U$ given aU and detrital U sources and radioactive decay since burial for comparison to modern values. Comparatively, the observed $\delta^{234}U$ record displays sections of discrepancy from the model prediction, in particular surrounding aU enrichments, which in many cases exceed the $\delta^{234}U$ of seawater. The pattern of these anomalies may be consistent with the idea that deglacial spikes in aU, resulting from periods of high organic carbon delivery and thereby strong respiration, act as a persistent sink of ^{234}U alpha-recoiled from adjacent sediment after burial. We tested this hypothesis by performing an integrated mass balance of ^{234}U

with depth. Diffusion of alpha-recoiled ^{234}U from surrounding sediment, which reprecipitates at aU peaks, can explain the excess ^{234}U observed during Marine Isotope Stage 7/8 and 11/12 transitions as well as partially during MIS 5/6 and MIS 9/10. Remaining ^{234}U excesses during these deglacial transitions require a possible external source of U.

2.2 Introduction

The Southern Ocean acts as a hub for thermohaline circulation and is an important driver of global heat, nutrient, and carbon cycles. One of its more salient elements is the formation of Antarctic Bottom Water, which is a control on deep ocean circulation and glacial carbon transport. During glacial periods, there is reduced atmospheric carbon dioxide (Delmas et al., 1980). This carbon must ultimately have been stored in the deep ocean during these periods as this is the only mechanism where the reservoirs equilibrate on needed time scales (Broecker, 1982), although the mechanisms for this process are still being debated (Sigman et al., 2010). Regardless, any increase in the carbon storage capacity of the biological pump, which ultimately decrease atmospheric CO_2 concentrations, also lowers the inventory of deep sea dissolved oxygen proportional to the Redfield ratio of respiration (Broecker, 1982; Galbraith & Jaccard, 2015; Redfield, 1958; Sigman et al., 2010). This relationship allows for past ocean carbon storage to be qualitatively constrained using deep sea dissolved oxygen budgets (Anderson et al., 2019; Francois et al., 1993). One method to assess oxygen delivery to the deep sea by bottom water ventilation, when combined with proxies for organic matter flux, is the use of redox-sensitive trace metals in sediment (Francois et al, 1997).

One such redox tracer is U, which is soluble and well-mixed throughout the world's oxygenated oceans; however, uranium becomes insoluble in suboxic pore waters (Henderson & Anderson, 2003; Ku et al., 1997; Zheng et al., 2002). Its residence time in seawater far exceeds the time scale of global ocean mixing and individual glacial-interglacial cycles, leading to the assumption that U chemistry is relatively unchanged over these time scales (Esat & Yokoyama, 2006). Authigenic uranium (aU), which is formed by *in situ* precipitation in oxygen depleted pore waters, has been used as a proxy for changes in circulation/ventilation (Chase et al., 2001; Francois et al., 1993; Hayes et al., 2014; Jaccard et al., 2016) and organic carbon delivery (Jaccard et al., 2013). The other major component of U flux to the sediments is detrital U, supplied via continental sources including rivers, aeolian dust deposition, or ice rafted debris. Because of its redox sensitivity, records of U are potentially prone to post-depositional alteration, such as "burn-down", which can complicate the use of aU and detrital U as paleoproxies (Wilson et al., 1986). This study explores bulk sedimentary U isotope ratios as a diagnostic tool for the diagenesis of U after burial.

Eq. 1 $$\delta^{234}U = \left(\left(\frac{^{234}U}{^{238}U}_{meas} \Big/ \frac{^{234}U}{^{238}U}_{eq} \right) - 1 \right) * 1000$$

Where $\delta^{234}U$ is the isotopic composition of U as a per mil (‰) deviation from secular equilibrium. $(^{234}U/^{238}U)_{meas}$ is the measured activity ratio and $(^{234}U/^{238}U)_{eq}$ is the activity ratio of U isotopes at secular equilibrium.

Both aU and detrital U have unique U isotopic compositions stemming from systematic fractionation during the U cycle. Variations in $\delta^{234}U$ from secular equilibrium occur from alpha-recoil, where the alpha-decay of ^{238}U ejects its daughter isotope ^{234}Th

out of the mineral lattice entirely or into a damaged lattice site. Subsequently ^{234}Th (half-life 24.1 days, Knight & Macklin, 1948) and its daughter ^{234m}Pa (half-life 1.17 minutes, Firestone et al., 1998) beta-decay into the longer-lived ^{234}U (half-life 245,620 yrs, Cheng et al., 2013). At macroscales, this effect leads to preferential loss of ^{234}U in terrestrial rock, creating a flux of ^{234}U to marine systems from terrestrial riverine discharge and a flux from marine sediment pore-waters also enriched by alpha-recoil (Henderson, 2002; Ku, 1965). In marine sediment, alpha-recoil creates a pool of ^{234}U that is reactive and prone to remobilization (Gourgiotis et al., 2011; Maher et al., 2004), which may be preferentially mobilized during sedimentary diagenesis. These inputs of ^{234}U from alpha-recoil keep δ^{234}U seawater above secular equilibrium with a modern global average of 146.8 ± 0.1‰ (Andersen et al., 2010). There is evidence to show this global seawater value fluctuates over glacial-interglacial cycles, as coral records support changes as high as ~ ± 15‰ (Esat & Yokoyama, 2006; Henderson & Anderson, 2003). However, more recent assessments have suggested the Last Glacial Maximum seawater δ^{234}U may have been closer to 5 - 7‰ lower than modern seawater composition (Chen et al., 2016; Chutcharavan et al., 2018) and relatively constant throughout the late Quaternary (Esat & Yokoyama, 2006; Henderson, 2002; Robinson et al., 2004). In some environments, such as during the anoxic formation of shallow carbonates, the change in form from seawater U(VI) to sedimentary U(IV) can induce a δ^{234}U mass fractionation of ~0.8 – 1.6‰ heavier than expected (Romaniello et al., 2013). Authigenic U precipitation in the pelagic ocean should, at least initially, reflect the δ^{234}U seawater composition. Detrital sediments are expected to have δ^{234}U close to secular equilibrium (0‰) due to radioactive decay, however, due to loss of ^{234}U from alpha-recoil, can be slightly negative

(Thomas et al., 2007). The exact $\delta^{234}U$ of detrital materials can vary as the amount of ^{234}U lost from alpha-recoil is a function of 1. Sediment age since formation by mechanical erosion and 2. Grain size (DePaolo et al., 2006a, 2012). Given the half-life of ^{234}U (~254 ka), a steady state between ^{234}U and ^{238}U is reached after 1 Ma that depends only on grain size (DePaolo et al., 2006a, 2012). For larger grains (>65 μm), this steady state is roughly the same as secular equilibrium (0‰), but for smaller grain sizes, the fractional loss of ^{234}U can be between a few percent and ~50%, with the expectation that the $\delta^{234}U$ of fine silts sediment (~10 μm) is ~240‰ (Bourne et al., 2012; DePaolo et al., 2006b, 2012).

2.3 Methods

2.3.1 ODP 1094

ODP 1094 (53.18035˚ S, 5.130333˚ E, 2807 m water depth, Fig. 2.1) is an Atlantic-sector Southern Ocean core to situated between the Antarctic Polar Front to the north and the southern boundary of the Antarctic Circumpolar Current to the south. This location is close to the Weddell Sea, a known site for the formation of Antarctic Bottom Water, and the core site is bathed by Circumpolar Deep Water (Shipboard Scientific Party, 1999a). ODP 1094 primarily consists of Pleistocene age diatomaceous ooze (60 - 80% biogenic opal; Shipboard Scientific Party 1999a) during interglacial sections, with punctuated increases in volcaniclastic particles and crystalline quartz derived from Ice Raft Debris (IRD) present during glacial periods (Kanfoush et al., 2002; Nielsen et al., 2007), and a relative lack of calcium carbonate (<1%), except during deglacial intervals where $CaCO_3$ reaches at most 10% (Jaccard et al., 2013). Present day redox conditions of bottom water at this location are generally well oxygenated (average dissolved O_2

concentration of ~200 - 230 μM) due to influx of recently ventilated subsurface water masses (Jaccard et al., 2016). Previous efforts have reconstructed ODP 1094's paleoredox conditions using aU over the past 150 ka (Hayes et al., 2014) and 500 ka (Glasscock et al., 2020); these studies ultimately showed that aU in this area is sensitive to redox changes in sediments from both increases in organic matter delivery and sluggish bottom water ventilation. Additional paleoredox constructions using aU, Mn, and Re have shown that ODP 1094 has experienced constantly sub-oxic conditions over the last 500 ka, which makes oxic remobilization of authigenic trace metals unlikely (Rohde et al., 2021).

ODP 1094's age model was constructed using paleomagnetic and biostratigraphic markers (Shipboard Scientific Party, 1999b) which have been further refined by tuning the oxygen isotopes of benthic foraminifera to the LR04 global benthic stack (Hasenfratz et al., 2019; Lisiecki & Raymo, 2005) (Fig. 2.2). The greatest certainty in the age model is during deglacial transitions, having 3 – 4 tie points in <10 ky, however this age model is less confined during other periods. Given the average sedimentation rate, an age model uncertainty of ~5.5 ky can create an offset of 1 meter in the U record with other proxies. For this study, the section of ODP 1094 analyzed was between 0.57 to 76.29 meters composite depth (corresponding to ages of ~1 to 504 ka), and new results were combined with the bulk U data presented in Hayes et al., 2014 and Glasscock et al., 2020. The average sedimentation rate for this section was ~17 cm/ka, with sampling rate intervals of 10 cm to create sub millennial resolution.

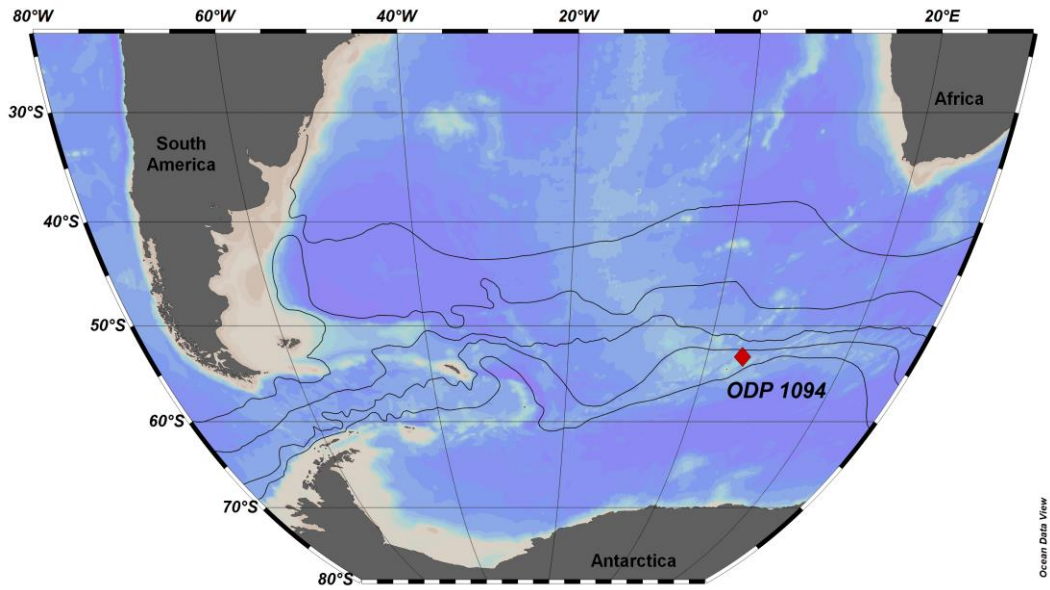

Figure 2.1 *Location of ODP 104*

ODP 1094 (53.18035˚ S, 5.130333˚ E, 2807 m) is in the center of the ice-free Antarctic Zone bounded by the Polar Front to the north and the Southern Antarctic Circumpolar Current boundary to the south (Shipboard Scientific Party, 1999b). Black lines show Southern Ocean fronts as defined in (Orsi et al., 1995); (North to South) Subtropical Front, Sub-Antarctic Front, Antarctic Polar Front, and the southern boundary of the Antarctic Circumpolar Current.

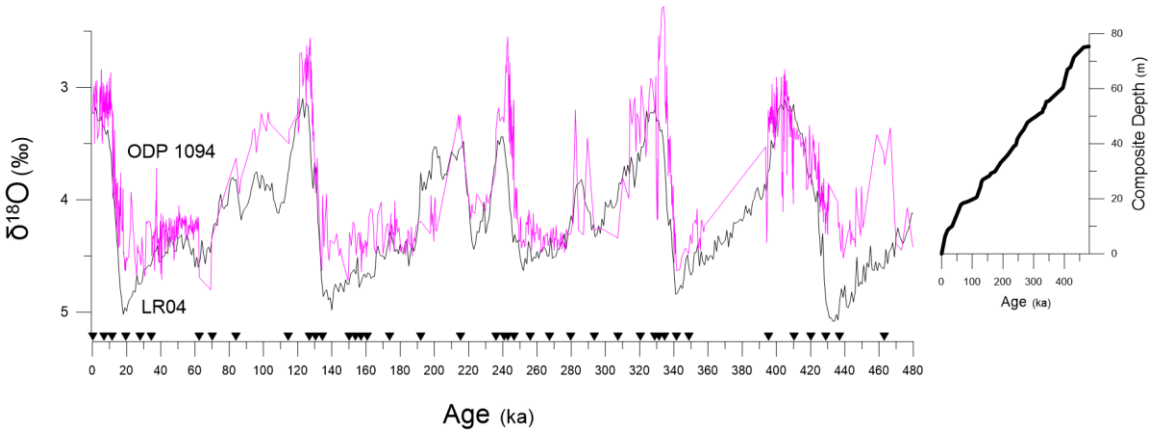

Figure 2.2 *$\delta^{18}O$ at ODP 1094 compared to the global benthic stack*

Global stack of benthic $\delta^{18}O$ (black) from (Lisiecki & Raymo, 2005) (LR04) shows changes in global glaciation. The benthic $\delta^{18}O$ for ODP 1094 (pink) from Hasenfratz et al., 2019 is tuned according to the LR04 stack (tie points shown with black triangles). Inset figure shows the age to depth model used in Hasenfratz et al., 2019.

2.3.2 Isotopic Measurements

U isotope data covering the period 0 to 504 ka were produced in three laboratories (at the Lamont-Doherty Earth Observatory Data, the Massachusetts Institution of Technology, and the University of Southern Mississippi, respectively). All three labs used similar methods for strong acid digestions and total dissolution of the sediments, and pre-concentration with iron (oxy)hydroxide co-precipitation, followed by anion exchange chromatography, to analyze uranium isotopes using isotope dilution with ^{236}U (Glasscock et al., 2020; Hayes et al., 2014, 2017). The main difference in sediment digestion techniques is that the Lamont lab used perchloric acid during digestions with HNO_3, HCl and HF, while the MIT and USM labs did not use perchloric acid but still achieved total sediment dissolution using a combination of HNO_3, H_2O_2, HCl and HF.

Data for ^{234}U activities from the 0 to 157 ka section (144 samples at roughly millennial resolution) were produced initially at the Lamont-Doherty Earth Observatory in 2010 - 2012. The Lamont data were analyzed using a single-collector, VG Axiom inductively-coupled plasma mass spectrometer (ICP-MS). Corrections for tailing of the ^{235}U peak onto measured ^{234}U count rates were made using the geometric mean of the count rates at mass-to-charge ratios 233.5 and 234.5. Corrections for instrumental mass bias were made by bracketing samples with standard solutions of SRM129 every 5 - 10 samples, and blank corrections on ^{238}U and ^{234}U were less than 0.2% of measured signals. The average precision on $\delta^{234}U$ values for samples and standards was 12‰. Duplicate digestions were analyzed (n = 7) and the $\delta^{234}U$ of duplicates agreed within an average of 27‰. The bulk U concentrations from this work were used in published studies (Hayes et al., 2013; Jaccard et al., 2013) for which only the ^{238}U activities were necessary, and the

^{234}U activities were not published at that time. As a point of historical context, in the Lamont data an anomaly of measured and decay corrected $\delta^{234}U$ was found of ~200‰, higher than ~147‰, the ratio in seawater, during MIS 5 (specifically around 127 ka), which will be described more fully in results. Because of the relatively large uncertainties in the Lamont $\delta^{234}U$ data, there was some question whether these data were of high enough quality to merit further investigation. Therefore, we sought to confirm the anomalous finding using a higher precision multi-collector ICP-MS.

In 2014, a suite of 24 samples from throughout the 38 to 155 ka sections were analyzed at MIT on a Nu Plasma II multi-collector ICP-MS, capable of an improved average precision on samples and standards of 2‰. At MIT, every sample was bracketed with a standard solution of CRM-112a and ^{234}U was analyzed on the central ion multiplier, with ^{238}U being analyzed on a Faraday cup simultaneously. A peak jumping routine also had to be used to measure count rates at mass-to-charge ratios of 233.5 and 234.5 on the ion multiplier for a ^{234}U tail correction similar to that described above. MIT blank corrections were less than 0.1% on U isotopes. These data confirmed the large positive $\delta^{234}U$ anomaly around 127 ka (Fig. 2.3) and gave confidence that any further anomalies in $\delta^{234}U$ were likely resolvable using the lower precision single collector, Element HR-ICP-MS at USM.

We now turn to provide more details on the procedures used to determine $\delta^{234}U$ at USM from 2017 - 2019 in sections of ODP-1094 covering 156 to 504 ka, (280 samples at roughly millennial resolution). Freeze-dried sediment samples of 50 mg were spiked with a known quantity (0.1 ng) of ^{236}U (Eckert & Ziegler Isotope Products) and then dissolved in a series of digestions including HNO_3, H_2O_2, HCl and HF, as described by (Glasscock

et al., 2020). Once fully dissolved, 2 - 3 mg of iron, as dissolved iron chloride, was added to the solution and pH was raised using drops of NH_4OH until an iron oxyhydroxide containing the U was precipitated. U was extracted via column chromatography on Dowex 1X8 resin. Count rates of ^{234}U, ^{235}U, and ^{236}U were measured on the Thermo Element HR-ICP-MS at USM. The ICP-MS analysis method was similar to that described for the Lamont lab above, using solutions of CRM-112a bracketing every 5 - 10 samples to correct for instrumental mass bias and making a tail correction based on count rates at mass-to-charge ratios 233.5 and 234.5. Decay-corrected $\delta^{234}U$ values were calculated based on measured $^{234}U/^{235}U$ ratios, assuming a seawater $^{238}U/^{235}U$ ratio of 137.83 (Andersen et al., 2016) and the following half-lives (^{234}U, 2.456×10^5 yr; ^{238}U, 4.468×10^9 yr; (Villa et al., 2016). Using ^{235}U here and avoiding the measurement of the most abundant isotope, ^{238}U, allowed measurement of a higher signal of ^{234}U. The sub-per mil level variation of $^{235}U/^{238}U$ in the ocean (Andersen et al., 2017) causes a negligible change in $\delta^{234}U$ calculated this way. The average precision of $\delta^{234}U$ for the USM data was 22‰. Blank corrections on U isotopes were less than 0.2% of measured signals. Duplicate (n = 37) and triplicate (n = 4) digestions were analyzed and the average standard deviation of replicate measurements was 26‰.

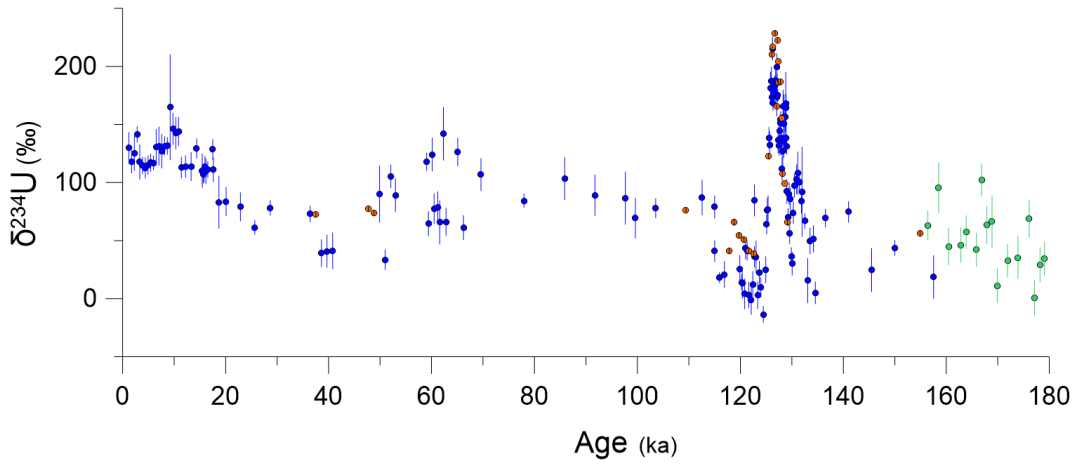

Figure 2.3 *Bulk observed $\delta^{234}U$ from 3 labs*

Bulk observed δ^{234}U (‰, per mil) in ODP 1094 as a function of sediment age illustrating the results from overlapping sections analyzed by three labs (blue – Lamont-Doherty Earth Observatory, orange – Massachusetts Institute of Technology, green – University of Southern Mississippi).

2.3.3 Model for Predicting Bulk δ^{234}U

An endmember mixing model (Fig. 2.4, gray line) was made to predict δ^{234}U at depth using the following steps; 1. Calculation of aU and detrital U from ^{232}Th/IRD (Eq. 2 and 3), 2. Mixing of aU and detrital U fractions with known δ^{234}U (Eq. 4, and Fig. 2.4, blue and purple), and 3. Decay for comparison to modern observed data (Eq. 4). The uncertainty for these predictions was propagated using the uncertainty of the lithogenic ^{238}U/^{232}Th mass ratio and uncertainty in the δ^{234}U of detrital U (Fig. 2.4, gray envelope).

The fraction of aU and detrital U were calculated as follows:

Eq. 2 $$[aU] = [U_{bulk} * (1 - F_{U,det})]$$

Where [aU] is the concentration authigenic U in ppm (µg/g). U_{bulk} is the concentration of U in bulk sediment in ppm. $F_{U,det}$ is the fraction of total U that is detrital.

Eq. 3 $$F_{U,det} = \frac{[^{232}Th] * \left(\text{lithogenic } \frac{^{238}U}{^{232}Th} \text{ mass ratio}\right)}{U_{bulk}}$$

Where $F_{U,det}$ is the fraction of total U that is detrital. [^{232}Th] is the concentration of ^{232}Th in bulk sediment in ppm. The lithogenic ^{238}U/^{232}Th mass ratio is representative of terrigenous materials. U_{bulk} is the concentration of U in bulk sediment in ppm.

Given the assumption that the observed concentration of bulk sedimentary U (ppm) is a conservative mixing of authigenic and detrital fractions, determining one of these fractions allows for the calculation of each component's relative concentration (ppm) (Eq. 2). The detrital fraction of bulk sedimentary U, $F_{U,det}$, can be estimated from measurements of ^{232}Th (ppm) (Eq. 3), an isotope assumed to be of entirely lithogenic origin, by using lithogenic ^{238}U/^{232}Th activity ratio representative for its ocean basin (Brewer et al., 1980; Henderson & Anderson, 2003). To account for potential variability of this site, a range of 0.4 to 0.7 was used (Henderson & Anderson, 2003). For these calculations, the activity ratio was converted to mass which yielded a lithogenic ^{238}U/^{232}Th mass ratio of 0.178 ± 0.049. While ^{232}Th concentration can be used to calculate detrital material from its concentration of detrial material, this relationship is dependant on the ratio of volcanics to Upper Continental Crust. Comparitively, the ratio of lithogenic ^{238}U/^{232}Th varies significantly less regionally and can be used to calculate aU without knowledge of the volcanic to Upper Continental Crust composition of the sediment. Measurements of ^{232}Th were taken for two intervals: 0 - 155 ka and 370 - 450 ka. In these intervals, a strong correlation existed between ^{232}Th concentrations and IRD (^{232}Th (dpm/g) = .0034 * IRD (grains/g) + 0.065, R = .79, n = 203, p < .00001, updated from (Glasscock et al., 2020)). For samples in which ^{232}Th was not measured, ^{232}Th

concentrations were estimated from this relationship using IRD records from (Kanfoush et al., 2002).

Eq. 4 $$\delta^{234}U_{bulk,t} = ((1 - F_{\mathrm{U,det}})\delta^{234}U_{sw} + F_{U,det}\delta^{234}U_{det}) * e^{-\lambda_{234}t}$$

Where $\delta^{234}U_{bulk,t}$ is the predicted U composition of bulk sediment U at core age t. $\delta^{234}U_{sw}$ is the U isotopic composition of seawater. $\delta^{234}U_{det}$ is the U isotopic composition of detrital sediments.

The expected isotopic composition of bulk U at sediment age (t) is given by a combination of each source's relative fraction and composition (both unitless), accounting for the decay of ^{234}U ($e^{-\lambda 234}$) for direct comparison with present day values (Fig. 2.4). The $\delta^{234}U$ of modern seawater used was 147‰ (Andersen et al., 2010). Although, the $\delta^{234}U$ of seawater is potentially variable over glacial cycles as a response to changes in physical weathering, a box model by (Henderson, 2002) has shown that $\delta^{234}U$ probably couldn't have changed more than 10‰ over 800,000 years. To account for the potential variability in $\delta^{234}U$ composition of detrital U, a range of -150 ± 100‰ was used from the model of (DePaolo et al., 2006).

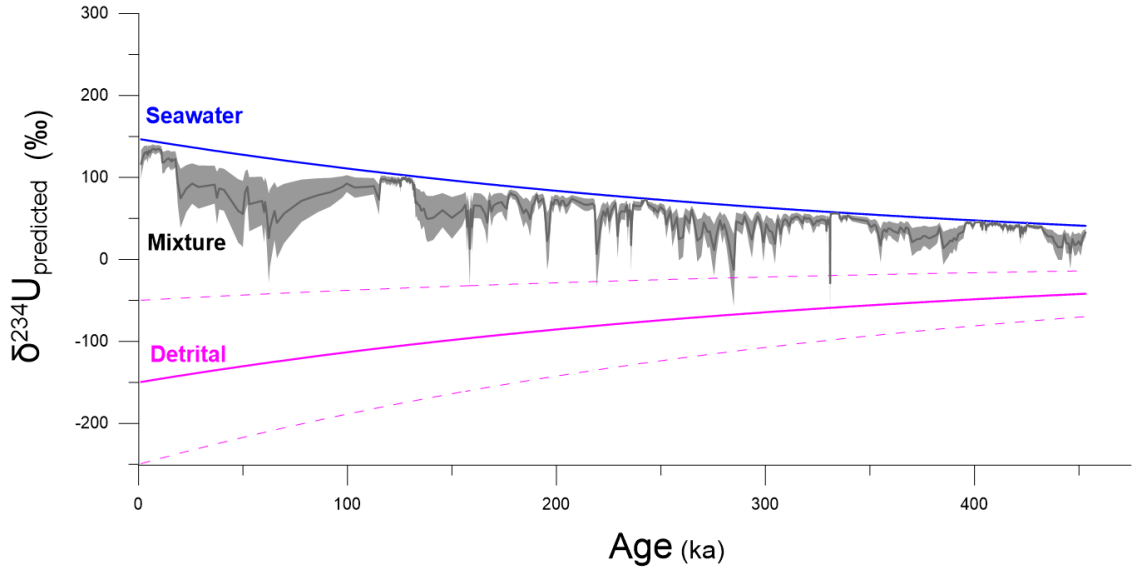

Figure 2.4 *Model of predicted bulk $\delta^{234}U$ as a function of sediment age*

Model of predicted bulk $\delta^{234}U$ (gray) as a function of sediment age given authigenic U (blue) and detrital U (purple) endmembers. The colored lines show age-decayed, pure endmember composition for aU (blue, decayed from ~ 147‰), and detrital U (purple, decayed from -150, dotted lines show uncertainty decayed from ± 100‰). The predicted $\delta^{234}U$ (gray line) is created using Eq. 2, 3 and 4, and uses the detrital U fraction calculated using a lithogenic mass ratio of 0.178, $\delta^{234}U$ of aU decayed from 147‰, and $\delta^{234}U$ of detrital U decayed from -150‰. The uncertainty of predicted $\delta^{234}U$ (gray envelope) is propagated from the uncertainty in determining the detrital fraction (Eq. 3, lithogenic $^{238}U/^{232}Th$ mass ratio ± 0.0485) and the uncertainty of detrital $\delta^{234}U$ (Eq. 4, ± 100‰).

2.4 Results

2.4.1 Observed aU and $\delta^{234}U$ Records

Authigenic U was the dominant form of U in ODP 1094, on average consisting of 90.5% of the bulk sediment fraction. ODP 1094 displays generally lower aU concentration during interglacial intervals and higher concentrations during glacial periods (Fig. 2.5). Among deglacial transitions, the aU behavior is not identical, although some features appear in multiple cycles. For the glacial terminations at MIS 5/6, 7/8, and 9/10, aU concentration drops precipitously at the start of deglaciation, and these drops are followed by peaks of aU concentration, likely as a result of increased organic matter

delivery/ high mass accumulation rate, which in turn increases respiration in sediment and precipitates aU. These peaks of aU concentration fall sharply concurrent with the end of deglaciation as organic fluxes begin to fall. MIS 5/6 differs from this group in that it has an additional aU peak around 127 ka associated with a change in Antarctic Bottom Water formation (Hayes et al., 2014; Zhou & McManus, 2022). MIS 11/12 is similar, although these features are spread out more, which reflects the longer time scale of this termination. MIS 11/12 shares an initial drop in relative aU concentration at the start of the glacial termination, followed by a series of small concentration peaks which extend into the glacial period. The MIS 11 aU concentration peak at 395 - 401 ka is similar to that of 127 ka which is believed to be reflective of sluggish bottom water conditions (Glasscock et al., 2020). The most recent glacial termination (< 20 ka) appears to show a small peak aU concentration.

There are some apparent similarities of the $\delta^{234}U$ record to aU concentrations, although they are not directly comparable. The most striking feature in this comparison is similar peaks in $\delta^{234}U$ and aU in the sections surrounding glacial terminations (Fig. 2.5). There was no significant correlation between $\delta^{234}U$ to aU throughout the whole record; however, when comparing only the features surrounding glacial terminations (further defined in the next section), a moderate ($R = 0.42 - 0.83$), and significant ($p < 0.05$) linear correlation was observed (Fig. 2.6). Generally, both aU and $\delta^{234}U$ seem to be enriched around periods of higher organic rain rate (Fig. 2.7, green), explaining correlation, however, this correlation is imperfect as the mechanism imparting each may be slightly different and the uncertainty in the age model is generally higher around deglacial terminations.

While we might expect this relationship during these high mass accumulation events, the correlation between aU and $\delta^{234}U$ (of lower values) is continued meters into both sides of adjacent sediment. During MIS 5/6, 7/8, and 9/10, $\delta^{234}U$ is high during deglaciation and is relatively low in the periods before and after this peak. MIS 11/12 is similar but has two unique peaks of high $\delta^{234}U$. However, these patterns are not synchronous with the changes in the aU record and are not confined within changes in the benthic $\delta^{18}O$, even given the uncertainty of the age model. Accomapanying changes in high or low $\delta^{234}U$ are significantly broader than its aU counterpart, making it appear that the signal is "smeared" over a longer timeframe. Although this "smearing" indicates that any relationship between $\delta^{234}U$ and aU is likely non-linear, correlation between them in only these select intervals suggests a mechanistic link between the two.

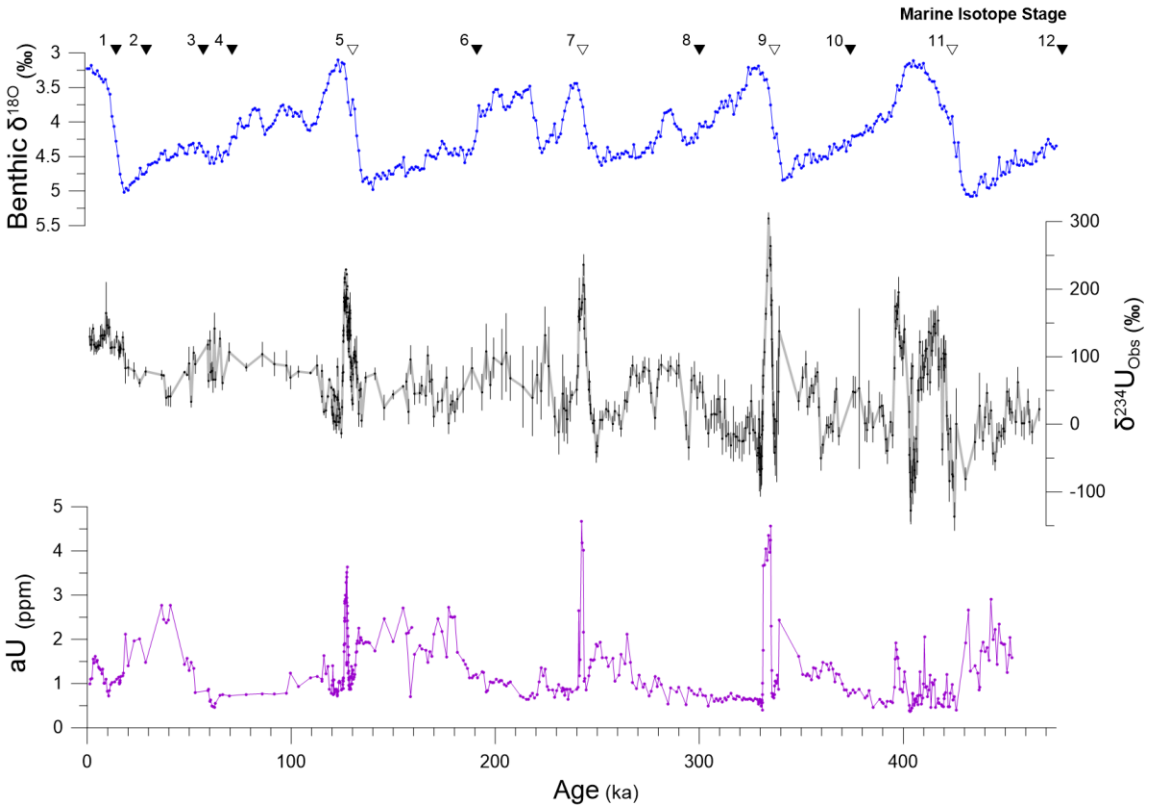

Figure 2.5 *$\delta^{234}U$ in ODP 1094 over the last 480 ka*

$\delta^{234}U$ in ODP 1094 over the last 480 ka. Marine Isotope Stages (triangles) are defined by the benthic $\delta^{18}O$ record (blue, from (Lisiecki & Raymo, 2005)) and shows changes in global glaciation. Observed bulk $\delta^{234}U$ (black) shows generally increased values during spikes in aU (purple) surrounding glacial terminations (marked as white triangles for MIS 5/6, 7/8, 9/10, and 11/12 transitions). The aU plotted is calculated from a lithogenic $^{238}U/^{232}Th$ mass ratio of 0.162.

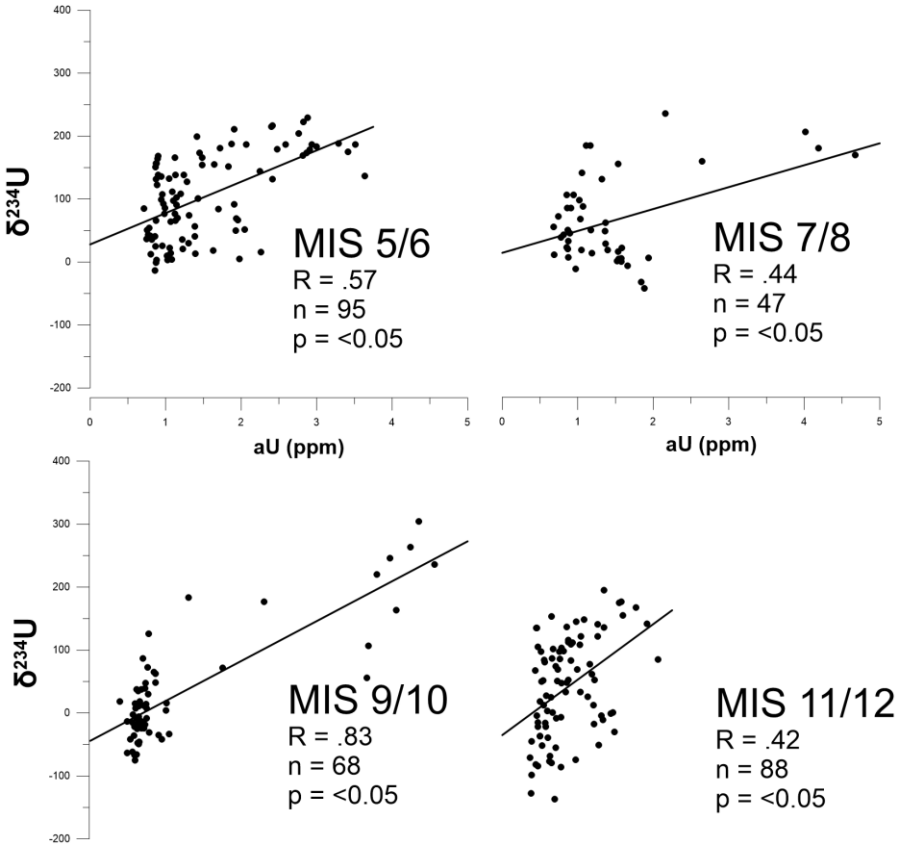

Figure 2.6 *Relationship between $\delta^{234}U$ and aU*

Relationship between $\delta^{234}U$ and aU (calculated from a lithogenic $^{238}U/^{232}Th$ mass ratio of .1615) for anomalous sections around the MIS 5/6, 7/8, 9/10, and 11/12 transitions. Sections are defined by periods where $\delta^{234}U$ was greater than the $\delta^{234}U$ of seawater and its adjacent low $\delta^{234}U$ anomalies. These sections are plotted in Fig. 2.8. While there is no relationship between $\delta^{234}U$ and aU in ODP 1094 as a whole, these variables are positively correlated during certain periods such as during high organic mass fluxes during deglacial transitions. However, this relationship extends into adjacent sediment, which is potentially emblematic of preferential ^{234}U remobilization.

2.4.2 Relationship of $\delta^{234}U$ to Pre-Alteration Model

By finding differences between the predicted bulk $\delta^{234}U$ of the endmember mixing model and the observed $\delta^{234}U$ isotope data, we were able to identify sections of ODP 1094 where it is potentially subject to post-depositional mobilization of ^{234}U. We define observed values of $\delta^{234}U$ within model expectations, and thereby unaltered, where

the uncertainty of observed bulk $\delta^{234}U$ intersects with the uncertainty of predicted bulk $\delta^{234}U$ (Fig. 2.4). In total, 283 of 595 data points (47%) fell outside of model expectations (Fig. 2.7), which represent a significant fraction of geologic time in the core. Small anomalies were found within glacial-interglacial periods, however the largest deviation from model expectations occurred within adjacent sections surrounding deglacial transitions MIS 5/6, 7/8, 9/10, and 11/12 (Fig. 2.8). These anomalies were characterized by high $\delta^{234}U$ peaks, that were significantly greater than the decayed seawater endmember, which are bordered by sections with low anomalies (red and blue bars on Fig. 2.8).

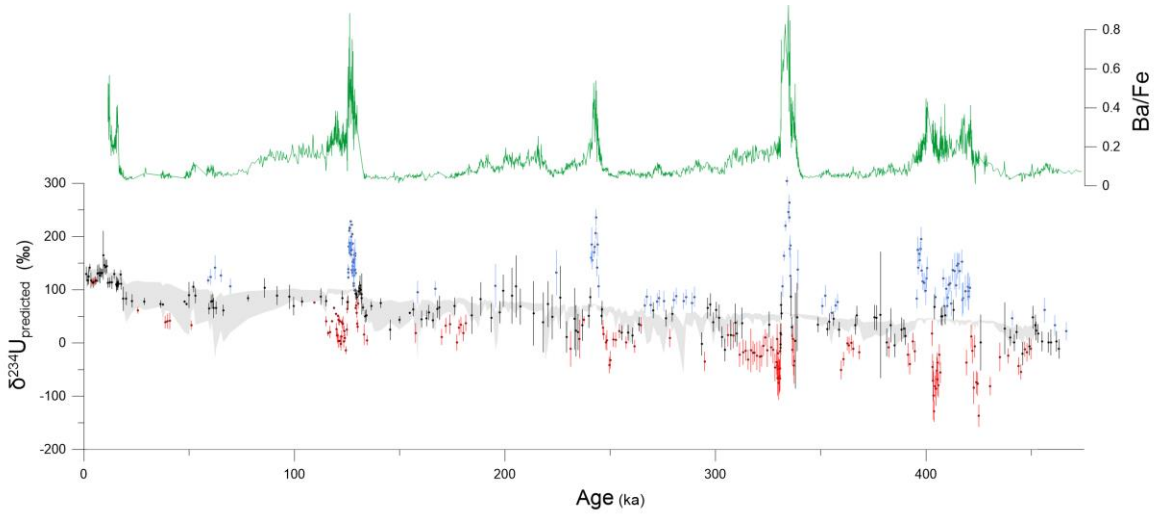

Figure 2.7 *Model of predicted $\delta^{234}U$ vs Ba/Fe*

Ba/Fe (green) shows the record of productivity at ODP 1094 (Jaccard et al., 2013), which illustrate periods of increased organic carbon flux. Modern bulk $\delta^{234}U$ is predicted (gray) by an age decayed mixing model of aU and detrital U using Eq. 2, 3 and 4. The range of uncertainty (gray envelope) is propagated from a lithogenic $^{238}U/^{232}Th$ mass ratio of 0.178 ± 0.049 and $\delta^{234}U$ of detrital U of -150 ± 100‰. Observed bulk $\delta^{234}U$ is colored by its relationship to predicted bulk $\delta^{234}U$. If the range of uncertainty of predicted $\delta^{234}U$ and the range of uncertainty of observed $\delta^{234}U$ intersect, data is considered within model expectations (black). Data were considered above (blue) or below (red) model expectations if the range of uncertainty of observed bulk $\delta^{234}U$ is greater than or less than predicted bulk $\delta^{234}U$ respectively.

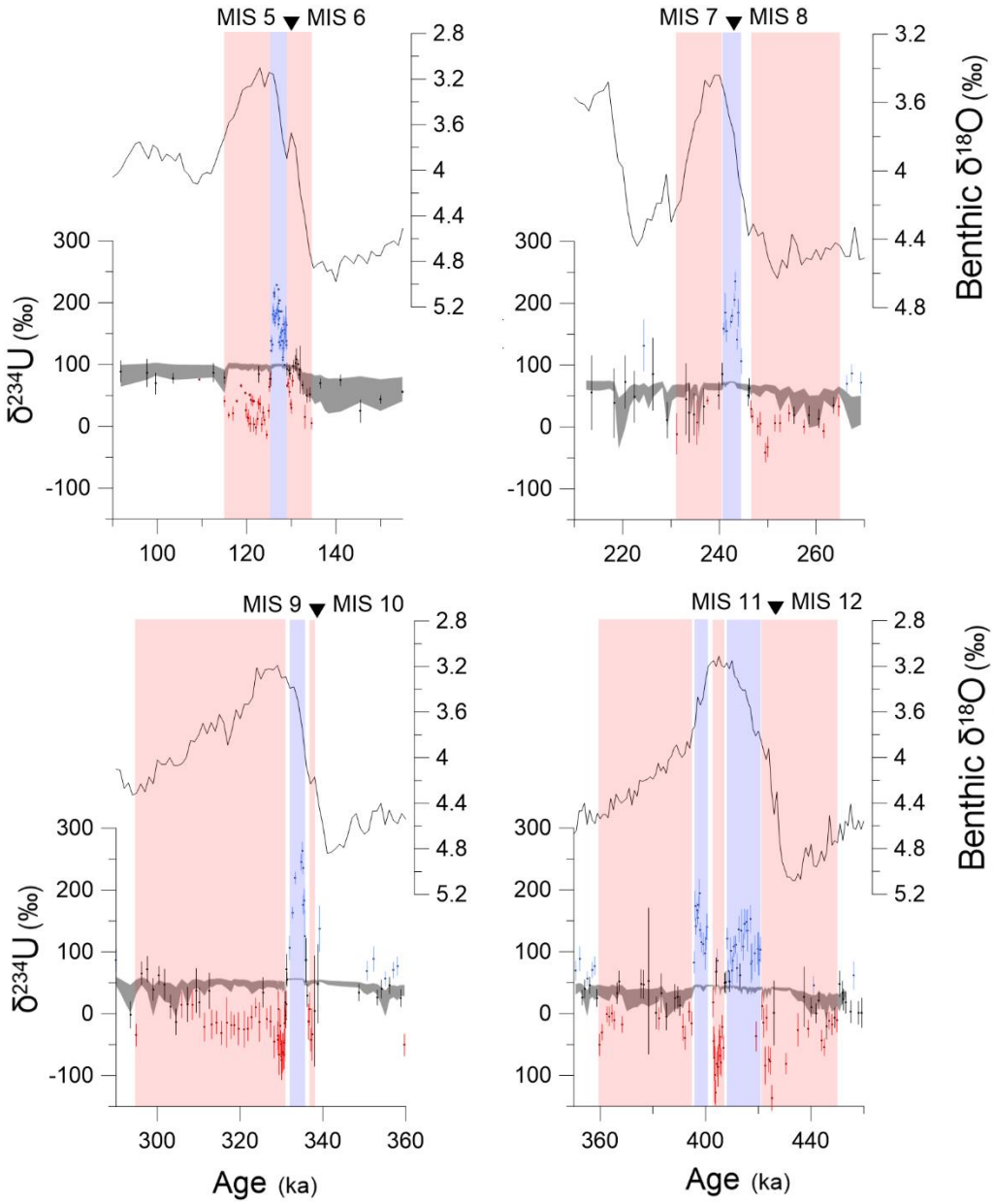

Figure 2.8 *Four $\delta^{234}U$ anomaly sections*

Characterization of four $\delta^{234}U$ anomaly sections, MIS 5/6, 7/8, 9/10, and 11/12, used for mass balance. Benthic $\delta^{18}O$ record from (Lisiecki & Raymo, 2005) is displayed on each subplot (black) to show changes in global glaciation. The bottom half of each subplot is enlarged from Fig. 2.4. Each subplot shows the uncertainty of predicted bulk $\delta^{234}U$ (gray envelope, derived from the propagated uncertainty in Eq. 3 and 4), overlain by observed bulk $\delta^{234}U$. Sections of colored points and bars represent sections where adjacent anomalies of observed bulk $\delta^{234}U$ are greater (blue) or less (red) than the uncertainty of predicted bulk $\delta^{234}U$. These four sections were identified by finding values where observed bulk $\delta^{234}U$ was significantly higher than the decayed $\delta^{234}U$ of seawater and its surrounding intervals of low $\delta^{234}U$.

2.5 Discussion

2.5.1 Relationship between aU and $\delta^{234}U$

The anomalous patterns observed may be explained by the differences in the reprecipitation potential of alpha-recoiled U in sediments. Authigenic U is present at all depths of this record, which implies that there is functionally no U concentration in surrounding pore waters. However, ^{234}U is introduced into the pore water when alpha-recoil occurs, acting as a relatively constant source of ^{234}U to all sediment layers over time. Some of this ^{234}U may reprecipitate back in place, but this effect will be stronger in intervals with greater reducing capacity, such as those with high organic delivery during deglaciation. A mechanism proposed for the reduction of aU is the active respiration of sulfate/Fe reducing bacteria, which may explain why intervals with the highest organic carbon flux, and thereby the highest sustained respiration, might act as persistent sinks of U (Lovley et al., 1993). Stronger rates of reprecipitation at these intervals drives lower ^{234}U concentration in surrounding pore water compared to adjacent sediment layers. In turn, this gradient in ^{234}U concentration in pore water drives diffusion of ^{234}U towards these highly reducing layers.

Eq. 5 $$F_{^{234}U} = D * \frac{\Delta[^{234}U]_{PW}}{\Delta x}$$

This mechanism can generally be described with Fick's first law of diffusion (Eq. 5), where F_{234U} is the flux of ^{234}U between two pore water intervals, D is the diffusivity coefficient for U in sediment pore water, $\Delta[^{234}U]_{PW}$ is the difference in ^{234}U concentration between pore water intervals, and Δx is the distance between pore water intervals. Two of the three variables that determine the flux of ^{234}U in pore water are known. The diffusivity of U in sediment pore water (D) is $3x10^{-6}$ cm^2s^{-1} (Klinkhammer & Palmer,

1991). The distance of ^{234}U diffusion (Δx) can be assumed to be the distance between core sections of high $\delta^{234}U$ anomaly and low $\delta^{234}U$ anomaly (colored sections of Fig. 2.8), which is generally on the scale of a few meters. Given this diffusivity coefficient and the age of sediment older that MIS 5, there is enough time for ^{234}U to diffuse over the distances observed across anomaly sections. The variable that is least constrained in the gradient of pore water ^{234}U concentrations. The ratio of the accumulation rate of aU and other redox sensitive trace metals at ODP 1094, such as aRe and Mn, show there has been little remobilization of bulk U from oxygen changes in this record (Rohde et al., 2021). This means that aU concentrations are potentially useful for gauging the relative strength of redox reprecipitation in surrounding pore water, however, the concentration of sedimentary aU is not indicative of the ^{234}U concentration in pore water. This hypothesis may also explain why the correlation between aU and observed bulk $\delta^{234}U$ is not perfect as the redistribution of ^{234}U will be some combination of its mobility via diffusion over time and its reprecipitation dependent on the history of organic carbon flux.

It should be noted that although this mechanism explains the apparent relationship between sediment aU and $\delta^{234}U$ at ODP 1094 and other open ocean records (such as site 90-13-13 in the Labrador Sea, (Vallières, 1997), or the Lomonosov Ridge, (Purcell et al., 2022)), some types of geologic settings or diagenetic effect can reverse the apparent relationship. Changes in aU at ODP 1094 are relatively within a few ppm of its background, so aU precipitation represents only small changes within suboxic conditions (Rohde et al., 2021). After undergoing burn-down, Mediterranean sapropels described by (Gourgiotis et al., 2011; Mangini & Dominik, 1979; Severmann & Thomson, 1998) show ^{234}U diffused away from peaks of aU built by the re-oxidation front. For sediment that

has undergone strong redox changes, the processes controlling the gradient of ^{234}U in pore water, unlike ODP 1094, may not solely be the result of differences in reprecipitation of alpha-recoiled ^{234}U.

2.5.2 Mass Balance

A mass balance was created by backtracking isotope data into a ^{234}U budget with the purpose of determining whether observed alterations of U isotope can be explained by simple rearrangement of ^{234}U. The mass of ^{234}U per volume at each data point was integrated using simple trapezoids to estimate the total ^{234}U mass in each section (Eq. 6). The same process was applied to the model of predicted $\delta^{234}U$ (Eq. 7) and then the difference between these two represent the total quantified ^{234}U mass anomaly (Eq. 8):

Eq. 6 $$^{234}U_{obs} = \int_{z1}^{z2} \frac{\rho_{sed} * [^{238}U] * (1 + (1000 * \delta^{234}U_{obs})) * SA^{238}U}{SA^{234}U}$$

Eq. 7 $$^{234}U_{pred} = \int_{z1}^{z2} \frac{\rho_{sed} * [^{238}U] * (1 + (1000 * \delta^{234}U_{mod})) * SA^{238}U}{SA^{234}U}$$

Eq. 8 **Excess**

$$if\ ^{234}U_{obs} > {}^{234}U_{pred}, then\ ^{234}U_{anomaly} = {}^{234}U_{obs} - {}^{234}U_{pred}$$

Deficiency

$$if\ ^{234}U_{pred} > {}^{234}U_{obs}, then\ ^{234}U_{anomaly} = {}^{234}U_{pred} - {}^{234}U_{obs}$$

Total mass of predicted and observed ^{234}U (g/cm^2) is a function of dry bulk density of sediment (ρ_{sed}, g/cm^3), observed concentration of ^{238}U in sediment ([^{238}U], g/cm^2), and the specific activities of ^{238}U ($SA^{238}U$, 1.24 x 10^4 Bq/g, Jaffey et al., 1971) and ^{234}U ($SA^{234}U$, 2.30 x 10^8 Bq/g, Cheng et al., 2013), integrated over depths z1 and z2 (cm) with respect to core sections. For data points where the observed and predicted $\delta^{234}U$ agreed within uncertainties, the mass difference was integrated as zero. High and

low integrated anomalies were then separated into “Excess” and “Deficiency” categories based on their relationship to the model as a means to represent the potential pathway ^{234}U alteration takes during diffusion (^{234}U is potentially moving from deficiency to excess). This mass balance was done for four specific intervals (Fig. 2.8), potentially representing diagenetic alteration at MIS 5/6, 7/8, 9/10, and 11/12, where observed bulk $\delta^{234}U$ was found to be greater than its seawater endmember. Additionally, this mass balance was conducted for our entire record of ODP 1094 as a means to look at larger scale sources and alterations. This choice of data is restrained by our ability to differentiate measurements from model estimates, and thus, there is potential that better constraints for the uncertainties in Eq. 2, 3, and 4 could re-categorize points, which slightly changes terms used in for mass balance in Eq. 6, 7, and 8. For example, laboratory techniques to physically separate detrital and authigenic fractions (Martin et al., 2015) might help constrain our model’s range associated with the detrital fraction and its isotopic value. This may in turn re-contextualize an observed $\delta^{234}U$ when compared with the model, slightly altering certain parameters within our equations.

The results of our mass balance (Table 2.1) seem to indicate that anomalies at the four MIS transitions of interest support our hypothesis in part that diffusion causes a simple rearrangement of preferentially mobilized ^{234}U near aU peaks. We might expect that in a closed system, where the only change to $\delta^{234}U$ was due to internal reorganization, that the difference between excess ^{234}U and deficiency ^{234}U would be roughly zero as U is neither added nor removed from the system. This seems to be roughly the case for MIS 7/8 and MIS 11/12 as their total excess ^{234}U are marginally small within propagated error. However, this is not the case at MIS 5/6 and MIS 9/10

where a significant amount of additional ^{234}U is present, and in this case points to there being an additional external source of ^{234}U. All four anomalous sections have deficiencies of relatively similar scale (~1 - 4 pg/cm^2), which is evidence that all sections undergo a similar change from diffusive diagenesis, but the fact that they vary on the scale of excess (~5 - 50 pg/cm^2) evidences that MIS 5/6 and 9/10 require an additional source ^{234}U not accounted for in our original modeling.

Anomaly Section	Depth (m)	Def ^{234}U (pg/cm^2)	Ex ^{234}U (pg/cm^2)	Net ^{234}U (pg/cm^2)
MIS 5/6	21 - 27	3.8 ± 0.5	25.4 ± 1.6	21.6 ± 1.7
MIS 7/8	34 - 44	1.5 ± 0.4	4.7 ± 0.9	3.2 ± 1.0
MIS 9/10	49 - 54.5	3.8 ± 0.7	16.5 ± 1.5	12.7 ± 1.7
MIS 11/12	56 - 73	3.3 ± 0.7	4.8 ± 0.9	1.5 ± 1.1
Full Record to 504 ka	.57 – 75.14	13.9 ± 1.5	52.9 ± 2.6	39.1 ± 2.9

Table 2.1 *Mass balance of four anomalous sections*

Table 1. A mass balance was performed by integrating observed bulk $\delta^{234}U$ and predicted bulk $\delta^{234}U$ with depth (Fig 2.4., Fig. 2.8) into a ^{234}U inventory. The difference between these two budgets represent the potential pathway of ^{234}U mobilization and quantifies how much is mobilized. The goal of this mass balance is to assess whether there has been a simple rearrangement of ^{234}U due to diffusion from surrounding sediment (deficiency to excess). In these cases, we might expect the excess ^{234}U from high anomalies to be equal to the deficiency of ^{234}U from low anomalies. Uncertainty of mass integration is reported as the propagation of error from the uncertainty of $\delta^{234}U$ measurement at 2σ. Anomaly Section – Time period of interest. Depth – depth range of interest. Def ^{234}U – Combined integrated mass of ^{234}U below model prediction from both adjacent low anomaly features for each event. This represents how much ^{234}U could have mobilized to the high anomaly feature. Ex ^{234}U – Integrated mass of ^{234}U above model prediction at high anomaly features. Net ^{234}U – Net excess ^{234}U = Ex ^{234}U - Def ^{234}U. Values close to zero represent close system behavior of diffusion, whereas deviation represents additional source and removal terms.

2.5.3 Sources of Additional ^{234}U during MIS 5/6 and MIS 9/10

We find that a significant portion of $\delta^{234}U$ at ODP 1094 can be explained given its initial formation from authigenic and detrital sources, particularly during glacial and interglacial sections. From the anomalies that occur during deglacial transition, the entire

anomaly from MIS 7/8 and 11/12, and part of the anomaly from MIS 5/6 and 9/10, can be explained by diffusion of alpha-recoiled ^{234}U. However, the mass balance of MIS 5/6 and 9/10 shows that $\delta^{234}U$ anomalies cannot be fully explained by a simple rearrangement of existing ^{234}U. While a total explanation for this phenomenon is elusive, we look to evaluate some candidate sources to narrow potential processes such as deglacial meltwater pulses, introduction of oxidized coastal environments during sea level rise, and deposition of altered hydrothermal deposits. Because kinetic fractionation between ^{234}U and ^{238}U is on the magnitude of 1‰, the main difficulty of categorizing a single source to match our observed data is the deglacial timing and the extent of how positive our observed $\delta^{234}U$ is.

One candidate explanation for this unaccounted source of ^{234}U includes the flux of ^{234}U enriched Antarctic meltwater. This mechanism involves subglacial weathered ^{234}U becoming entrained in glacial meltwater and over time significantly enriching the water with highly positive $\delta^{234}U$, being released as its reservoirs melt. Although parts of the Greenland Ice Sheet (Arendt et al., 2018) and the Wilkes Basin (Blackburn et al., 2020), exhibit ^{234}U enriched beyond our observed data, it is unlikely that these strong, freshwater sources would permeate in Antarctic Bottom Water to the degree needed to match observations. However, these pulses can become integrated into the global $\delta^{234}U$ over glacial-interglacial time scales (Esat & Yokoyama, 2006; Robinson et al., 2004), potentially leading to a variable isotopic composition in seawater between 120 - 180‰ (Arendt et al., 2018). This explains variations seen in the paleo coral record, which invoke changes on the order of 10's ‰ (Chen et al., 2016; Esat & Yokoyama, 2006);

however, without more proximal influence from the meltwater pulse, this global effect is not enough to explain ODP 1094's $\delta^{234}U$.

A mechanism that may similarly affect globally integrated $\delta^{234}U$ of seawater is from the re-dissolution of coastal sediments during sea level rise. During interglacials and interstadials, there is an increased number of environments, such as margins, slopes, marshes, and mangroves, which are overlain by oxygen depleted water, which build U and excess ^{234}U concentrations (Chen et al., 2016; Dunk et al., 2002; Esat & Yokoyama, 2006). These sediments are oxidized during low stands and return to the ocean as sea level rises. If this process were to have a major effect on deep ocean sediment, we might also expect it to have a large effect on the more proximal coral records, in which we would expect increases matching the same magnitude of ODP 1094. This does not seem to be the case, however, as studies like that of (Chen et al., 2016), show much smaller variation (<10‰) in $\delta^{234}U$ which is asynchronous with sea level rise.

Another candidate explanation involves ferromanganese deposits enriched via the leaching of low temperature hydrothermal fluid or volcanics (Herbert Veeh & Boström, 1971; MacDougall et al., 1979). Global hydrothermal activity is hypothesized to increase during glacial terminations (Lund et al., 2016). Changes in ice sheet dynamics drive sea-level weighted pressure change on the upper mantle, which ultimately modulate melt production and by extension, hydrothermal activity (Huybers & Langmuir, 2009; Lund et al., 2016; Lund & Asimow, 2011). Ferromanganese deposits have variable $\delta^{234}U$ which is often within 20% of seawater, but has been observed to be as high as twice that of seawater (Reyss et al., 1987). While this means that hydrothermal particles are potentially enriched to the same degree as our high observations, this would require a larger percent

of the U in ODP 1094 to be hydrothermal than is possible. For example the observed values of (Reyss et al., 1987) would require nearly 100% of the sediment U to be a hydrothermal ferromanganese fraction. This cannot be the case as clean mineral analysis of TN057-13PC4, a piston core from the same location, show quartz chemistry that is not characteristic of hydrothermal origin (Nielsen & Hodell, 2007). While it is possible that volcaniclastics play a small role in $\delta^{234}U$ changes in deep sea sediment, a lack of observed hydrothermal proxies make this scenario unlikely to account for ODP 1094's observed $\delta^{234}U$ anomalies.

Lastly, variation in the sediment accumulation rate, and thereby aU accumulation, is seen across cores in the Atlantic sector of the Southern Ocean (Frank et al., 2000). We might expect that at the basin or regional scale, there is a degree of spatial heterogeneity in pore water redox state at sediment layer depths. Given the diffusivity coefficient of U in pore water, U can travel a little over 300 km per hundred thousand years, potentially allowing lateral gradients to drive ^{234}U transport at significant distance. It is possible that some excess ^{234}U is sourced by diffusion from the surrounding region from offsets in U precipitation at depth. However, determining the effect of geographic differences in pore water redox will require future work measuring U in sediment and pore waters in more core in this ocean region.

2.6 Conclusions

The U isotopic composition of ODP 1094 shows a relationship with sedimentary aU during deglacial periods of high organic rain and in surrounding sediment, but not throughout the entire record. Observed bulk $\delta^{234}U$ was compared to a model predicting $\delta^{234}U$ where distinct pattern sections of alternating high and low anomalies potentially

evidenced post-depositional diagenesis during these features. Our results show a significant amount of $\delta^{234}U$ at ODP 1094 is explained by its initial formation given authigenic and detrital components. Major sections of anomaly, identified by periods where high $\delta^{234}U$ was greater than seawater $\delta^{234}U$ and its surrounding sediment of low anomaly, were observed at MIS 5/6, 7/8, 9/10, and 11/12. It was observed that deglacial intervals with increased organic rain and increased reducing capacity act as a sink for ^{234}U that is alpha-recoiled and diffused from surrounding sediment. This remobilization of ^{234}U towards peaks of aU explains anomalies at MIS 7/8 and 11/12 entirely, and partially at MIS 5/6 and 9/10. This is evidence to support the use of $\delta^{234}U$ to identify diagenetic features in other similar pelagic sediments, however we find that deviations in $\delta^{234}U$ from expectations do not only reflect diagenetic changes. An additional source of high $\delta^{234}U$, present during some deglacial transitions, may be needed to explain the remaining excess ^{234}U during MIS 5/6 and MIS 9/10. We have considered candidate explanations for this source, including glacial meltwater and hydrothermal fluxes: however, we are unconvinced of the viability of these options in regards to ODP 1094. Although we cannot yet attribute ODP 1094's excess ^{234}U to any known physical process, the implications of this phenomenon may be important in understanding deep sea redox state and its controls on the sedimentary U budget.

2.7 Data Availability Statement

Data is available at Zenodo.org. https://doi.org/10.5281/zenodo.6959606

2.8 Works Cited

Andersen, M. B., Stirling, C. H., & Weyer, S. (2017). Uranium isotope fractionation.

Non-Traditional Stable Isotopes, *82*, 799–850. https://doi.org/10.2138/rmg.2017.82.19

Andersen, M. B., Stirling, C. H., Zimmermann, B., & Halliday, A. N. (2010). Precise determination of the open ocean 234U/238U composition. *Geochemistry, Geophysics, Geosystems*, *11*(12). https://doi.org/10.1029/2010GC003318

Andersen, M. B., Vance, D., Morford, J. L., & Bura-Nakić, E. (2016). Closing in on the marine 238U/235U budget. *Checmical Geology*, *420*, 11–22.

Anderson, R. F., Sachs, J. P., Fleisher, M. Q., Allen, K. A., Yu, J., Koutavas, A., & Jaccard, S. L. (2019). Deep-Sea Oxygen Depletion and Ocean Carbon Sequestration During the Last Ice Age. *Global Biogeochemical Cycles*, *33*(3), 301–317. https://doi.org/10.1029/2018GB006049

Arendt, C. A., Aciego, S. M., Sims, K. W. W., Das, S. B., Sheik, C., & Stevenson, E. I. (2018). Influence of glacial meltwater on global seawater δ234U. *Geochimica et Cosmochimica Acta*, *225*, 102–115. https://doi.org/10.1016/j.gca.2018.01.007

Blackburn, T., Edwards, G. H., Tulaczyk, S., Scudder, M., Piccione, G., Hallet, B., Mclean, N., Zachos, J. C., Cheney, B., & Babbe, J. T. (2020). Ice retreat in Wilkes Basin of East Antarctica during a warm interglacial. *Nature*, *583*(November 2019). https://doi.org/10.1038/s41586-020-2484-5

Bourne, M. D., Thomas, A. L., Niocaill, C. Mac, & Henderson, G. M. (2012). Improved determination of marine sedimentation rates using 230Thxs. *Geochemistry, Geophysics, Geosystems*, *13*(1), 1–9. https://doi.org/10.1029/2012GC004295

Brewer, P. G., Nozaki, Y., Spencer, D. W., & Fleer, A. P. (1980). Sediment trap

experiments in the deep north Atlantic: isotopic and elemental fluxes. *Journal of Marine Research*, *38*(4), 703–728.

Broecker, W. S. (1982). Ocean chemistry during glacial time. *Geochimica et Cosmochimica Acta*, *46*(10), 1689–1705.

Chase, Z., Anderson, R. F., & Fleisher, M. Q. (2001). Evidence from authigenic uranium for increased productivity of the glacial Subantarctic Ocean. *Paleoceanography*, *16*(5), 468–478. https://doi.org/10.1029/2000PA000542

Chen, T., Robinson, L. F., Beasley, M. P., Claxton, L. M., Andersen, M. B., Gregoire, L. J., Wadham, J., Fornari, D. J., & Harpp, K. S. (2016). Ocean mixing and ice-sheet control of seawater 234U/238U during the last deglaciation. *Science*, *354*(6312), 626–629. https://doi.org/10.1126/science.aag1015

Cheng, H., Lawrence Edwards, R., Shen, C. C., Polyak, V. J., Asmerom, Y., Woodhead, J., Hellstrom, J., Wang, Y., Kong, X., Spötl, C., Wang, X., & Calvin Alexander, E. (2013). Improvements in 230Th dating, 230Th and 234U half-life values, and U-Th isotopic measurements by multi-collector inductively coupled plasma mass spectrometry. *Earth and Planetary Science Letters*, *371–372*, 82–91. https://doi.org/10.1016/j.epsl.2013.04.006

Chutcharavan, P. M., Dutton, A., & Ellwood, M. J. (2018). Seawater 234U/238U recorded by modern and fossil corals. *Geochimica et Cosmochimica Acta*, *224*, 1–17. https://doi.org/10.1016/j.gca.2017.12.017

Delmas, R. J., Ascencio, J., & Legrand, M. (1980). Polar ice evidence that atmospheric CO2 20,000 yr BP was 50% of present. *Nature*, *284*, 155–157.

DePaolo, D. J., Lee, V. E., Christensen, J. N., & Maher, K. (2012). Uranium

comminution ages: Sediment transport and deposition time scales. *Comptes Rendus - Geoscience*, *344*(11–12), 678–687. https://doi.org/10.1016/j.crte.2012.10.014

DePaolo, D. J., Maher, K., Christensen, J. N., & McManus, J. (2006a). Sediment transport time measured with U-series isotopes: Results from ODP North Atlantic drift site 984. *Earth and Planetary Science Letters*, *248*(1–2), 394–410. https://doi.org/10.1016/j.epsl.2006.06.004

DePaolo, D. J., Maher, K., Christensen, J. N., & McManus, J. (2006b). Sediment transport time measured with U-series isotopes: Results from ODP North Atlantic drift site 984. *Earth and Planetary Science Letters*, *248*(1–2), 394–410. https://doi.org/10.1016/j.epsl.2006.06.004

Dunk, R. M., Mills, R. A., & Jenkins, W. J. (2002). A reevaluation of the oceanic uranium budget for the Holocene. *Chemical Geology*, *190*(1–4), 45–67. https://doi.org/10.1016/S0009-2541(02)00110-9

Esat, T. M., & Yokoyama, Y. (2006). Variability in the uranium isotopic composition of the oceans over glacial–interglacial timescales. *Geochimica et Cosmochimica Acta*, *70*(16), 4140–4150.

Firestone, R. B., Baglin, C. M., & Chu, F. S. Y. (1998). Table of Isotopes 8th ed. In *Wiley*.

Francois, R., Bacon, M. P., Altabet, M. A., & Labeyrie, L. D. (1993). Glacial/interglacial changes in sediment rain rate in the SW Indian Sector of subantarctic Waters as recorded by 230Th, 231Pa, U, and δ15N. *Paleoceanography*, *8*(5), 611–629.

Frank, M., Gersonde, R., Rutgers van der Loeff, M., Bohrmann, G., Nürnberg, C. G.,

Kubik, P. W., Suter, M., & Mangini, A. (2000). Similar glacial and interglacial export bioproductivity in the Atlantic sector of the Southern Ocean: Multiproxy evidence and implication for glacial atmospheric CO2. *Paleoceanography*, *15*(6), 642–658.

Galbraith, E. D., & Jaccard, S. L. (2015). Deglacial weakening of the oceanic soft tissue pump: Global constraints from sedimentary nitrogen isotopes and oxygenation proxies. *Quaternary Science Reviews*, *109*, 38–48. https://doi.org/10.1016/j.quascirev.2014.11.012

Glasscock, S. K., Hayes, C. T., Redmond, N., & Rohde, E. (2020). Changes in Antarctic Bottom Water Formation During Interglacial Periods. *Paleoceanography and Paleoclimatology*, *35*(8), 1–13. https://doi.org/10.1029/2020PA003867

Gourgiotis, A., Reyss, J. L., Frank, N., Guihou, A., & Anagnostou, C. (2011). Uranium and radium diffusion in organic-rich sediments (sapropels). *Geochemistry, Geophysics, Geosystems*, *12*(9). https://doi.org/10.1029/2011GC003646

Hasenfratz, A. P., Jaccard, S. L., Martínez-García, A., Sigman, D. M., Hodell, D. A., Vance, D., Bernasconi, S. M., Kleiven, H. F., Haumann, F. A., & Haug, G. H. (2019). The residence time of Southern Ocean surface waters and the 100,000-year ice age cycle. *Science*, *363*(6431), 1080–1084. https://doi.org/10.1126/science.aat7067

Hayes, C. T., Anderson, R. F., Fleisher, M. Q., Serno, S., Winckler, G., & Gersonde, R. (2013). Quantifying lithogenic inputs to the North Pacific Ocean using the long-lived thorium isotopes. *Earth and Planetary Science Letters*, *383*, 16–25.

Hayes, C. T., Martínez-García, A., Hasenfratz, A. P., Jaccard, S. L., Hodell, D. A.,

Sigman, D. M., Haug, G. H., & Anderson, R. F. (2014). A stagnation event in the deep south atlantic during the last interglacial period. *Science*, *346*(6216), 1514–1517. https://doi.org/10.1126/science.1256620

Hayes, C. T., McGee, D., Mukhopadhyay, S., Boyle, E. A., & Maloof, A. C. (2017). Helium and thorium isotope constraints on African dust transport to the Bahamas over recent millennia. *Earth and Planetary Science Letters*, *457*, 385–394. https://doi.org/10.1016/j.epsl.2016.10.031

Henderson, G. M. (2002). Seawater (234U/238U) during the last 800 thousand years. *Earth and Planetary Science Letters*, *199*(1–2), 97–110. https://doi.org/10.1016/S0012-821X(02)00556-3

Henderson, G. M., & Anderson, R. F. (2003). The U-series toolbox for paleoceanography. *Uranium-Series Geochemistry*, *52*, 493–531. https://doi.org/10.2113/0520493

Herbert Veeh, H., & Boström, K. (1971). Anomalous 234U/238U on the East Pacific rise. *Earth and Planetary Science Letters*, *10*(3), 372–374.

Huybers, P., & Langmuir, C. (2009). Feedback between deglaciation, volcanism, and atmospheric CO2. *Earth and Planetary Science Letters*, *286*(3–4), 479–491. https://doi.org/10.1016/j.epsl.2009.07.014

Jaccard, S. L., Galbraith, E. D., Martínez-Garciá, A., & Anderson, R. F. (2016). Covariation of deep Southern Ocean oxygenation and atmospheric CO2 through the last ice age. *Nature*, *530*(7589), 207–210. https://doi.org/10.1038/nature16514

Jaccard, S. L., Hayes, C. T., Martínez-García, A., Hodell, D. A., Anderson, R. F.,

Sigman, D. M., & Haug, G. H. (2013). Two modes of change in Southern Ocean productivity over the past million years. *Science*, *339*(6126), 1419–1423. https://doi.org/10.1126/science.1227545

Jaffey, A. H., Flynn, K. F., Glendenin, L. E., Bentley, W. C., & Essling, A. M. (1971). Precision measurement of half-lives and specific activities of U235 and U238. *Physical Review C*, *4*(5), 1889–1906. https://doi.org/10.1103/PhysRevC.4.1889

Kanfoush, S. L., Hodell, D. A., Charles, C. D., Janecek, T. R., & Rack, F. R. (2002). Comparison of ice-rafted debris and physical properties in ODP Site 1094 (South Atlantic) with the Vostok ice core over the last four climatic cycles. *Palaeogeography, Palaeoclimatology, Palaeoecology*, *182*(3–4), 329–349. https://doi.org/10.1016/S0031-0182(01)00502-8

Klinkhammer, G. P., & Palmer, M. R. (1991). Uranium in the oceans: Where it goes and why. *Geochimica et Cosmochimica Acta*, *55*(7), 1799–1806.

Knight, G. B., & Macklin, R. L. (1948). Half-life of U X1(Th234). *Phys. Rev.*, *74*, 1540–1541.

Ku, T. (1965). An evaluation of the U234/U238 method as a tool for dating pelagic sediments. *Journal of Geophysical Research*, *70*(14).

Ku, T., Knauss, K., & Mathieu, G. (1997). Uranium in open ocean: concentration and isotopic composition. *Deep Sea Research*, *24*, 1005–1017.

Lisiecki, L. E., & Raymo, M. E. (2005). A Pliocene-Pleistocene stack of 57 globally distributed benthic δ 18O records. *Paleoceanography*, *20*(1), 1–17. https://doi.org/10.1029/2004PA001071

Lovley, D. R., Roden, E. E., Phillips, E. J. P., & Woodward, J. C. (1993). Enzymatic iron

and uranium reduction by sulfate-reducing bacteria. *Marine Geology*, *113*(1–2), 41–53. https://doi.org/10.1016/0025-3227(93)90148-O

Lund, D. C., & Asimow, P. D. (2011). Does sea level influence mid-ocean ridge magmatism on Milankovitch timescales? *Geochemistry, Geophysics, Geosystems*, *12*(12), 1–26. https://doi.org/10.1029/2011GC003693

Lund, D. C., Asimow, P. D., Farley, K. A., Rooney, T. O., Seeley, E., Jackson, E. W., & Durham, Z. M. (2016). Enhanced east pacific rise hydrothermal activity during the last two glacial terminations. *Science*, *351*(6272), 478–482. https://doi.org/10.1126/science.aad4296

MacDougall, J. D., Finkel, R. C., Carlson, J., & Krishnaswami, S. (1979). Isotopic evidence for uranium exchange during low-temperature alteration of oceanic basalt. *Earth and Planetary Science Letters*, *42*(1), 27–34.

Maher, K., DePaolo, D. J., & Lin, J. C. F. (2004). Rates of silicate dissolution in deep-sea sediment: In situ measurement using 234U/238U of pore fluids. *Geochimica et Cosmochimica Acta*, *68*(22), 4629–4648. https://doi.org/10.1016/j.gca.2004.04.024

Mangini, A., & Dominik, J. (1979). Late Quaternary sapropel on the Mediterranean Ridge: U-budget and evidence for low sedimentation rates. *Sedimentary Geology*, *23*(1–4), 113–125.

Martin, A. N., Dosseto, A., & Kinsley, L. P. J. (2015). Evaluating the removal of non-detrital matter from soils and sediment using uranium isotopes. *Chemical Geology*, *396*, 124–133. https://doi.org/10.1016/j.chemgeo.2014.12.016

Nielsen, S. H. H., & Hodell, D. A. (2007). Antarctic ice-rafted detritus (IRD) in the South

Atlantic; indicators of iceshelf dynamics or ocean surface conditions? *Open-File Report - U. S. Geological Survey*, *4*(1999), Short Research Paper 020. https://doi.org/10.3133/of2007-1047.srp020

Nielsen, S. H. H., Hodell, D. A., Kamenov, G., Guilderson, T., & Perfit, M. R. (2007). Origin and significance of ice-rafted detritus in the Atlantic sector of the Southern Ocean. *Geochemistry, Geophysics, Geosystems*, *8*(12). https://doi.org/10.1029/2007GC001618

Orsi, A. H., Whitworth, T., & Nowlin, W. D. (1995). On the meridional extent and fronts of the Antarctic Circumpolar Current. *Deep-Sea Research Part I*, *42*(5), 641–673. https://doi.org/10.1016/0967-0637(95)00021-W

Purcell, K., Hillaire-marcel, C., Vernal, A. De, Ghaleb, B., & Stein, R. (2022). Potential and limitation of 230 Th-excess as a chronostratigraphic tool for late Quaternary Arctic Ocean sediment studies : An example from the Southern Lomonosov Ridge. *Marine Geology*, *448*(February), 106802. https://doi.org/10.1016/j.margeo.2022.106802

Redfield, A. C. (1958). THE BIOLOGICAL CONTROL OF CHEMICAL FACTORS IN THE ENVIRONMENT. *American Scientist*, *46*(3), 205–221.

Reyss, J. L., Lamitre, N., Bonte, P., & Franck, D. (1987). Anomalous $^{234}U/^{238}U$ ratios in deep-sea hydrothermal deposits. In *Nature* (Vol. 325, pp. 798–800).

Robinson, L. F., Belshaw, N. S., & Henderson, G. M. (2004). U and Th concentrations and isotope ratios in modern carbonates and waters from the Bahamas. *Geochimica et Cosmochimica Acta*, *68*(8), 1777–1789. https://doi.org/10.1016/j.gca.2003.10.005

Rohde, E. E., Hayes, C. T., Redmond, N., & Glasscock, S. K. (2021). Southern Ocean Oxygenation Changes Inferred From Redox-Sensitive Trace Metals Across Marine Isotope Stage 11. *Geochemistry, Geophysics, Geosystems*, *22*(8), 1–13. https://doi.org/10.1029/2021GC009921

Romaniello, S. J., Herrmann, A. D., & Anbar, A. D. (2013). Uranium concentrations and 238U/235U isotope ratios in modern carbonates from the Bahamas: Assessing a novel paleoredox proxy. *Chemical Geology*, *362*, 305–316. https://doi.org/10.1016/j.chemgeo.2013.10.002

Severmann, S., & Thomson, J. (1998). Investigation of the ingrowth of radioactive daughters of 238U in Mediterranean sapropels as a potential dating tool. *Chemical Geology*, *150*(3–4), 317–330. https://doi.org/10.1016/S0009-2541(98)00113-2

Shipboard Scientific Party. (1999a). Leg 177 summary. *Paleoceanography*, *177*.

Shipboard Scientific Party. (1999b). Site 1094. *Proceedings of the Ocean Drilling Program, 177 Initial Reports*, *177*. https://doi.org/10.2973/odp.proc.ir.177.109.1999

Sigman, D. M., Hain, M. P., & Haug, G. H. (2010). The polar ocean and glacial cycles in atmospheric CO2 concentration. *Nature*, *466*(7302), 47–55. https://doi.org/10.1038/nature09149

Thomas, A. L., Henderson, G. M., & McCave, I. N. (2007). Constant bottom water flow into the Indian Ocean for the past 140 ka indicated by sediment 231Pa/230Th ratios. *Paleoceanography*, *22*(4). https://doi.org/10.1029/2007PA001415

Vallières, S. (1997). FLUX D'URANIUM AU COURS DES PROCESSUS DIAGÉNÉTIQUES. In *L'UNIVERSITÉ DU QUÉBEC À MONTRÉAL* (Vol. 2).

Villa, I. M., Bonardi, M. L., De Bièvre, P., Holden, N. E., & Renne, P. R. (2016). IUPAC-IUGS status report on the half-lives of 238 U, 235 U and 234 U. *Geochimica et Cosmochimica Acta*, *172*, 387–392. https://doi.org/10.1016/j.gca.2015.10.011

Wilson, T. R. S., Thomson, J., Hydes, D. J., Colley, S., Culkin, F., & Sørensen, J. (1986). Oxidation fronts in pelagic sediments: Diagenetic formation of metal-rich layers. *Science*, *232*, 972–975.

Zheng, Y., Anderson, R. F., Van Geen, A., & Fleisher, M. Q. (2002). Preservation of particulate non-lithogenic uranium in marine sediments. *Geochimica et Cosmochimica Acta*, *66*(17), 3085–3092. https://doi.org/10.1016/S0016-7037(01)00632-9

Zhou, Y., & McManus, J. (2022). Extensive evidence for a last interglacial Laurentide outburst (LILO) event. *Geology*, *50*.

CHAPTER III – ZONAL BOUNDARY SCAVENGING OF THE NORTH AND EQUATORIAL PACIFIC: ^{230}TH AND ^{231}PA FROM GEOTRACES GP15

3.1 Abstract

An important role in the biogeochemical cycling of trace metals in the marine environment is scavenging, the adsorption and removal of elements by sinking particles. In some cases, knowledge of scavenging processes can inform us about other modern and past marine processes such as circulation, nutrient availability, or dust deposition. Boundary scavenging, the enhanced removal of elements in areas of high particle flux, is an important but poorly constrained process, especially in the Pacific where there are stark changes in the processes that drive particle scavenging such as productivity fronts, hydrothermal activity, and benthic resuspension. Here we present a water column transect of dissolved ^{230}Th and ^{231}Pa along 152° W between Alaska and Tahiti (GEOTRACES GP15). These radioisotopes are produced uniformly in the ocean by U decay but are differentially affected by scavenging. The motivation behind observing these ^{230}Th and ^{231}Pa distributions is to understand the relative role of multiple scavenging effects and to consider the implications for the method of ^{230}Th-normalization for particle flux or burial estimates. Our observations show that the scavenging intensities of both ^{230}Th and ^{231}Pa in the upper 2000 m of the North & Equatorial Pacific is set by the reversible scavenging of biogenic particles and related to major biogeochemical province. Deviations from reversible scavenging identified two other major scavenging processes: advection of hydrothermally scavenged water along 10°N and 12°S, and benthic features related to the ventilation of bottom water. We show that the lateral gradients in ^{230}Th concentration expected from the contrast in particle load between the subtropical gyres and the

Equatorial Particle Veil are functionally erased by the advection of adjacent, hydrothermally scavenged water. Hydrothermal boundary scavenging and its effect on ^{230}Th transport is potentially substantial and warrants additional consideration when using ^{230}Th to normalize burial flux in these areas. The boundary between the subarctic and subtropical gyres is shown to be latitudinally narrow, within 500 km, and located near the annually averaged productivity front. Lastly, benthic anomalies of $^{230}Th_{xs}$ provide evidence of regional contrasts in ventilation by Lower Circumpolar Deep Water, with relatively vigorous circulation inducing nepheloid layers near 20° N and sluggish, cyclonic recirculation creating bottom sediment dissolution around 40° N.

3.2 Introduction

Scavenging, the process by which elements adsorb to ocean particles and sink to depth, is an important mechanism for understanding the marine cycling of trace metals (Goldberg, 1954). Scavenging has implications for bioavailability of micronutrients such as Fe (Tagliabue et al., 2019), Cu (Richon & Tagliabue, 2019), and Co (Bown et al., 2011), and on the distribution of important paleoceanographic proxies for dust, such as Al (Hsieh et al., 2011; Hydes, 1983) and Th (Anderson et al., 2016), or overturning circulation, such as Pa (Lippold et al., 2011). Boundary Scavenging is the preferential scavenging and removal of particle-reactive species in areas of higher particle flux (Anderson et al., 1983; Bacon et al., 1976; Spencer et al., 1981) such as continental margins (Anderson et al., 1990; Roy-Barman, 2009), areas of increased particulate matter rain, aeolian dust input, benthic particle resuspension, and between some hydrographic features across oceanic biogeochemical boundaries (Hayes et al., 2013). As these boundary effects represent an important control of the distribution of dissolved trace

metals (Bruland et al., 2014), and thereby their ultimate sink to the seafloor, it is important to understand global boundary scavenging and its implications for reconstructing sediment archives.

One method for studying how changes in scavenging regimes affect trace metal removal is the use constant flux proxies such as ^{230}Th (Bacon, 1984; Francois et al., 2004). ^{230}Th (half-life of 75.58 x 10^3 y, Cheng et al., 2013) and ^{231}Pa (half-life of 32.76 x 10^3 y, Robert et al., 1969) are both long-lived radionuclides with high affinity to adsorb to marine particles. The input of both ^{230}Th and ^{231}Pa is almost entirely derived from the decay of uniformly distributed ^{234}U and ^{235}U, respectively, (Andersen et al., 2010; Delanghe et al., 2002; Robinson et al., 2004; Weyer et al., 2008) at a production activity ratio of ^{231}Pa/^{230}Th = 0.093 (Henderson & Anderson, 2003). As this production of Th and Pa is constrained and stable in the marine system (Costa et al., 2020), it is balanced by its removal terms including scavenging to sinking particles, redistribution from ocean circulation, and sedimentation to the seafloor (Hayes et al., 2015). These properties make these elements appealing as proxies to trace the processes for which they are involved. Unlike their U parents, Th and Pa are both highly insoluble in seawater, but they vary in their degree of solubility with Th's residence time being < 40 y (Bacon & Anderson, 1982) and Pa at < 200 y (Henderson & Anderson, 2003). This difference leads to the expectation that Th is limited in the spatial extent of isopycnal mixing and will scavenge "in-place" such that its concentration is inversely proportional to scavenging intensity (Hayes et al., 2013). Alternatively, Pa is drawn down by scavenging more slowly than Th and has enough time to transport that it will be preferentially removed via boundary scavenging. As the drawdown of Th into sediment is relatively quick, the ratio of

dissolved $^{231}Pa/^{230}Th$ in seawater is functionally determined by processes dictating Pa mobility during its longer residence time. This can be driven by the physical transport of Pa, such as advection/circulation (Yu et al., 2001) or mixing along strong diffusive gradients (Pavia et al., 2020), as well as processes altering the strength of Pa removal to scavenging, such as export productivity (Francois et al., 1993), particle composition affinity (Chase et al., 2002; Gueguen & Guo, 2002), or hydrothermal fluxes (Hayes et al., 2015). The expectation for these combined processes as part of the boundary scavenging model is that dissolved $^{231}Pa/^{230}Th$ (hereafter written as Pa/Th) should be higher in regions of high scavenging and is ultimately buried with this enriched signature.

The current model traditionally used to understand ^{231}Pa and ^{230}Th distributions with depth is a one-dimensional reversible scavenging model where the dissolved and particulate phases continuously exchange as particles sink to depth (Bacon & Anderson, 1982). This model predicts that dissolved concentrations of Pa and Th should linearly increase with depth and that the slope of said increase is determined by the intensity of scavenging. Another consequence of this behavior is that the total inventory of dissolved Pa and Th in the water column is lower where scavenging is higher. Deviations from a reversible scavenging profile must thereby reflect changes in local scavenging behaviors or as signatures from areas where scavenging is different (Hayes et al., 2013; Pavia et al., 2019). Previous studies have used this linear slope as a baseline for identifying and quantifying hydrothermal scavenging (Deng et al., 2014; Hayes et al., 2015; Lopez et al., 2015; Pavia et al., 2018). This study focuses on the variations in ^{230}Th and ^{231}Pa scavenging intensity and implications for ^{230}Th transport. A future study, likely involving ocean biogeochemical modeling, will be necessary to fully evaluate ^{231}Pa transport.

Ultimately, the processes that affect scavenging in the modern ocean are vital to understanding how certain elements are removed to the seafloor over time. Sedimentary ^{230}Th concentrations are a useful tool for reconstructing past burial rates without specifically needing to date the sediment for age tie points. As ^{230}Th production from decay is relatively uniform in both space and time and it is buried relatively quickly into sediment, changes to excess ^{230}Th, ^{230}Th not supported by uranium decay from with the sediments, theoretically reflect variable changes to sediment mass flux (Bacon, 1984; Costa et al., 2020; Francois et al., 2004). However, this technique, ^{230}Th normalization, can be complicated in areas where the flux of ^{230}Th from production does not equal the flux of ^{230}Th to the seafloor via scavenging. The flux-to-production ratio of ^{230}Th can vary due to sediment remobilization or where scavenging boundaries drive lateral mixing. In this study, we will explore uncertainties of the flux-to-production ratio of various Pacific scavenging boundaries and comment on their potential effects on ^{230}Th normalization.

3.3 Methods

3.3.1 Cruise Setting and Shipboard Collection

GP15 (Fig. 3.1) is a meridional transect along the 152° W between Alaska and Tahiti, taken by the R/V Roger Revelle from Sep – Oct 2018 as part of the GEOTRACES program (www.geotraces.org). GP15 transverses many hydrographic features that potentially impact scavenging such as benthic particle resuspension at the Alaskan Margin, dust flux from the tail end of Asian sources, strong export productivity with differing particle composition at the Intertropical Convergence Zone and the Transition Zone Chlorophyll Front, and hydrothermal activity from the East Pacific Rise and

hotspots like Loihi Seamount. Twenty-five profiles of dissolved ^{232}Th, ^{230}Th, and ^{231}Pa were taken including 5 super stations (where additional hydro casts were taken and particle resolution was increased), 15 regular stations (measuring the full suite of GEOTRACES parameters), 2 shelf stations, and 3 slope stations (Fig. 3.1). Stations provide relatively high-resolution sampling for this type of analysis, covering roughly every 500 km in the open ocean or less at the Alaskan Margin, Hawaii, and across the equator and most stations consisting of greater than 20 depth measurements. For each, 5 or 10L of 0.45 μm filtered water was collected via Niskin bottles and acidified to a pH of 1.5 for storage. Samples were processed by three labs; at the Lamont-Doherty Earth Observatory at Colombia University in New York, at the University of Minnesota, and at the University of Southern Mississippi. Both the shipboard collection of water and the later processing of seawater samples were done using GEOTRACES standard protocol (Anderson et al., 2012), with some slight modifications as detailed below.

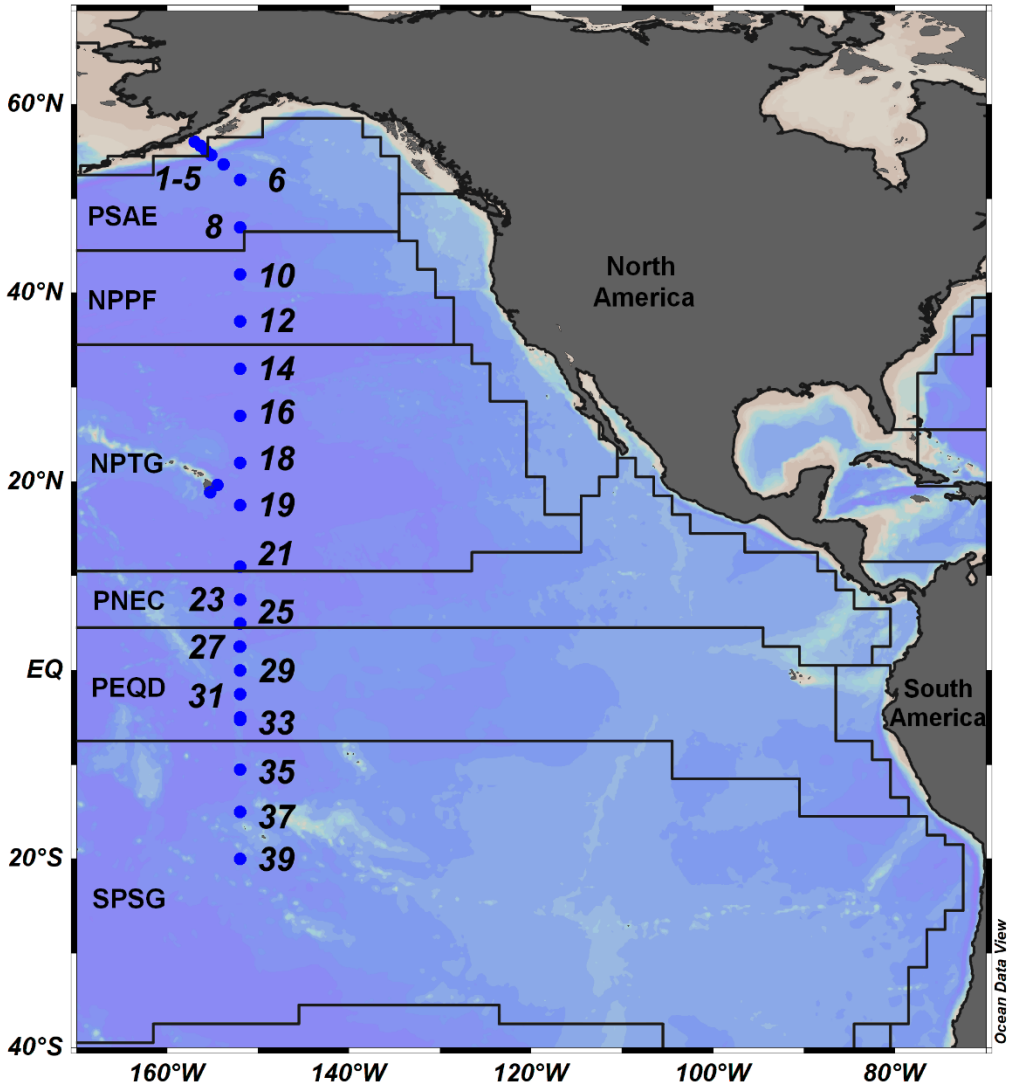

Figure 3.1 *Map of GEOTRACES GP15*

Map of GEOTRACES GP15 showing station numbers where Th and Pa measurements were taken. GP15 crosses many biogeochemical boundaries (black lines, Longhurst, 1995) that may have implications for scavenging regime. Biogeochemical provinces labeled from north to south; Eastern Pacific subarctic gyres (PSAE), North Pacific polar front (NPPF), North Pacific Tropical Gyre (NPTG), North Pacific equatorial counter current (PNEC), Pacific equatorial divergence (PEQD), and South Pacific gyre (SPSG).

3.3.2 Dissolved Th and Pa

The data presented here was produced by 3 collaborating labs. Details for analytical procedures followed at the LDEO and University of Minnesota labs will be forthcoming. Here we describe the procedure for processing dissolved Th and Pa done at USM, which are modified from Anderson et al., 2012, Auro et al., 2012, and Hayes et al., 2015c. Th and Pa concentrations were determined by isotope dilution via inductively coupled plasma-mass spectrometry (ICP-MS) using an Element XR instrument and an ESI Spiro-Apex for sample introduction. Acidified water samples were spiked with aliquots of ^{229}Th and ^{233}Pa and allowed to equilibrate for 1 day. The Th and Pa were then co-precipitated as Fe (oxy)hydroxide using added $FeCl_3$ and pH adjustment using ammonium hydroxide. The Fe precipitate was then digested in a series of HF, HCl, and HNO_3 (OPTIMA grade) and then elements were separated by anion exchange column chromatography using BioRad AG1-X8 resin. Water samples were analyzed in batches of 14 to 22 (12 batches total). Procedural blanks were determined by processing 4-5 L of Milli-Q H_2O in an acid-cleaned cubitainer acidified to pH ~2 with 6 M HCl (OPTIMA grade) as a sample in each batch (n = 12 total procedural blanks). A smaller number (n = 3) of "at-sea" blanks were analyzed which were cubitainers filled with MQ-H_2O and acidified at sea. "At-sea" blanks fell into the range of procedural blanks measured at USM which were (mean ± SD): 32 ± 26 pg ^{232}Th, 1.4 ± 0.8 fg ^{230}Th and 0.8 ± 0.9 fg ^{231}Pa, which in general were less than 10% of measured samples with the following exceptions. Out of 190 water samples analyzed at USM, 6 were flagged for potential ^{232}Th contamination based on oceanographic consistency and 23 were flagged as below detection for ^{231}Pa.

Intercalibration between labs was done by alternating profile locations and running a standard aliquot of artificial seawater with each sample batch (SWS2010-1 and SWS2015-1). The USM results for these standards were: 1058 ± 111 pg/g ^{232}Th, 262 ± 26 fg/g ^{230}Th and 33.1 ± 6.1 fg/g ^{231}Pa for SWS2010-1 (n = 7) and 178 ± 2 pg/g ^{232}Th, 205 ± 1 fg/g ^{230}Th and 41.5 ± 2.4 fg/g ^{231}Pa for SWS2015-1 (n = 5). Our results for SWS2010-1 are within the consensus range from the intercalibration exercise (Anderson et al., 2012). Consensus values for SWS2015-1 have not yet been coordinated but they agree with the reports of the LDEO lab. As an additional measure of our internal consistency, we analyzed a set of 4 replicate samples that were Niskin bottles fired at the same depth at a station but from a different cast (casts were designed to overlap for at least one depth). Our percent error agreement with these replicates were similar to the percent relative standard deviation of the reference material solution results given above. Measured radionuclide concentrations were corrected for two factors; 1. For the ingrowth of ^{231}Pa and ^{230}Th by U decay during storage, and 2. For lithogenic contribution of ^{231}Pa and ^{230}Th based on measured ^{232}Th concentrations. Data corrected in this manner are designated with the subscript xs. The ingrowth correction is about 0.4 μBq/kg/yr for ^{230}Th and 0.04 μBq/kg/yr for ^{231}Pa. This correction is nearly negligible for ^{231}Pa, but significant for ^{230}Th, especially for samples from the upper ~500 m whose concentrations can fall below 1 μBq/kg and some of which were analyzed>2 years after collection. The xs correction was between 0.1% - 7% for ^{230}Th and 0.01% - 2% for ^{231}Pa.

3.3.3 Suspended Particulate Matter and He Isotopes

The full details for the determination of suspended particulate mass (SPM) can be found in Lam et al., 2018 and the specifics for GP15 will be presented in a forthcoming

publication. Briefly summarized, total SPM is estimated by the combined chemical dry weight of the major particulate phases; particulate organic matter, opal, calcium carbonate, lithogenic material, and Fe / Mn oxyhydroxides. SPM is presented as inventories integrating the total particle mass between 500 – 4000 m. Concentrations of suspended particles are expected to rapidly decrease in the surface ocean, reaching a clear water minimum in the middle of the water column (Biscaye & Eittreim, 1977). In absence of benthic influence, this particle concentration can remain low, however nepheloid layers will cause particle concentrations below the clear water minimum to increase towards the bottom (Biscaye & Eittreim, 1977). The upper limit of this depth was set to avoid uncertainty with the most extreme changes in particle concentrations and the lower limit was set to avoid changes due to potential nepheloid layers. The inventories presented function as a first order estimate for the total background scavenging intensities. Although SPM particles have a much shorter residence time than ^{230}Th at these depths (months vs years), however, seasonal change in SPM at our study location are expected to be much smaller than the change between certain biogeochemical regions, making the relationship between SPM and ^{230}Th to still potentially be useful.

Helium concentrations and isotopic composition were measured by gas-extraction and mass spectrometry following the methods of Young & Lupton, 1983, and standardized following Jenkins et al., 2019. Results specific to GP15 can be found in Jenkins et al., 2020.

3.4 Results

3.4.1 Distribution of ^{230}Th

^{230}Th concentrations generally increased with depth and were overall lowest in the Subarctic Gyre (stations 4 – 12), highest in both subtropical gyres (stations 14 – 25 and 33 – 39), and intermediate narrowly around the Equator (stations 27 – 31) (Fig. 3.2A). Upper water column (0 - ~2000 m) ^{230}Th concentration distributions were relatively similar within each of these four biogeochemical provinces (Fig. 3.3) and showed linear concentration-depth profiles (Fig. 3.4, red lines), consistent with a reversible scavenging model. SPM inventories, used to show the general biogenic scavenging regime, were also similar throughout each biogeochemical province (Fig. 3.3) and significantly correlated with ^{230}Th concentration-depth slope (Fig. 3.5). Deviations from linear concentration-depth profiles (see discussion) occurred mainly in two sections: (1) below 4000 m in all stations besides the Subarctic Gyre, and (2) below 2000 m surrounding the equatorial region at stations 23 – 39.

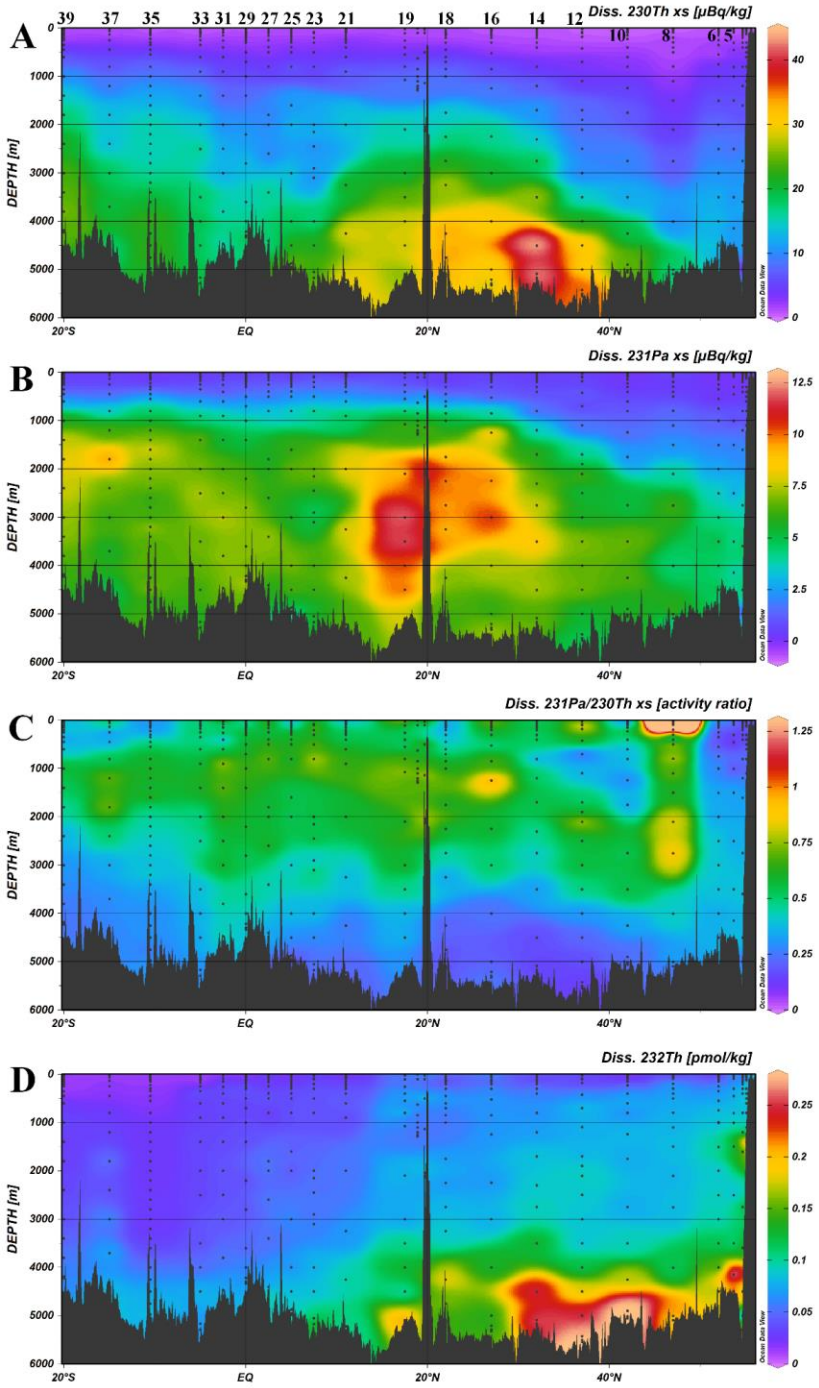

Figure 3.2 *Dissolved element sections at GP15*

Dissolved element sections at GP15. A – Dissolved $^{230}Th_{xs}$ (µBq/kg). B – Dissolved $^{231}Pa_{xs}$ (µBq/kg). C - $^{231}Pa_{xs}/^{230}Th_{xs}$ (activity ratio). D – Dissolved ^{232}Th (pmol/kg).

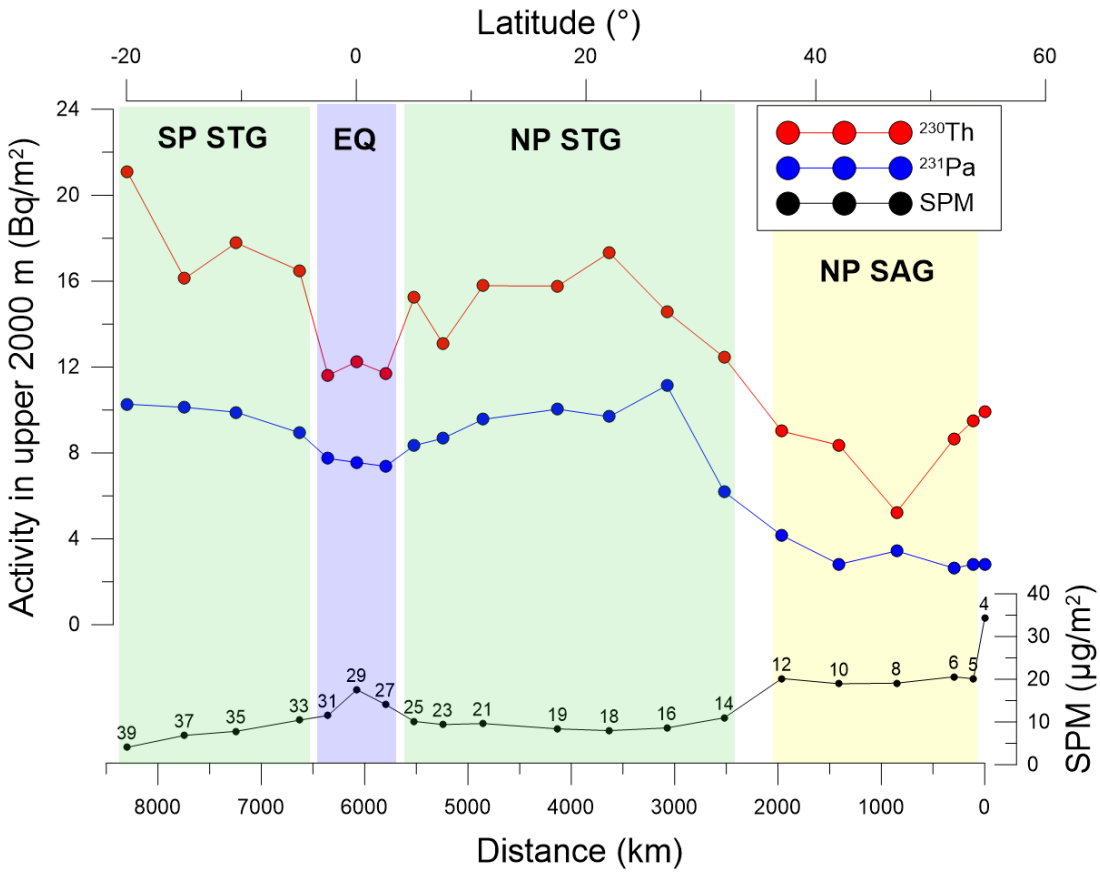

Figure 3.3 *Inventories of ^{230}Th and ^{231}Pa over biogeochemical provinces*

Upper water column (<2000 m) inventory of ^{230}Th (red) and ^{231}Pa (blue) in Bq/m^2. Suspended Particulate Matter inventories (SPM, black) are calculated between 500 – 4000 m depth (µg/m^2) and are used to show the general scavenging setting. These regions correspond to the North and South Pacific Subtropical Gyres (SP STG and NP STG respectively, green), the Equatorial Particle Veil (EQ, light blue), and the North Pacific Subarctic Gyre (NP SAG, yellow). Both subtropical gyres have relatively higher activities of ^{230}Th and ^{231}Pa, intermediate activities at the Equatorial Particle Veil, and lowest activities in the Subarctic Gyre. This difference in ^{230}Th and ^{231}Pa activity between regions is on roughly the same scale between the subtropical and subarctic gyres, however the difference in ^{231}Pa activity at the equator is muted compared to ^{230}Th.

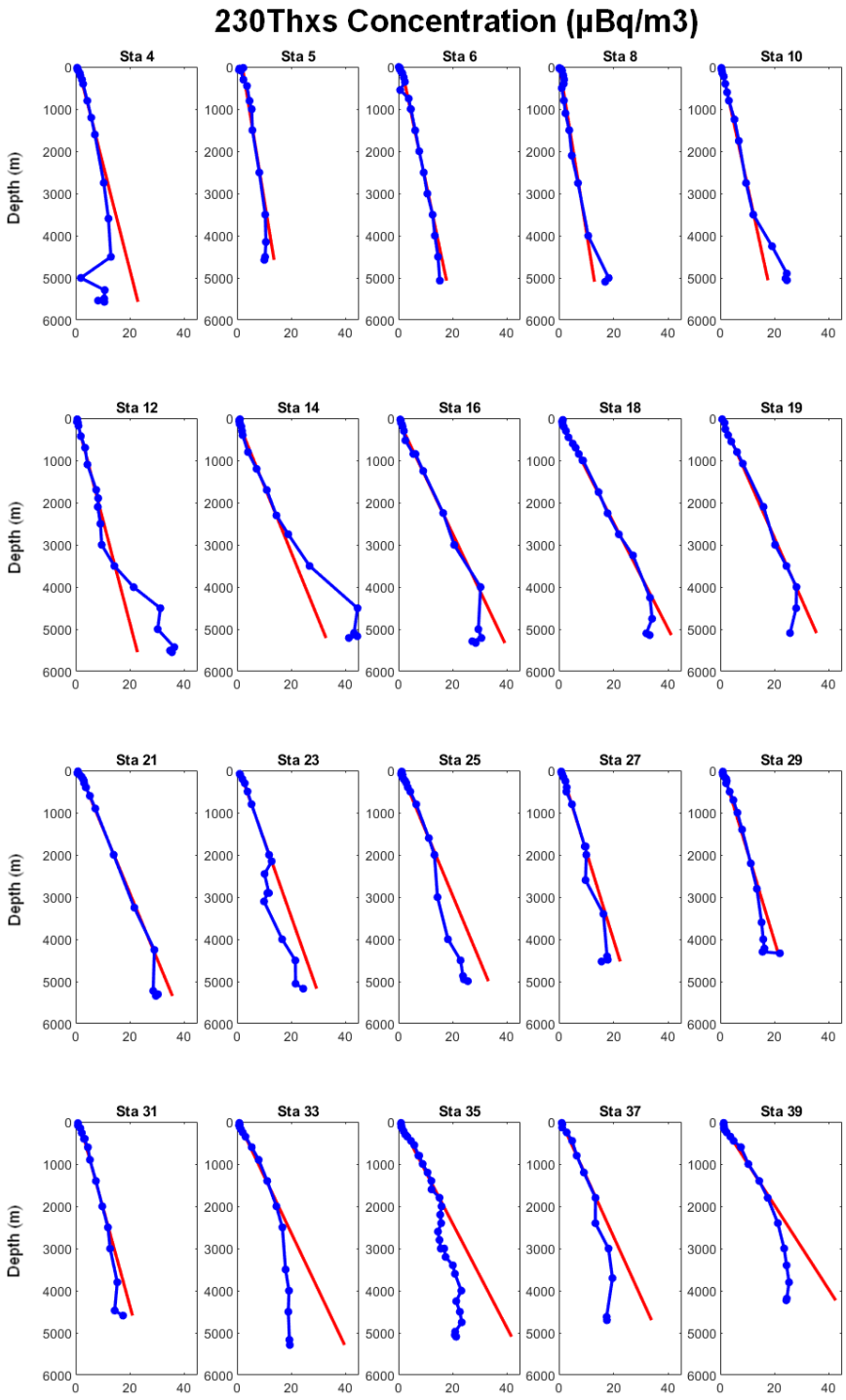

Figure 3.4 *Profiles of observed and predicted $^{230}Th_{xs}$*

Profiles (µBq/m^3 vs m depth) of observed (blue) profiles of $^{230}Th_{xs}$ and profiles of $^{230}Th_{xs}$ as predicted by reversible scavenging (Red). Reversible scavenging was predicted by linear regression between the first sample below the maximum seasonal mixed layer and the successive points (minimum 2000 m) that maximizes the coefficient of determination (R^2). All stations had an $R^2 > .97$.

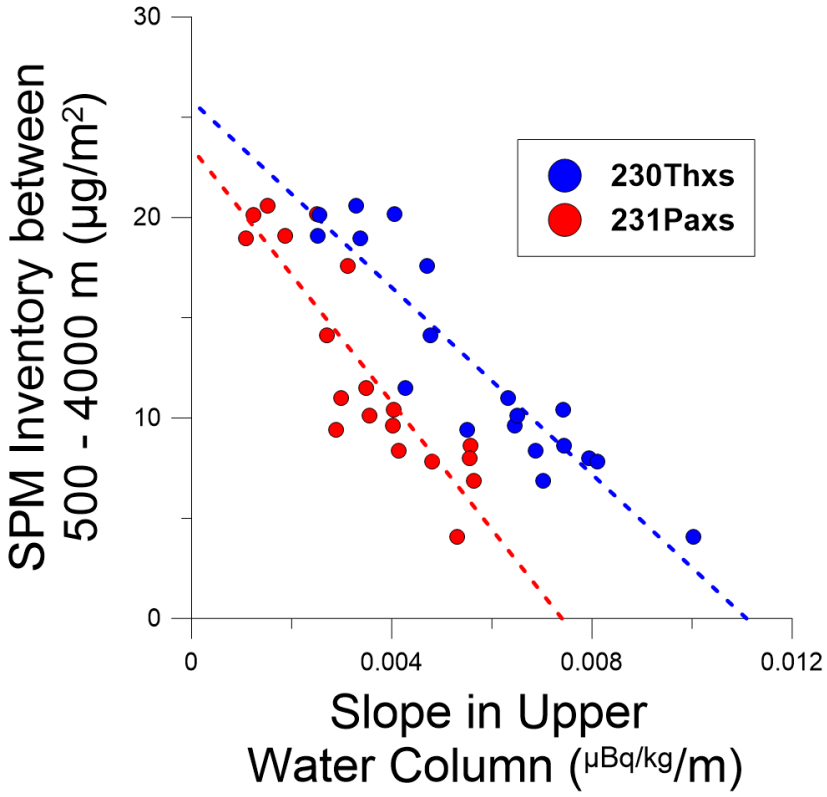

Figure 3.5 *Suspended Particulate Matter vs the slope of upper water column concentrations of ^{230}Th and ^{231}Pa*

Suspended Particulate Matter (µg/m^2) vs the slope (ΔµBq/kg/m) of upper water column concentrations of ^{230}Th and ^{231}Pa between stations 5 and 39. Both elements share similar relationship and are both statistically significant.

3.4.2 Distribution of ^{231}Pa

The distribution of ^{231}Pa can generally be characterized into two distinct regions: the Subtropical Gyre and the remaining Pacific (Fig. 3.2B), which varied in both total ^{231}Pa inventory and the shape of ^{231}Pa concentration distribution. Total inventories of ^{231}Pa were significantly lower in the Subarctic Gyre (4 – 12) than in the other biogeochemical provinces. The inventory of ^{231}Pa in the upper 2000 m is generally lower than and follows the same distribution patterns as ^{230}Th, however the difference in the equatorial region is muted compared to the surrounding gyres (Fig. 3.3). The Subarctic

Gyre was characterized by a strong linear concentration-depth relationship throughout the water column, whereas the subtropical gyres and equatorial Pacific showed linear ^{231}Pa concentration-depth profiles in the upper ocean (Fig. 3.6) and depleted values below 1500 – 2000 m. These subsurface depletions in ^{231}Pa concentration with depth occurred shallower in the water column than their ^{230}Th counterparts and occurred throughout the North Pacific Subtropical Gyre where similar depletions were not observed. In some cases, the central stations of the North Pacific Subtropical Gyre have more prominent subsurface maxima in ^{231}Pa concentration than the rest of the region. Unlike ^{230}Th, the inventory of ^{231}Pa in the upper water column of the Pacific is not thought to reflect production in seawater due to its higher mobility. The reversible scavenging of upper ^{231}Pa distribution and the similarity in the relationship between SPM (Fig. 3.5) both elements might imply that any change in upper ^{231}Pa inventory from production happen relatively homogeneous throughout the basin.

The $^{231}Pa_{xs}/^{230}Th_{xs}$ (Fig. 3.3C) of GP15 falls above the activity production ratio of .093 throughout the entire section. The North Pacific Subarctic Gyre has a relatively homogeneous, low $^{231}Pa_{xs}/^{230}Th_{xs}$ throughout. The subtropical gyres and equatorial regions are divided with depth and have relatively higher $^{231}Pa_{xs}/^{230}Th_{xs}$ in the upper 3000 m and much lower values in the lower and upper deep water.

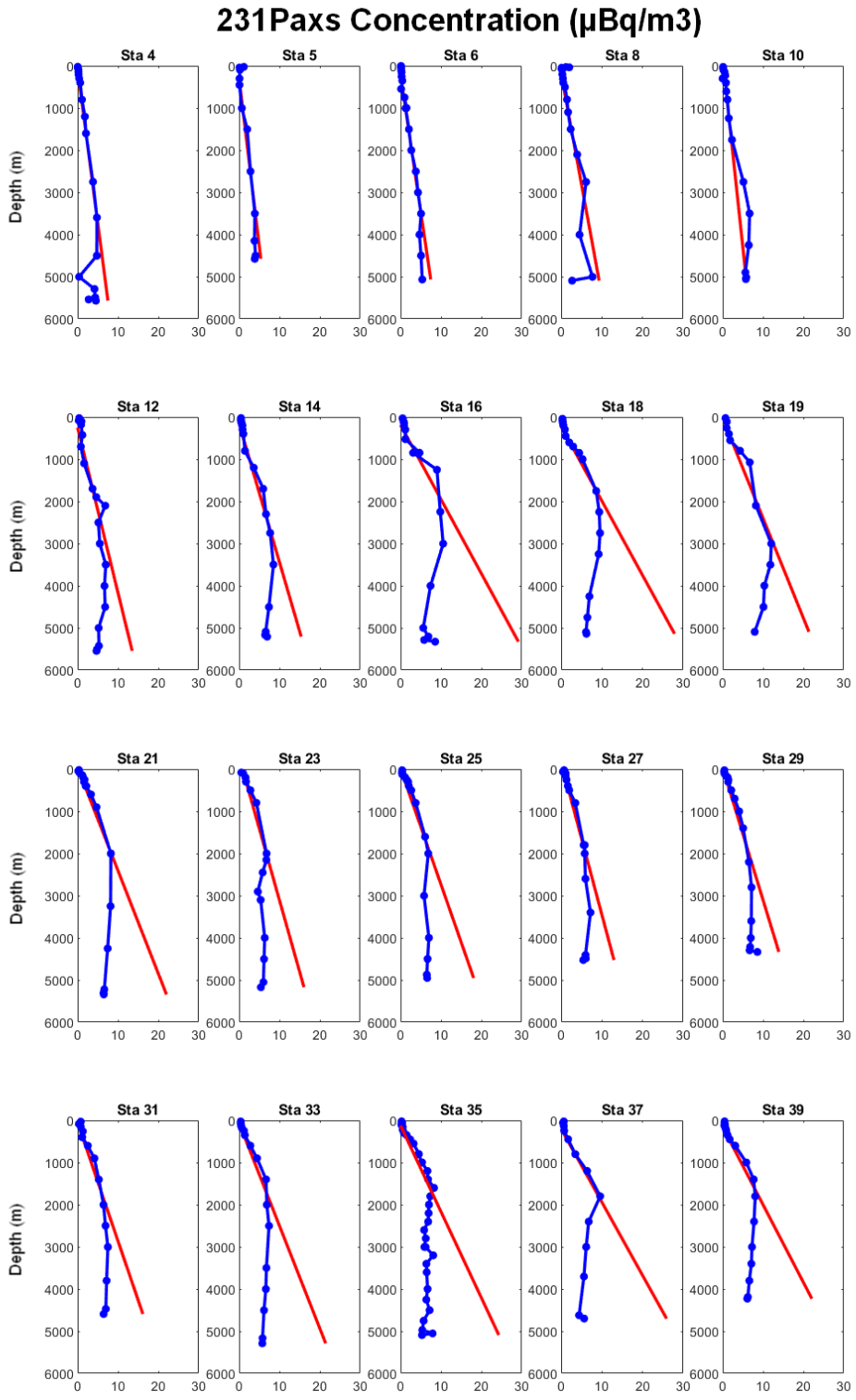

Figure 3.6 *Profiles of observed and predicted* $^{231}Pa_{xs}$

Profiles (µBq/m^3 vs m depth) of observed $^{231}Pa_{xs}$ (blue) and profiles of $^{231}Pa_{xs}$ as predicted by reversible scavenging (Red). $R^2 > .874$.

3.4.3 Distribution of ^{232}Th

The inventory of ^{232}Th is generally low throughout, however is more depleted in the southern half of the transect (stations 21 – 39) where dust flux is expected to be the lowest (Fig. 3.2D). North of station 21, where there is potentially influence from Asian dust, ^{232}Th concentrations are elevated slightly throughout the water column. However, unlike the homogeneous concentration-depth distribution expected from a dust source, ^{232}Th concentrations below 3000 m in this region are elevated with proximity to the bottom, indicating some type of benthic resuspension or influence on the distribution of this element.

3.4.4 SPM vs ^{230}Th and ^{231}Pa

Suspended particulate matter (SPM) plays a major role in the removal of adsorption-prone elements and can be used as a general indicator for scavenging conditions. We observe that SPM significantly correlates with upper water column slopes from stations 5 – 39 (lower slopes have a lower total inventory, see discussion for calculation) for both ^{230}Th and ^{231}Pa (Fig. 3.5). The relationships are as follows: Thorium: SPM = -2329 * m^{230}Th + 25.823, R^2 = 0.8417, and Protactinium: SPM = -3177.1 * m^{231}Pa + 23.479, R^2 = 0.7819, where SPM is the inventory of SPM between 500 - 4000 m and m is the slope (ΔμBq/kg/m) of each element as predicted by upper water column slope. This relationship shows that scavenging by biogenic particles forms the backdrop for ^{230}Th and ^{231}Pa distribution in the upper 2000 m of the Pacific and potential shows that deviations from this profile are not biogenic in nature.

3.5 Discussion

3.5.1 Isolating the Scavenging Terms of ^{231}Pa and ^{230}Th

Here we predict reversible scavenging by projecting a slope from concentration measurements in the upper water column (Fig. 3.4 and Fig. 3.6). Deviations from this reversible scavenging profile should reflect local changes to scavenging behavior. Methodologies to predict reversible scavenging ^{230}Th and ^{231}Pa profiles have previously been used for GEOTRACES GP16 Eastern Pacific Zonal Transect (~10° - 17° S) (Pavia et al., 2018). The rationale behind this was that as variance is low in the upper water column where reversible scavenging is the driving process behind ^{230}Th and ^{231}Pa distribution with depth, an increase in this variance identifies where other processes affect element distribution. This linear regression is projected to depth, where deviations from it can be inferred as the effect from scavenging processes outside of reversible scavenging. For GP16, this prediction was done by performing a linear regression on 11 combined stations from 112° – 152° W between 300 - 1500 m depth. The upper limit of this depth range was below the influence of seasonal vertical mixing and the lower limit was above any hydrothermal influences. For GP15 additional consideration is warranted. For example, GP15 crosses hydrographic zones of varying scavenging intensity, leading to the expectation that upper water column ^{230}Th and ^{231}Pa slopes might vary dramatically between stations. Additionally, some features that can affect ^{230}Th and ^{231}Pa concentration at depth, like hydrothermal or benthic influence, do not apply to every station at GP15. To accommodate these differences, first, we do a linear regression for each individual station in order to account for regional biogeochemical distribution changes and, second, use various window sizes to account for different potential

influences with depth. Linear regressions were run starting from the maximum seasonal mixed layer depth to a minimum depth of 2000 m. This choice of depth was for much the same reason as in GP16; to avoid changes in ^{230}Th and ^{231}Pa distribution from mixing and subsurface hydrothermal influence near the equator. The size of these windows was then increased by including successive samples deeper than 2000 m if the coefficient of determination (R^2) was increased by doing so. For the regression of $^{230}Th_{xs}$ at each station, n ranged from 6 - 15, R values were >0.98, and all p values were < 0.0023 respectively. For $^{231}Pa_{xs}$, n ranged from 6 - 16, R values were >0.936, and all p values were <0.002 respectively. Although the linear regression for each station is made over a different depth range, the regressions for all stations and elements were strongly significant. This sliding window method is useful because it can be used to compare stations that have different sample numbers and accounts for sample aliasing with depth, but with the potential pitfall that comparing slopes from different regions requires knowledge of the processes influencing ^{230}Th and ^{231}Pa profiles with depth to make these comparisons.

Deviations from reversible scavenging in $^{230}Th_{xs}$ profiles identify two major areas where local processes impact scavenging; 1. Hydrothermal scavenging adjacent to the Equator below 2000 m, and 2. Benthic scavenging in the North Pacific Subtropical Gyre below 4000 m. Apart from some small deviations in the upper 300 m of some subarctic stations, ^{230}Th concentration profiles in the upper 2000 m were extremely linear, consistent with reversible scavenging. Similarly, ^{231}Pa profiles were also linear to up to 1500 – 3000 m.

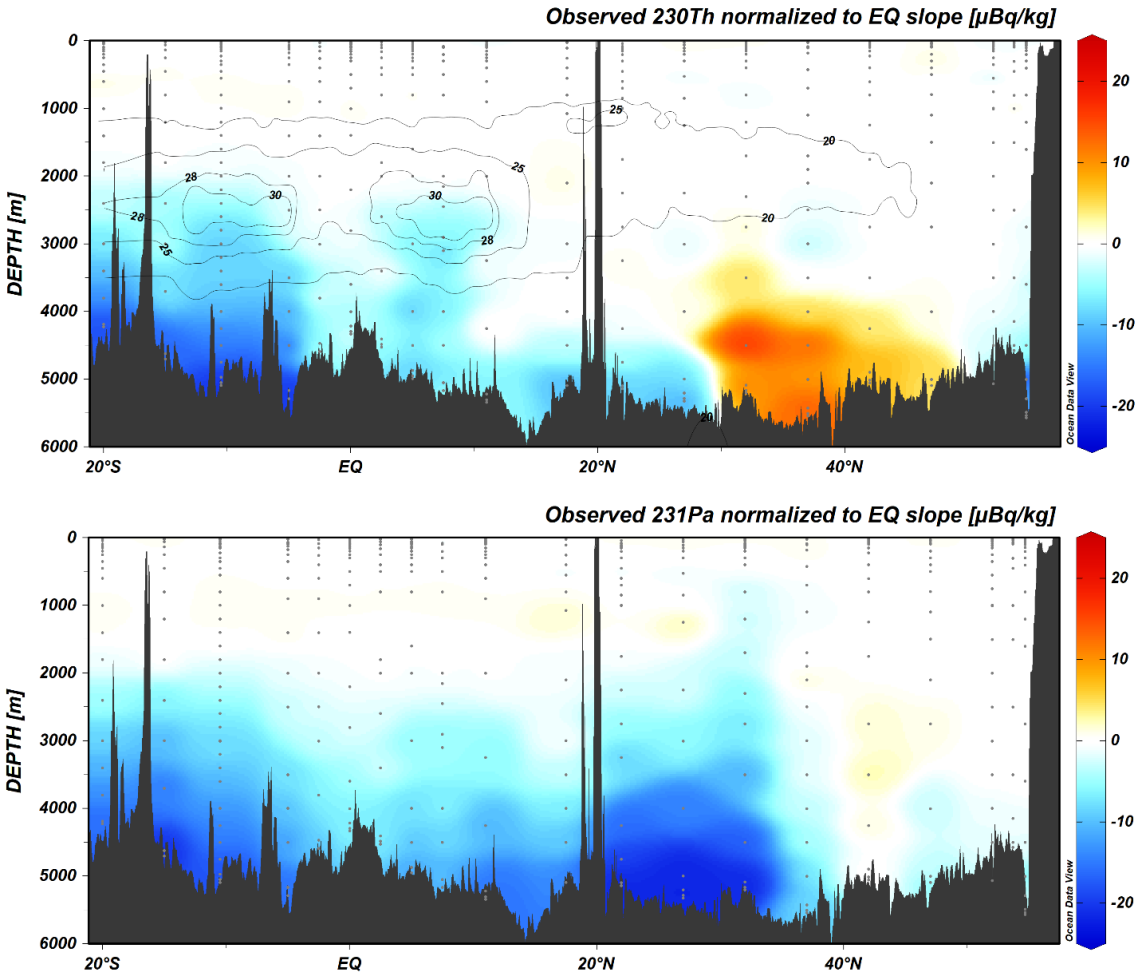

Figure 3.7 *Section of $^{230}Th_{xs}$ and $^{231}Pa_{xs}$ anomaly*

$^{230}Th_{xs}$ and $^{231}Pa_{xs}$ anomaly as the difference between the concentration predicted by reversible scavenging minus observed concentration (µBq/kg). Contours of δ^3He are shown on the top graph to identify the influence of hydrothermally influenced water.

3.5.2 Hydrothermal Scavenging

Hydrothermal activity plays an important part in regulating the chemistry of the Pacific Ocean, especially given the fast-spreading ridges of the East Pacific Rise. For example, dispersal of mantle-derived ^3He from the EPR has been used as a tracer for ocean circulation and mixing in the Pacific (Lupton, 1998). However, the extent to which hydrothermal activity can influence the basin-scale budget of trace element is still a

subject of debate. Its effects on far-field transport have been a recent topic of interest as studies found plumes of dissolve iron and manganese thousands of kilometers from vent sites (Bennett et al., 2008; Fitzsimmons et al., 2014; Saito et al., 2013). Distal metal scavenging of ^{230}Th and ^{231}Pa in the equatorial Pacific have been documented (Lopez et al., 2015; Pavia et al., 2018) and decreasing westward depletions of these elements below 1500 m is consistent with advection of plume waters. The degree to which scavenging by hydrothermal particles is happening *in-situ* at these distal locations or that this effect is derived from the advection of EPR vent fluid that has maintained its signature throughout its lifetime, is still subject to some debate, although the progressively smaller westward element depletions (Lopez et al., 2015; Okubo et al., 2012) and relatively low dissolved Fe/Mn (Pavia et al., 2018) seem to point to the latter. As GP15 crosses the tail end of both EPR plumes, it provides a specific opportunity to analyze the meridional extent of hydrothermal effects and its relationship to the equator as a boundary scavenging feature.

^{3}He is potentially useful as a deep water tracer for hydrothermal activity (Stuart et al., 1994); however, as ^{3}He is conservative, its presence does not necessarily indicate the presence of reactive particle phases such as Fe/Mn oxyhydroxides, making it difficult to isolate active hydrothermal scavenging from other effects. In the Pacific, the complications of using ^{3}He as a hydrothermal tracer are doubly so as ^{3}He/^{4}He ratios are elevated throughout the basin in respect to the global ocean. The relationship between He isotopes and metal scavenging may be useful in some cases even if they are not always empirically correlated. In GP16, which traversed the hydrothermal plume emanating from the Southern East Pacific Rise, ^{230}Th and ^{231}Pa inventory depletions from reversible scavenging within plume water depths were correlated with $^{3}He_{xs}$ inventories west of the

East Pacific Rise ridge site (Pavia et al., 2018). However, by including provinces that are unaffected by hydrothermal scavenging, a relationship between He and ^{230}Th or ^{231}Pa depletion is more difficult to gauge. For example, as a whole GP15 did not show a relationship between $^{230}Th_{xs}$ depletion from reversible scavenging and δ^3He in areas where $^{230}Th_{xs}$ depletions occur. This is potentially a result of the asymmetry and difference in relative depletion between the plumes. However, at stations 23, 25, and 33 – 37 the beginning of these mid-depth depletions (Fig. 3.8) occurred concurrent with some of the highest δ^3He values (Fig. 3.7), with depletions only occurring with a δ^3He above 27. The implications of this seems to be that high δ^3He is still a useful indicator to show where $^{230}Th_{xs}$ is depleted due to hydrothermal activity, although the degree of depletion is not necessarily linked. The overall message of this finding is that areas with high δ^3He or a similar hydrothermal indicator can represent areas of the ocean where ^{230}Th has been scavenged due to hydrothermal activity, which potentially creates uncertainty to ^{230}Th is being used as a constant-flux proxy.

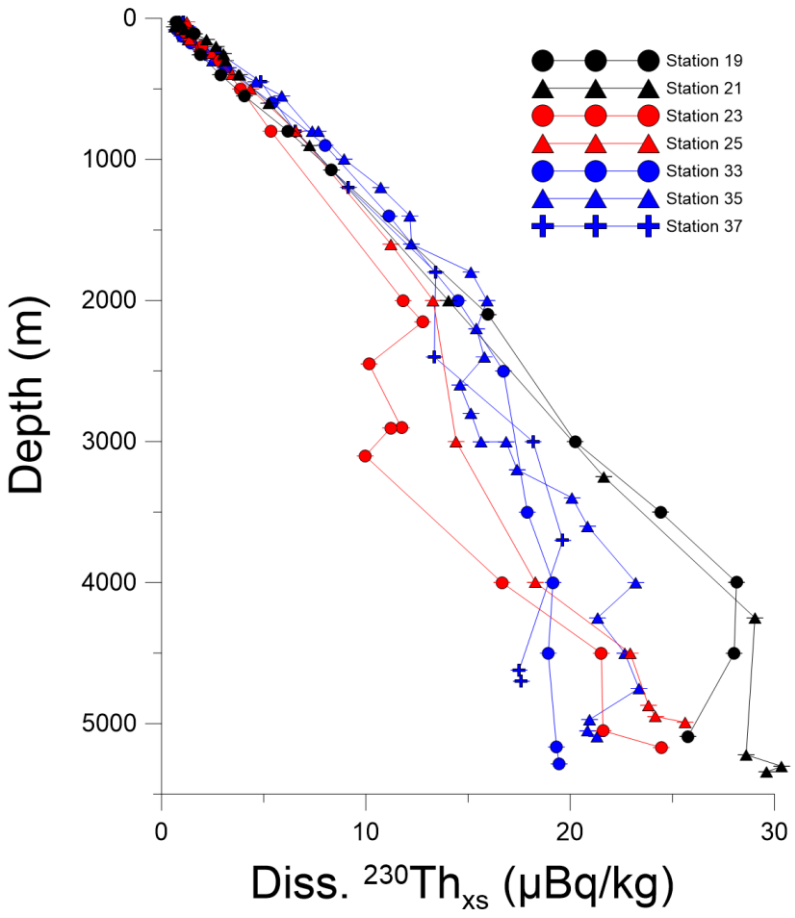

Figure 3.8 *GP15 stations where hydrothermal depletions of $^{230}Th_{xs}$ are present*

GP15 stations where hydrothermal depletions of $^{230}Th_{xs}$ are present. Stations 19 and 21 (black) are subtropical stations used to show reversible scavenging conditions to 4000 m. Stations 23 and 25 (red) are north of the equator and stations 33 – 37 are south of the equator and show the difference in depletion of $^{230}Th_{xs}$ due to hydrothermally-scavenged water starting at 2000 m.

3.5.3 Lack of ^{230}Th Scavenging off the Hawaiian Ridge

Hydrothermal plumes transport Fe and Mn oxyhydroxide particles, which can be particularly reactive in terms of metal scavenging. This hydrothermal Fe potentially a nutrient source to systems that are otherwise Fe-limited. The Loihi Seamount is one such place where it has been proposed that hydrothermal Fe may persist far enough away from its source to be upwelled and incorporated into productivity along the North American

coast (Jenkins et al., 2020). Measurements of δ^3He, dFe, and dMn at Loihi GP15 station 18.6 increase after 1000 m to a maximum at 1200 m before slightly decreasing to the bottom at 1300 m (Jenkins et al., 2020). This signal is seen in the surrounding GP15 stations, showing that hydrothermal Fe is propagated ~100 – 1000 km from its source (Jenkins et al., 2020). However, there is still some debate as to whether this hydrothermal Fe has a sufficient residence time to make it to the surface. While traditional estimates of deep water dFe replacement times (70 – 270 y, Bergquist & Boyle, 2006; Bruland, 1994) potentially support this hypothesis, recent estimates deriving from Th fluxes lowers this timescale to <20 years (Hayes et al., 2018; Hayes et al., 2015) which suggests this Fe would not reach the surface. Our observation of $^{230}Th_{xs}$ at Loihi and surrounding GP15 stations show that, although there is an increased presence of potentially reactive Fe and Mn below 1100 m, shelf demi-stations at Puna Ridge (18.3) and Loihi Seamount (18.6) have $^{230}Th_{xs}$ profiles that can be entirely explained by reversible scavenging (Fig. 3.9). Surrounding stations 18 and 19 also set by reversible scavenging above 4000 m. This is consistent with similar trends seen at sampling site ALOHA (Hayes, Fitzsimmons, et al., 2015). Distinctive from EPR scavenging, discussed below, hydrothermal activity from Hawaiian hotspot activity does not seem to have an effect on scavenging intensity of ^{230}Th either locally or distally.

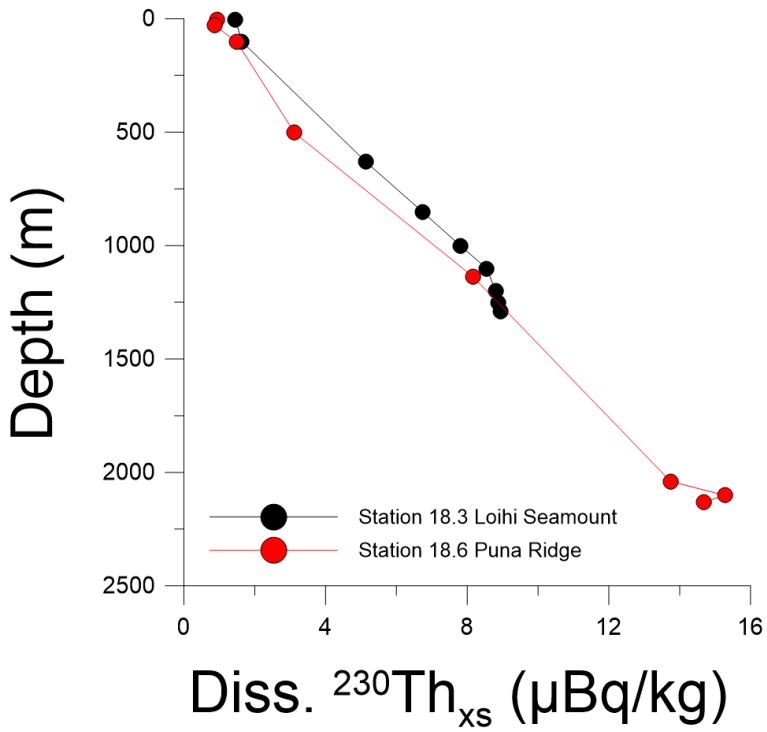

Figure 3.9 *The $^{230}Th_{xs}$ concentration vs depth profiles for Loihi Seamount and Puna Ridge*

The $^{230}Th_{xs}$ concentration (µBq/kg) vs depth profiles (m) for Loihi Seamount (black) and Puna Ridge (red). Both distributions can be explained by reversible scavenging and have an R^2 of .9948 and .9925 respectively.

3.5.4 Impact of the EPR on Boundary Scavenging at the Equatorial Particle Veil

The complex currents and upwelling of nutrients along the equator create and extremely dynamic zone of regeneration and primary productivity. We define the Equatorial Particle Veil as a comprised by the area of (1) between 1° N and S where particulate organic carbon flux is three times greater than off-equatorial regions and (2) its adjacent deep eastward jets ~2° N and S that act to focus small marine particles (Kiko et al., 2017). In the right conditions, scavenged ^{230}Th can be used as a reference to estimate the flux of other trace elements to the seafloor using a technique called ^{230}Th normalization (Francois et al., 2004; Henderson & Anderson, 2003). Because of ^{230}Th's

extreme insolubility, ^{230}Th accumulation in sediment should be equal to its production by radioactive decay in the overlying water column, allowing a relative flux calculation of other trace elements without considering changes to mass accumulation rate. This technique is potentially problematic where ^{230}Th is removed or added before burial (Siddall et al., 2008). It has been argued that high ^{230}Th fluxes found in the Equatorial Pacific are a result of "particle flux effects" where the relatively high scavenging near the Equatorial Particle Veil will quickly remove ^{230}Th from seawater, which in turn, encourages increased lateral mixing from surrounding subtropical gyres and additional ^{230}Th burial (Lyle et al., 2005; Thomas et al., 2000). This focusing effect changes the flux-to-production-ratio, lead to equatorial burial fluxes being underestimated from its actual value. The effect from flux-to-production-ratio and sediment transport changes has been modeled (Siddall et al., 2008), estimating that ^{230}Th is buried in the Equatorial Pacific 30% higher than its production. However, this debate has mostly focused on particle flux effect stemming almost entirely from the scavenging contrast between the Equatorial Particle Veil and the surrounding subtropical gyres. Hydrothermal depletions of ^{230}Th can also drive hydrothermal flux effects which potentially bury ^{230}Th in excess of its production, which we separate from the biogenic particle flux. Our goal is not to specially calculate specific differences between ^{230}Th transport and production, but to use GP15 in the context of historical data to look at hydrothermally influenced regions and constrain where hydrothermal particle flux effects might bury above or below production and cause uncertainty for ^{230}Th normalization. We believe that ^{230}Th normalization calculations warrant additional consideration at EPR scavenging sites and all locations "downstream" where circulation has mobilized depleted water further into the basin.

Figure 3.11 uses δ^3He and historical measurements to roughly constrain the locations where hydrothermal influence potentially impacts ^{230}Th burial relative to its decay production.

For GP15, our prediction of reversible scavenging, which is related to biogenic scavenging sources, functionally serves as a way to predict scavenging without hydrothermal and/or benthic scavenging features. We can evaluate ^{230}Th transport, and thereby its changes relative to production from decay, and where this transport is taking place spatially by looking at the relative changes in concentration along isopycnal surfaces between sampling stations. Our model of reversible scavenging predicts the biggest changes in ^{230}Th transport between 2000 – 4000 m to occur within 5° north and south of the Equator (Fig. 3.10, top). In our observed data, the area encompassing the hydrothermal-enriched equatorial currents have significantly lower ^{230}Th concentrations, similar to the concentrations found in the Equatorial Particle Veil. This difference in ^{230}Th concentration due to hydrothermal activity functionally erases the ^{230}Th gradient expected from biogenic particle scavenging and a new gradient exists at the boundary between hydrothermally influenced waters and the subtropical boundary ~20° S and 10° N (Fig. 3.10, bottom). It appears that at GP15, at least qualitatively, the relatively smaller change in ^{230}Th concentration over distances at the hydrothermal/subtropical boundary implies less ^{230}Th transport than what would be expected by particle effects at the equator. This begs the question whether hydrothermal boundary ^{230}Th transport is enough to affect ^{230}Th normalization calculations. For comparison, modeling of the equatorial particle flux effect has shown that ^{230}Th is potentially buried about 1.3 times greater than its production (Siddall et al., 2008). As relative depletion of ^{230}Th below 2000 m becomes

smaller west of GP15, we expect that ^{230}Th transport patterns to progressively resemble those set by biogenic particles. This means that some part of the plumes around the equator might bury ^{230}Th closer to production than what is expected from equatorial particle effects, but at some point, hydrothermal influence will be low enough that the flux-to-production-ratio is driven by equatorial biogenic particle scavenging.

However, looking east of GP15, the difference in relative ^{230}Th depletion in the hydrothermal plume is greater as you progress towards the East Pacific Rise. This means that the contrast in ^{230}Th concentration between the hydrothermal/subtropical boundary is greater closer to the EPR than found in GP15. In the middle of the southern plume, ^{230}Th depletions due to hydrothermal scavenging at the EPR have been shown to be as high as 80% between 2200 and 2800 (Pavia et al., 2018), with ^{230}Th concentrations lower than the expected ^{230}Th concentration at the equator due to reversible scavenging. Although depletions near the hydrothermal/subtropical boundary might not be as high as directly over the ridge site, the implication of this is that transport due to the relative concentration difference at the hydrothermal/subtropical boundary can be, in places, potentially greater than expected equatorial transport.

The Equatorial Particle Veil has a slightly different role in the boundary scavenging of ^{230}Th when considering hydrothermal activity in the East Pacific. As GP15 stations 27 – 31 and JGOFS are relatively close to reversible equilibrium, it seems that biogenic particle scavenging at the equator and its adjacent to hydrothermally depleted waters have some degree of geographic separation, likely due to circulation of the major equatorial currents. This separation implies that mixing between the equator and its surrounding hydrothermal waters occurs to some degree, but has relatively little impact

on equatorial/hydrothermal ^{230}Th transport. The Equatorial Particle Veil should then bury ^{230}Th close to production where it is surrounded by hydrothermal activity in the East Pacific.

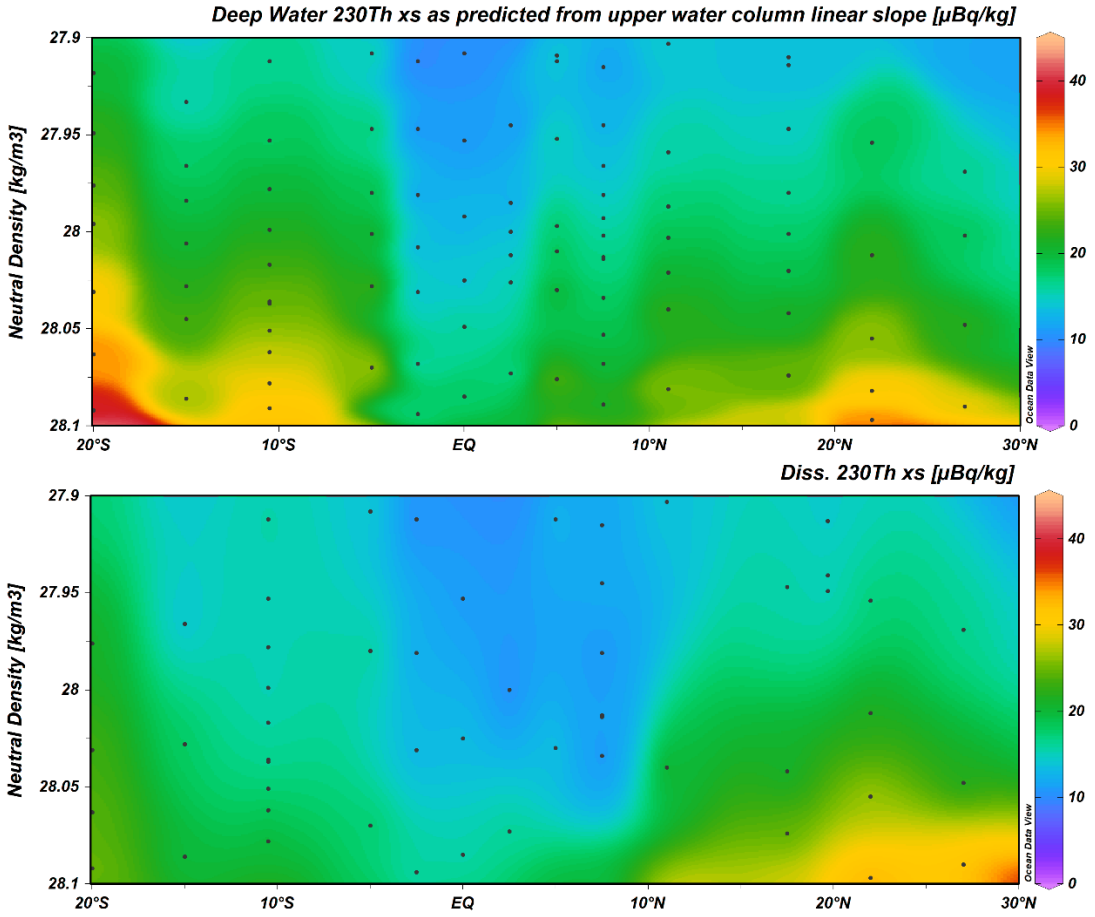

Figure 3.10 *Hydrothermal influence on equatorial boundary scavenging*

The difference between a one-dimensional reversible scavenging model and observed data show that the influence of hydrothermal plumes near the equator change the characteristics of the equatorial region as a boundary sink for ^{230}Th. The expected $^{230}Th_{xs}$ transport to the equator occurs along isopycnal surfaces and is relative to the concentration difference between stations. Neutral density shown represents the depths between 2000 – 4000 m. Top – $^{230}Th_{xs}$ concentration as predicted by reversible scavenging, showing expected transport of $^{230}Th_{xs}$ near the equator without hydrothermal influence. In our model, major changes in $^{230}Th_{xs}$ concentration are constrained within 5° of the Equator and are of a magnitude of ~5 – 10 µBq/kg over <250 km. Bottom – Observed $^{230}Th_{xs}$. Gradients in $^{230}Th_{xs}$ concentration are smoothed out in regions subject to hydrothermal influence. Major changes in 230Thxs concentration occur over a much wider area, 10° from the Equator or greater, and the relative difference in concentration is only ~2 – 5 µBq/kg at these transitions.

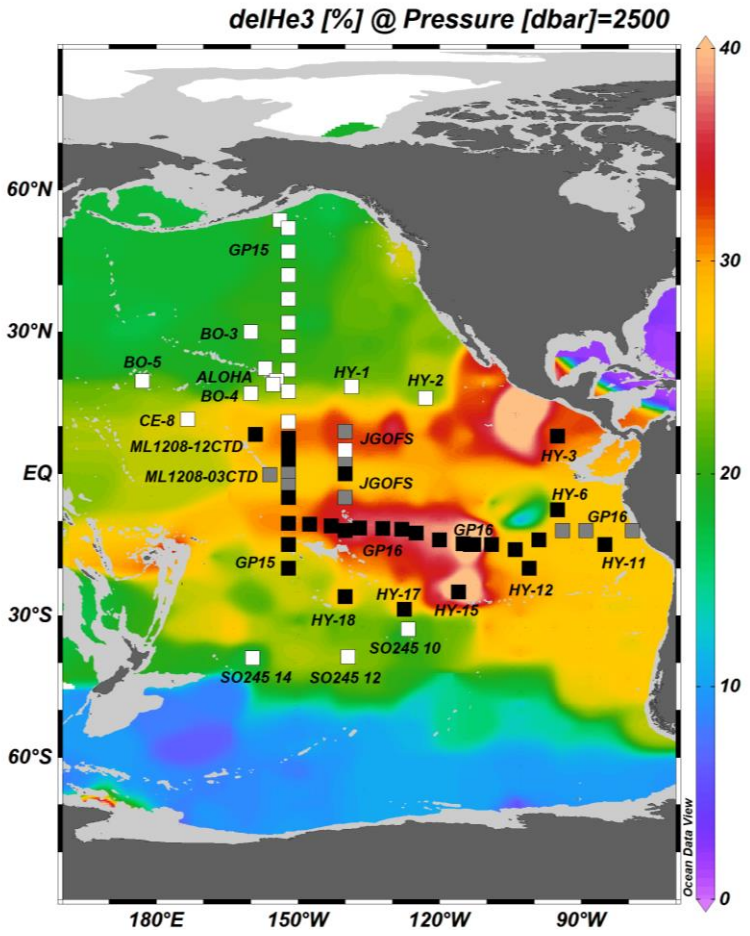

Figure 3.11 *Historical profiles for constraining hydrothermal scavenging of ^{230}Th and ^{231}Pa in the Pacific*

A map of stations from GP15 and historical studies of water column dissolved ^{230}Th constraining the spatial extend of potential hydrothermal scavenging in the middle eastern Pacific. Additional consideration for ^{230}Th normalization should be taken at or adjacent to EPR ridge sites, along the equator, and downstream of major circulation pathways from these areas. This area is shown, roughly outlined by higher δ^3He, and uses historical data to show areas where ^{230}Th depletions occur due to hydrothermal activity, giving some spatial constraint to where hydrothermal boundaries may be impactful. White squares show profiles where reversible scavenging explains at least the upper 3000 m of ^{230}Th concentration in the water column. These stations may deviate from reversible scavenging below this depth, however it is not possible in these cases to differentiate these depletions from other benthic effects. Gray squares indicate where conditions are close to reversible scavenging, but show some hydrothermal depletion. These stations have depletions that are relatively lower or quickly return to a pseudo-equilibrium distribution. Black squares indicate significant hydrothermal depletion where deviations from reversible scavenging occurs in waters shallower than 3000 m. Cruise sites included in this compilation are taken from this study, GP16 (Pavia et al., 2018), ML1208 (Lopez et al., 2015), SO245 (Pavia et al., 2020), ALOHA (Hayes et al., 2015), KH-82-1 (Nozaki & Nakanishi, 1985), Hydra (Okubo, 2018; Okubo et al., 2012), and Boötes Expedition (Okubo et al., 2012).

3.5.5 Transport of ^{230}Th between the Subarctic and Subtropical Gyres

One area where biogenic scavenging processes potentially act as a scavenging boundary is between the productive subarctic gyre and the oligotrophic subtropical gyre. However, it is somewhat difficult to constrain ^{230}Th transport across this feature, partially due to lack of understanding in the dynamics and convergence of this particular boundary in how it affects ^{230}Th scavenging. The Transition Zone Chlorophyll Front is a dynamic, seasonally variable productivity feature at the convergence between the subarctic/subtropical gyres (Polovina et al., 2001) where strong winds in the fall and winter drive accumulation of nutrients in the North Pacific subtropical gyre (Ayers & Lozier, 2010). At GP15, this feature varies seasonally from about 30° N in winter to 40° N in summer, changing surface chlorophyll content from <1 to ~0.2 mg/m^3 (Polovina et al., 2001). At GP15, we observe that $^{230}Th_{xs}$ concentrations across this boundary; (1) Can be explained by biogenic scavenging in the upper 3000 m (Fig. 3.4 and 3.5), (2) has little change in $^{230}Th_{xs}$ inventories within either gyre near this boundary, and (3) The transition between the low $^{230}Th_{xs}$ inventory of the subarctic gyre and high inventory subtropical gyre is located between stations 12 and 14, with no intermediate transition observed (Fig. 3.12). The implication of these is that the zone of where biogenic scavenging contrast can cause ^{230}Th transport is relatively very narrow, less than 500 km, and is located near the annually averaged Transition Zone Chlorophyll Front. SPM inventories, which at depth can have a residence time on the month scale, also seems to evidence this narrow scavenging front (Fig. 3.3). Transport of ^{230}Th via diffusive mixing can sometimes be calculated from discrete data where 3 or more profiles follow a progressive transition, such as what was done off the Mauritania continental margin (Hayes et al., 2015).

However, the spatial resolution of GP15 did not capture an adequate transition between the gyres to calculate transport. In the future, this data may be useful in constraining circulation models, where the spatial resolution is small enough to capture the ^{230}Th gradient, in order to create a better estimate of ^{230}Th transport between the subarctic and subtropical gyres.

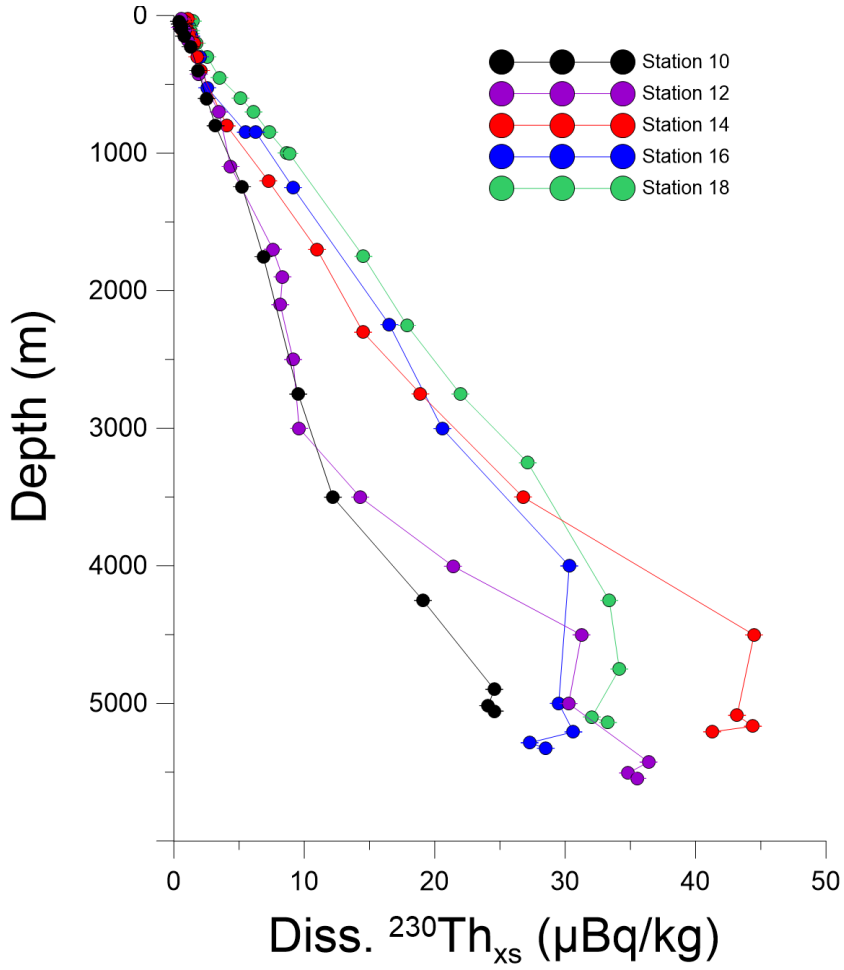

Figure 3.12 *$^{230}Th_{xs}$ concentration profiles at GP15 stations 10 – 18*

$^{230}Th_{xs}$ concentration profiles at GP15 stations 10 – 18 consisting of the stations that surround the transition between the North Pacific subarctic and subtropical gyres. Stations in each region show similar $^{230}Th_{xs}$ profiles with the largest change in concentrations, and thereby ^{230}Th transport, constrained between stations 12 and 14. However, our observed data failed to capture adequate transition between these features such that diffusive transport could be directly calculated.

3.5.6 Benthic Influences on $^{230}Th_{xs}$ Distribution

Multiple anomalies of $^{230}Th_{xs}$ are evident in the deep water north of 10° N and may be evidence of differing ventilation rates of Lower Circumpolar Deep Water throughout this region (Fig. 3.13). Circulation in the Pacific Ocean can be described by three component layers: the surface/intermediate layer, the upper deep layer, and the lower deep layer (Kawabe & Fujio, 2010). Throughout the North Pacific, these layers correspond to the depth ranges of <2000 m, 2000 – 3500 m, and >3500 m respectively (Kawabe et al., 2003). At GP15 between 10° N – 50° N, $^{230}Th_{xs}$ concentrations in the surface/intermediate and upper deep water layers are consistent with reversible scavenging whereas $^{230}Th_{xs}$ concentration are anomalous in the lower deep water layer (Fig. 3.4, top). The lower deep layer is comprised of Lower Circumpolar Deep Water (LCDW) (Lawrence et al., 2022) which travels northward in the western Pacific, taking various paths before eventually upwelling east of GP15. The lower deep layer we see at GP15 is comprised of several of these pathways (Kawabe & Fujio, 2010). North of 50° N Lower Circumpolar Deep Water convergences from both the major eastern and western branch pathways and travels along the Japan / Aleutian trenches (~6 Sv). The other two pathways are primarily derived from just the eastern branch (Kawabe & Fujio, 2010). The eastern branch diverges at ~10° N and loops around the Hawaiian Islands before traveling westward again (<1 Sv). At ~30° N, 170 E°, the eastern branch again diverges with most entering the convergence between the east and west branches and a small amount heading east through the gap in the Emperor Seamounts Chain and connecting with the remains of the Hawaiian branch (1 Sv).

The area of low $^{230}Th_{xs}$ anomaly is centered where the Hawaiian loop branch crosses GP15. This deep depletion may be evidence of persistent bottom sediment resuspension caused by the relatively more vigorous circulation in this section compared with surrounding regions. The area west of the Hawaiian Islands is relatively sparse of deep attenuation data (Gardner et al., 2018), making the identification of these nepheloid layer difficult. However, the circulation pathway leading to tropical GP15 is about 4 Sv (Kawabe & Fujio, 2010) and is potentially vigorous enough to stimulate benthic sediment resuspension. There is some evidence for increased particle load in the bottom waters of GP15 stations in the region as small particle SPM shows increased bottom concentration, however, these increases are confined to below 5000 m, meaning nepheloid layers at GP15 might not explain the anomaly in its entirety. Instead, we suspect that these nepheloid layers might be more prominent westward and to some degree, the depletion of ^{230}Th at GP15 is advected from these stronger sinks.

Opposite this, the high bottom $^{230}Th_{xs}$ anomaly is potentially evidence of slower deep water ventilation where bottom sediments can dissolve and "leak" excess ^{230}Th to bottom water. Modeling by Hautala et al. (2018) shows that deep water south of the Aleutian Islands surrounding 40° N is potentially subject to cyclonic recirculation and vastly slower upwelling. The impacts of this longer exposure might lead to dissolution of some bottom sediment, causing an excess of ^{230}Th and other scavenged trace metals such as Co and Mn (Chmiel et al., 2022), or Nd, Cu, and Ba (Shiller, 2021) to accumulate in the bottom water.

Due to the complicated topography of the region where we see benthic $^{230}Th_{xs}$ anomalies, it is difficult to assess whether the difference in scavenging potential between

these benthic features could constitute a boundary in terms of facilitating ^{230}Th transport. On one hand, there is a relative difference in ^{230}Th concentration between the anomalies and given the increased ^{230}Th inventory with depth could potentially drive a large amount of ^{230}Th transport. On the other hand, the existence of these $^{230}Th_{xs}$ anomalies implies that there is a degree of topographic separation between this water and if transport occurs, might not fit the simplified model of an ocean boundary.

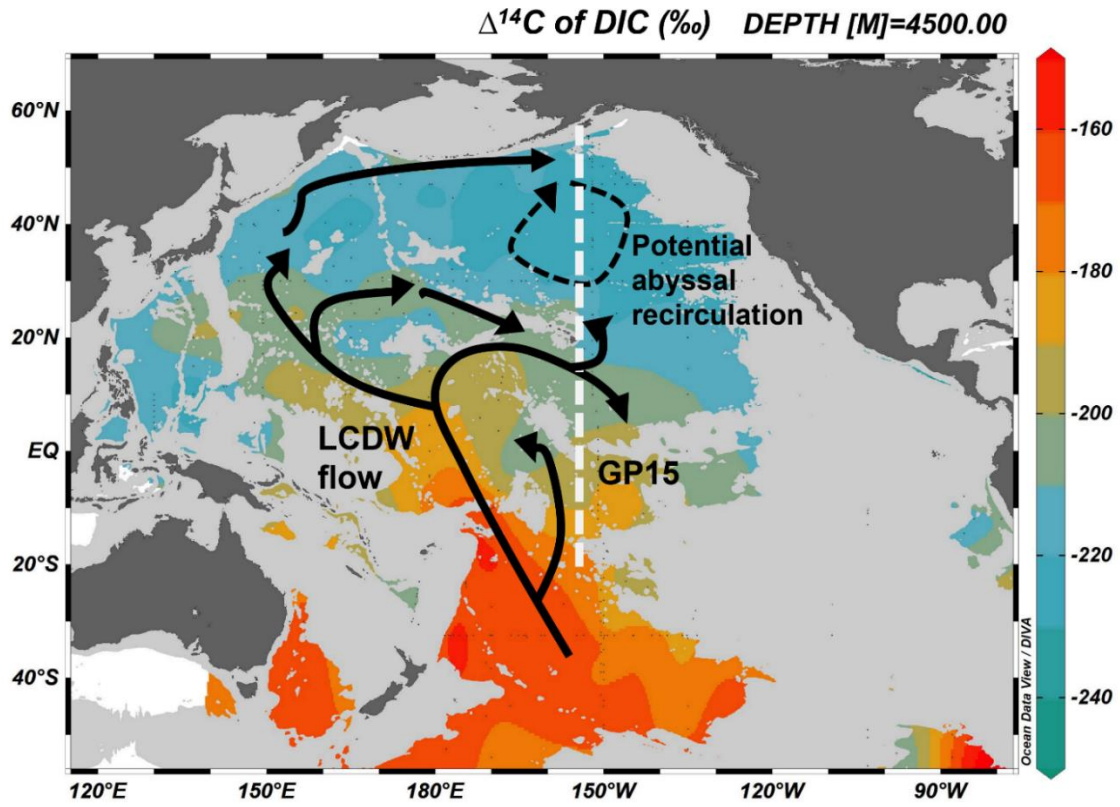

Figure 3.13 *Pathways of Lower Circumpolar Deep Water that potentially cause local scavenging anomalies in the bottom waters of GP15.*

Pathways of Lower Circumpolar Deep Water that potentially cause local scavenging anomalies in the bottom waters of GP15. LCDW circulation based on Kawabe & Fujio (2010), Abyssal recirculation based on Hautala (2018), and radiocarbon data from Lauvset et al. (2022).

3.6 Conclusion

The distribution of ^{230}Th and ^{231}Pa at GP15 show that biogenic, hydrothermal, and benthic processes all play a role in creating boundaries for scavenging in the Pacific. As a whole, the upper water column is set by biogenic particle flux, which was used to derive areas where other scavenging processes occurred. Near the equator, we observed two altered water masses where long-lived depleted ^{230}Th signatures were advected from hydrothermal activity at the EPR. This hydrothermally influenced water erased the expect biogenic scavenging boundary at the Equatorial Particle Veil, however new boundaries for potential transport of ^{230}Th were found at the transition between hydrothermal waters and the subtropical gyres. This potentially expands the area of uncertainty for flux estimates using ^{230}Th to include the extent of these hydrothermal depletions, however to what degree is difficult to constrain and likely variable with proximity to *in-situ* scavenging at the EPR. Other boundaries, such as the subarctic/subtropical gyre boundary, potentially affect flux calculations as well. This boundary has dramatic differences in biogenic particle flux which vary as much as 10° latitude seasonally. However, the distribution of $^{230}Th_{xs}$, which represents a longer time scale, was relatively insensitive to these changes. The transition between these low and high particle flux zones that is potentially sensitive to these changes is constrained to within 500 km near the midpoint of the seasonal extent. Lastly, $^{230}Th_{xs}$ anomalies in the deep water of the North Pacific show evidence for both a section of strong bottom ventilation that induced ^{230}Th scavenging from nepheloid layers and a section of sluggish recirculation that enriches ^{230}Th through the dissolution of bottom sediments.

3.7 Data Statement

Finalized data will be archived with the Biological and Chemical Oceanography Data Management Office (https://www.bco-dmo.org/project/695926).

3.8 Works Cited

Andersen, M. B., Stirling, C. H., Zimmermann, B., & Halliday, A. N. (2010). Precise determination of the open ocean 234U/238U composition. *Geochemistry, Geophysics, Geosystems*, *11*(12). https://doi.org/10.1029/2010GC003318

Anderson, R. F., Bacon, M. P., & Brewer, P. G. (1983). Removal of 230Th and 231Pa from the open ocean. *Earth and Planetary Science Letters*, *62*(1), 7–23.

Anderson, R. F., Cheng, H., Edwards, R. L., Fleisher, M. Q., Hayes, C. T., Huang, K. F., Kadko, D., Lam, P. J., Landing, W. M., Lao, Y., Lu, Y., Measures, C. I., Moran, S. B., Morton, P. L., Ohnemus, D. C., Robinson, L. F., & Shelley, R. U. (2016). How well can we quantify dust deposition to the ocean? *Philosophical Transactions of the Royal Society A: Mathematical, Physical and Engineering Sciences*, *374*(2081). https://doi.org/10.1098/rsta.2015.0285

Anderson, R. F., Fleisher, M. Q., Robinson, L. F., Edwards, R. L., Hoff, J. A., Moran, S. B., van der Loeff, M. R., Thomas, A. L., Roy-Barman, M., & Francois, R. (2012). GEOTRACES intercalibration of 230th, 232Th, 231Pa, and prospects: For10be. *Limnology and Oceanography: Methods*, *10*(APRIL), 179–213. https://doi.org/10.4319/lom.2012.10.179

Anderson, R. F., Lao, Y., Broecker, W. S., Trumbore, S. E., Hofmann, H. J., & Wolfli, W. (1990). Boundary scavenging in the Pacific Ocean: a comparison of 10Be and 231Pa. *Earth and Planetary Science Letters*, *96*(3–4), 287–304.

Auro, M. E., Robinson, L. F., Burke, A., Bradtmiller, L. I., Fleisher, M. Q., & Anderson, R. F. (2012). Improvements to 232-thorium, 230-thorium, and 231-protactinium analysis in seawater arising from GEOTRACES intercalibration. *Limnology and Oceanography: Methods*, *10*(JULY), 464–474. https://doi.org/10.4319/lom.2012.10.464

Ayers, J. M., & Lozier, M. S. (2010). Physical controls on the seasonal migration of the North Pacific transition zone chlorophyll front. *Journal of Geophysical Research: Oceans*, *115*(5). https://doi.org/10.1029/2009JC005596

Bacon, M. P. (1984). Glacial to interglacial changes in carbonate and clay sedimentation in the Atlantic Ocean estimated from 230Th measurements. *Isotope Geoscience*, *2*, 97–111.

Bacon, M. P., & Anderson, R. F. (1982). Distribution of Thorium Isotopes Between Dissolved and Particulate Forms in The Deep Sea. *Journal of Geophysical Research*, *87*(1), 2045–2056. https://doi.org/10.1029/JC087iC03p02045

Bacon, M. P., Spencer, D. W., & Brewer, P. G. (1976). 210Pb/226Ra and 210Po/210Pb disequilibria in seawater and suspended particulate matter. *Earth and Planetary Science Letters*, *32*, 277–296.

Bennett, S. A., Achterberg, E. P., Connelly, D. P., Statham, P. J., Fones, G. R., & German, C. R. (2008). The distribution and stabilisation of dissolved Fe in deep-sea hydrothermal plumes. *Earth and Planetary Science Letters*, *270*(3–4), 157–167. https://doi.org/10.1016/j.epsl.2008.01.048

Bergquist, B. A., & Boyle, E. A. (2006). Dissolved iron in the tropical and subtropical

Atlantic Ocean. *Global Biogeochemical Cycles*, *20*(1). https://doi.org/10.1029/2005GB002505

Biscaye, P. E., & Eittreim, S. L. (1977). SUSPENDED PARTICULATE LOADS AND TRANSPORTS IN THE NEPHELOID LAYER OF THE ABYSSAL ATLANTIC OCEAN*. In *Marine Geology* (Vol. 23).

Bown, J., Boye, M., Baker, A., Duvieilbourg, E., Lacan, F., le Moigne, F., Planchon, F., Speich, S., & Nelson, D. M. (2011). The biogeochemical cycle of dissolved cobalt in the Atlantic and the Southern Ocean south off the coast of South Africa. *Marine Chemistry*, *126*(1–4), 193–206. https://doi.org/10.1016/j.marchem.2011.03.008

Bruland, K. (1994). Reactive trace metals in the stratified central North Pacific. In *Geochimica et Cosmochimica Acta* (Vol. 58, Issue 15).

Bruland, K. W., Middag, R., & Lohan, M. C. (2014). *Controls of Trace Metals in Seawater*. http://www.agu.org/eos_elec/97025e.html

Chase, Z., Anderson, R. F., Fleisher, M. Q., & Kubik, P. W. (2002). The influence of particle composition and particle flux on scavenging of Th, Pa and Be in the ocean. *Earth and Planetary Sciences Letters*, *204*, 215–229.

Cheng, H., Lawrence Edwards, R., Shen, C. C., Polyak, V. J., Asmerom, Y., Woodhead, J., Hellstrom, J., Wang, Y., Kong, X., Spötl, C., Wang, X., & Calvin Alexander, E. (2013). Improvements in 230Th dating, 230Th and 234U half-life values, and U-Th isotopic measurements by multi-collector inductively coupled plasma mass spectrometry. *Earth and Planetary Science Letters*, *371–372*, 82–91. https://doi.org/10.1016/j.epsl.2013.04.006

Chmiel, R., Lanning, N., Laubach, A., Lee, J. M., Fitzsimmons, J., Hatta, M., Jenkins, W., Lam, P., McIlvin, M., Tagliabue, A., & Saito, M. (2022). Major processes of the dissolved cobalt cycle in the North and equatorial Pacific Ocean. *Biogeosciences*, *19*(9), 2365–2395. https://doi.org/10.5194/bg-19-2365-2022

Costa, K. M., Hayes, C. T., Anderson, R. F., Pavia, F. J., Bausch, A., Deng, F., Dutay, J. C., Geibert, W., Heinze, C., Henderson, G., Hillaire-Marcel, C., Hoffmann, S., Jaccard, S. L., Jacobel, A. W., Kienast, S. S., Kipp, L., Lerner, P., Lippold, J., Lund, D., … Zhou, Y. (2020). 230Th Normalization: New Insights on an Essential Tool for Quantifying Sedimentary Fluxes in the Modern and Quaternary Ocean. *Paleoceanography and Paleoclimatology*, *35*(2), 1–36. https://doi.org/10.1029/2019PA003820

Delanghe, D., Bard, E., & Hamelin, B. (2002). New TIMS constraints on the uranium-238and uranium-234 in seawaters from the main ocean basins and the Mediterranean Sea. *Marine Chemistry*, *80*, 79–93.

Deng, F., Thomas, A. L., Rijkenberg, M. J. A., & Henderson, G. M. (2014). Controls on seawater 231Pa, 230Th and 232Th concentrations along the flow paths of deep waters in the Southwest Atlantic. *Earth and Planetary Science Letters*, *390*, 93–102.

Fitzsimmons, J. N., Boyle, E. A., & Jenkins, W. J. (2014). Distal transport of dissolved hydrothermal iron in the deep South Pacific Ocean. *Proceedings of the National Academy of Sciences of the United States of America*, *111*(47), 16654–16661. https://doi.org/10.1073/pnas.1418778111

Francois, R., Bacon, M. P., Altabet, M. A., & Labeyrie, L. D. (1993). Glacial/interglacial

changes in sediment rain rate in the SW Indian Sector of subantarctic Waters as recorded by 230Th, 231Pa, U, and δ15N. *Paleoceanography*, *8*(5), 611–629.

Francois, R., Frank, M., Rutgers van der Loeff, M., & Bacon, M. P. (2004). 230Th normalization: An essential tool for interpreting sedimentary fluxes during the late Quaternary. *Paleoceangraphy*, *19*.

Gardner, W. D., Richardson, M. J., Mishonov, A. V., & Biscaye, P. E. (2018). Global comparison of benthic nepheloid layers based on 52 years of nephelometer and transmissometer measurements. *Progress in Oceanography*, *168*, 100–111. https://doi.org/10.1016/j.pocean.2018.09.008

Goldberg, E. D. (1954). Marine Geochemistry 1. Chemical Scavengers of the Sea. *The Journal of Geology*, *62*(3), 249–265.

Gueguen, C., & Guo, L. D. (2002). Thorium and protactinium sorption on silica. *Geochimica and Cosmochimica Acta*, *66*, A295.

Hautala, S. L. (2018). The abyssal and deep circulation of the Northeast Pacific Basin. *Progress in Oceanography*, *160*, 68–82. https://doi.org/10.1016/j.pocean.2017.11.011

Hayes, C. T., Anderson, R. F., Cheng, H., Conway, T. M., Edwards, R. L., Fleisher, M. Q., Ho, P., Huang, K. F., John, S. G., Landing, W. M., Little, S. H., Lu, Y., Morton, P. L., Moran, S. B., Robinson, L. F., Shelley, R. U., Shiller, A. M., & Zheng, X. Y. (2018). Replacement Times of a Spectrum of Elements in the North Atlantic Based on Thorium Supply. *Global Biogeochemical Cycles*, *32*(9), 1294–1311. https://doi.org/10.1029/2017GB005839

Hayes, C. T., Anderson, R. F., Fleisher, M. Q., Huang, K. F., Robinson, L. F., Lu, Y.,

Cheng, H., Edwards, R. L., & Moran, S. B. (2015). 230Th and 231Pa on GEOTRACES GA03, the U.S. GEOTRACES North Atlantic transect, and implications for modern and paleoceanographic chemical fluxes. *Deep-Sea Research Part II: Topical Studies in Oceanography*, *116*, 29–41. https://doi.org/10.1016/j.dsr2.2014.07.007

Hayes, C. T., Anderson, R. F., Fleisher, M. Q., Serno, S., Winckler, G., & Gersonde, R. (2013). Quantifying lithogenic inputs to the North Pacific Ocean using the long-lived thorium isotopes. *Earth and Planetary Science Letters*, *383*, 16–25.

Hayes, C. T., Anderson, R. F., Fleisher, M. Q., Vivancos, S. M., Lam, P. J., Ohnemus, D. C., Huang, K. F., Robinson, L. F., Lu, Y., Cheng, H., Edwards, R. L., & Moran, S. B. (2015). Intensity of Th and Pa scavenging partitioned by particle chemistry in the North Atlantic Ocean. *Marine Chemistry*, *170*, 49–60. https://doi.org/10.1016/j.marchem.2015.01.006

Hayes, C. T., Anderson, R. F., Jaccard, S. L., François, R., Fleisher, M. Q., Soon, M., & Gersonde, R. (2013). A new perspective on boundary scavenging in the North Pacific Ocean. *Earth and Planetary Science Letters*, *369–370*, 86–97. https://doi.org/10.1016/j.epsl.2013.03.008

Hayes, C. T., Fitzsimmons, J. N., Boyle, E. A., McGee, D., Anderson, R. F., Weisend, R., & Morton, P. L. (2015). Thorium isotopes tracing the iron cycle at the Hawaii Ocean Time-series Station ALOHA. *Geochimica et Cosmochimica Acta*, *169*, 1–16. https://doi.org/10.1016/j.gca.2015.07.019

Henderson, G. M., & Anderson, R. F. (2003). The U-series toolbox for

paleoceanography. *Uranium-Series Geochemistry*, *52*, 493–531. https://doi.org/10.2113/0520493

Hsieh, Y. Te, Henderson, G. M., & Thomas, A. L. (2011). Combining seawater 232Th and 230Th concentrations to determine dust fluxes to the surface ocean. *Earth and Planetary Science Letters*, *312*(3–4), 280–290. https://doi.org/10.1016/j.epsl.2011.10.022

Hydes, D. J. (1983). Distribution of aluminium in waters of the North East Atlantic 25°N to 35°N. *Geochimica et Cosmochimica Acta*, *47*(5), 967–973.

Jenkins, W. J., Doney, S. C., Fendrock, M., Fine, R., Gamo, T., Jean-Baptiste, P., Key, R., Klein, B., Lupton, J. E., Newton, R., Rhein, M., Roether, W., Sano, Y., Schlitzer, R., Schlosser, P., & Swift, J. (2019). A comprehensive global oceanic dataset of helium isotope and tritium measurements. *Earth System Science Data*, *11*(2), 441–454. https://doi.org/10.5194/essd-11-441-2019

Jenkins, W. J., Hatta, M., Fitzsimmons, J. N., Schlitzer, R., Lanning, N. T., Shiller, A., Buckley, N. R., German, C. R., Lott, D. E., Weiss, G., Whitmore, L., Casciotti, K., Lam, P. J., Cutter, G. A., & Cahill, K. L. (2020). An intermediate-depth source of hydrothermal 3He and dissolved iron in the North Pacific. *Earth and Planetary Science Letters*, *539*, 116223. https://doi.org/10.1016/j.epsl.2020.116223

Jenkins, W. J., Lott III, D. E., & Cahill, K. L. (2019). A determination of atmospheric helium, neon, argon, krypton, and xenon solubility concentrations in water and seawater. *Marine Chemistry*, *211*, 94–107.

Kawabe, M., & Fujio, S. (2010). Pacific Ocean Circulation Based on Observation.

Journal of Oceanography, *66*, 389–403.

Kawabe, M., Fujio, S., & Yanagimoto, D. (2003). Deep-water circulation at low latitudes in the western North Pacific. *Deep-Sea Research Part I: Oceanographic Research Papers*, *50*(5), 631–656. https://doi.org/10.1016/S0967-0637(03)00040-2

Kiko, R., Biastoch, A., Brandt, P., Cravatte, S., Hauss, H., Hummels, R., Kriest, I., Marin, F., McDonnell, A. M. P., Oschlies, A., Picheral, M., Schwarzkopf, F. U., Thurnherr, A. M., & Stemmann, L. (2017). Biological and physical influences on marine snowfall at the equator. *Nature Geoscience*, *10*(11), 852–858. https://doi.org/10.1038/NGEO3042

Lam, P. J., Lee, J.-M., Heller, M. I., Mehic, S., Xiang, Y., & Bates, N. R. (2018). Size-fractionated distributions of suspended particle concentration and major phase composition from the U.S. GEOTRACES Eastern Pacific Zonal Transect (GP16). *Marine Chemistry*, *201*, 90–107.

Lauvset, S. K., Lange, N., Tanhua, T., Bittig, H. C., Olsen, A., Kozyr, A., Alin, S., Álvarez, M., Azetsu-Scott, K., Barbero, L., Becker, S., Brown, P. J., Carter, B. R., da Cunha, L. C., Feely, R. A., Hoppema, M., Humphreys, M. P., Ishii, M., Jeansson, E., … Key, R. M. (2022). GLODAPv2.2022: the latest version of the global interior ocean biogeochemical data product. *Earth System Science Data*, *14*(12), 5543–5572. https://doi.org/10.5194/essd-14-5543-2022

Lawrence, R. M., Shikumar, A., Roy, E. le, Swift, J., Lam, P. J., Cutter, G., & Casciotti, K. L. (2022). Water mass analysis of the 2018 US GEOTRACES 2 Pacific Meridional Transect (GP15). *ESS Open Archive*.

Lippold, J., Gherardi, J. M., & Luo, Y. (2011). Testing the 231Pa/230Th paleocirculation

proxy: A data versus 2D model comparison. *Geophysical Research Letters*, *38*(20). https://doi.org/10.1029/2011GL049282

Longhurst, A. (1995). Seasonal cycles of pelagic production and consumption. *Prog. Oceanogr.*, *36*(2), 77– 167.

Lopez, G. I., Marcantonio, F., Lyle, M., & Lynch-Stieglitz, J. (2015). Dissolved and particulate 230Th-232Th in the Central Equatorial Pacific Ocean: Evidence for far-field transport of the East Pacific Rise hydrothermal plume. *Earth and Planetary Science Letters*, *431*, 87–95. https://doi.org/10.1016/j.epsl.2015.09.019

Lupton, J. (1998). Hydrothermal helium plumes in the Pacific OCean. *Journal of Geophysical Research: Oceans*, *103*(C8), 15853–15868.

Lyle, M., Mitchell, N., Pisias, N., Mix, A., Martinez, J. I., & Paytan, A. (2005). Do geochemical estimates of sediment focusing pass the sediment test in the equatorial Pacific? *Paleoceanography*, *20*(1), 1–12. https://doi.org/10.1029/2004PA001019

Nozaki, Y., & Nakanishi, T. (1985). *231pa and 23°Th profiles in the open ocean water column* (Vol. 32, Issue 10).

Okubo, A. (2018). 230Th in the eastern South Pacific Ocean: Boundary scavenging and bottom scavenging by metal oxides derived from hydrothermal vents. *Deep-Sea Research Part I: Oceanographic Research Papers*, *139*, 79–87. https://doi.org/10.1016/j.dsr.2018.07.010

Okubo, A., Obata, H., Gamo, T., & Yamada, M. (2012a). 230Th and 232Th distributions

in mid-latitudes of the North Pacific Ocean: Effect of bottom scavenging. *Earth and Planetary Science Letters*, *339–340*, 139–150. https://doi.org/10.1016/j.epsl.2012.05.012

Okubo, A., Obata, H., Gamo, T., & Yamada, M. (2012b). 230Th and 232Th distributions in mid-latitudes of the North Pacific Ocean: Effect of bottom scavenging. *Earth and Planetary Science Letters*, *339–340*, 139–150. https://doi.org/10.1016/j.epsl.2012.05.012

Pavia, F. J., Anderson, R., Vivancos, S., Fleisher, M., Lam, P., Lu, Y., Cheng, H., Zhang, P., & Lawrence Edwards, R. (2018). Intense hydrothermal scavenging of 230Th and 231Pa in the deep Southeast Pacific. *Marine Chemistry*, *201*(April 2017), 212–228. https://doi.org/10.1016/j.marchem.2017.08.003

Pavia, F. J., Anderson, R. F., Black, E. E., Kipp, L. E., Vivancos, S. M., Fleisher, M. Q., Charette, M. A., Sanial, V., Moore, W. S., Hult, M., Lu, Y., Cheng, H., Zhang, P., & Edwards, R. L. (2019). Timescales of hydrothermal scavenging in the South Pacific Ocean from 234Th, 230Th, and 228Th. *Earth and Planetary Science Letters*, *506*, 146–156. https://doi.org/10.1016/j.epsl.2018.10.038

Pavia, F. J., Anderson, R. F., Pinedo-Gonzalez, P., Fleisher, M. Q., Brzezinski, M. A., & Robinson, R. S. (2020). Isopycnal Transport and Scavenging of 230Th and 231Pa in the Pacific Southern Ocean. *Global Biogeochemical Cycles*, *34*(12).

Pavia, F. J., Anderson, R. F., Winckler, G., & Fleisher, M. Q. (2020). Atmospheric Dust Inputs, Iron Cycling, and Biogeochemical Connections in the South Pacific Ocean From Thorium Isotopes. *Global Biogeochemical Cycles*, *34*(9). https://doi.org/10.1029/2020GB006562

Polovina, J. J., Howell, E., Kobayashi, D. R., & Seki, M. P. (2001). The transition zone chlorophyll front, a dynamic global feature defining migration and forage habitat for marine resources. In *Progress in Oceanography* (Vol. 49). www.elsevier.com/locate/pocean

Richon, C., & Tagliabue, A. (2019). Insights Into the Major Processes Driving the Global Distribution of Copper in the Ocean From a Global Model. *Global Biogeochemical Cycles*, *33*(12), 1594–1610. https://doi.org/10.1029/2019GB006280

Robert, J., Miranda, C. F., & Muxart, R. (1969). Mesure de la periode du protactinium-231 par microcalorimetrie. *Radiochimica Acta*, *11*, 104–108.

Robinson, L. F., Belshaw, N. S., & Henderson, G. M. (2004). U and Th concentrations and isotope ratios in modern carbonates and waters from the Bahamas. *Geochimica et Cosmochimica Acta*, *68*(8), 1777–1789. https://doi.org/10.1016/j.gca.2003.10.005

Roy-Barman, M. (2009). Modelling the effect of boundary scavenging on Thorium and Protactinium profiles in the ocean. In *Biogeosciences* (Vol. 6). www.biogeosciences.net/6/3091/2009/

Saito, M. A., Noble, A. E., Tagliabue, A., Goepfert, T. J., Lamborg, C. H., & Jenkins, W. J. (2013). Slow-spreading submarine ridges in the South Atlantic as a significant oceanic iron source. *Nature Geoscience*, *6*(9), 775–779. https://doi.org/10.1038/ngeo1893

Shiller, A. (2021). *Dissolved concentrations of Ba, Cd, Cu, Ga, Mn, Nd, Ni, and Pb from*

Leg 1 (Seattle, WA to Hilo, HI) of the US GEOTRACES Pacific Meridional Transect (PMT) cruise (GP15, RR1814) on R/V Roger Revelle from September to October 2018.

Siddall, M., Anderson, R. F., Winckler, G., Henderson, G. M., Bradtmiller, L. I., McGee, D., Franzese, A., Stocker, T. F., & Müller, S. A. (2008). Modeling the particle flux effect on distribution of 230th in the equatorial pacific. *Paleoceanography*, *23*(2), 1–17. https://doi.org/10.1029/2007PA001556

Spencer, D. W., Bacon, M. P., & Brewer, P. G. (1981). Models of the distribution of 210Pb in a section across the North Equatorial Atlantic Ocean. *Journal of Marine Research*, *39*, 119–138.

Stuart, F. M., Turner, G., Duckworth, R. C., & Fallick, A. E. (1994). Helium isotopes as tracers of trapped hydrothermal fluids in ocean-floor sulfides. *Geology*, *22*(9), 823–829.

Tagliabue, A., Bowie, A. R., DeVries, T., Ellwood, M. J., Landing, W. M., Milne, A., Ohnemus, D. C., Twining, B. S., & Boyd, P. W. (2019). The interplay between regeneration and scavenging fluxes drives ocean iron cycling. *Nature Communications*, *10*(1). https://doi.org/10.1038/s41467-019-12775-5

Thomas, E., Turekian, K. K., & Wei, K.-Y. (2000). *Productivity control of fine particle transport to equatorial Pacific sediment*.

Weyer, S., Anbar, A. D., Gerdes, A., Gordon, G. W., Algeo, T. J., & Boyle, E. A. (2008). Natural fractionation of 238U/235U. *Geochimica et Cosmochimica Acta*, *72*, 345–359.

Young, C., & Lupton, J. E. (1983). An ultra-tight fluid sampling system using cold-

welded copper tubing. *Eos Trans. AGU*, *64*, 735.

Yu, E.-F., Francois, R., Bacon, M. P., & Fleer, A. P. (2001). Fluxes of 230Th and 231Pa to the deep sea: implications for the interpretation of excess 230Th and 231 Pa/ 230 Th profiles in sediments. *Earth and Planetary Science Letters*, *191*, 219–230. www.elsevier.com/locate/epsl

3.9 Supplemental Information

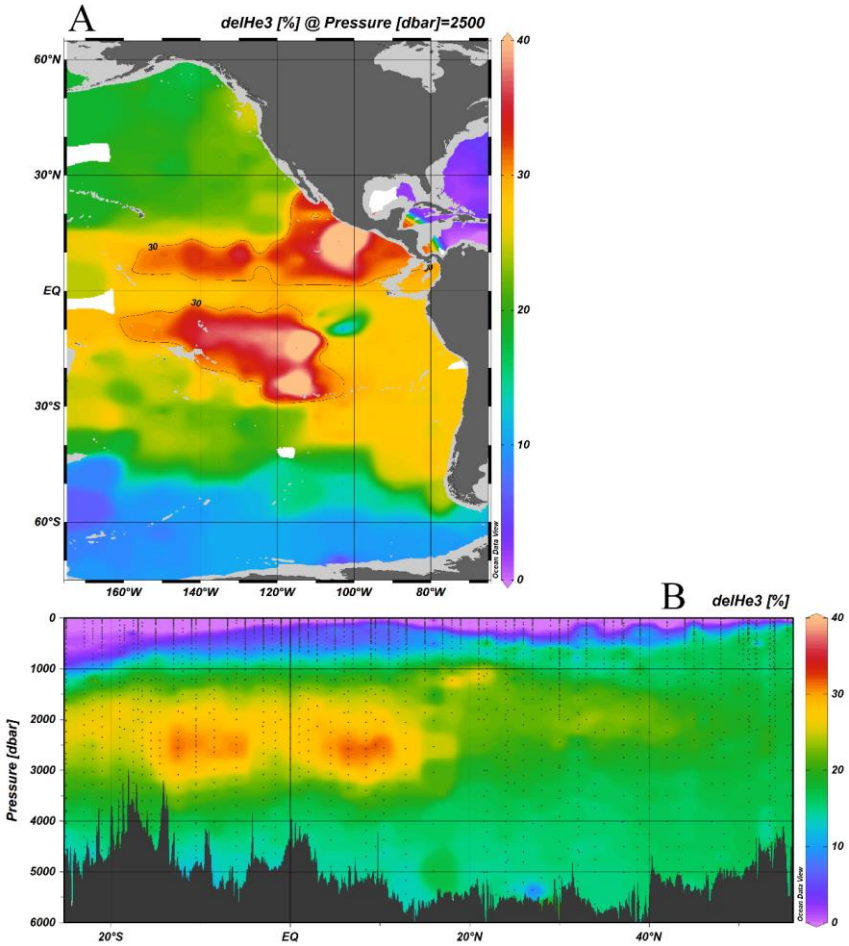

Figure 3.14 *He record at GP15*

δ^3He (%)He at 2500 dbar pressure. B - δ^3He (%) along the 152° W meridian. Both compiled from Jenkins et al., 2019 which includes GP15 (Jenkins et al., 2020). δ^3He is a conservative tracer of deep sea hydrothermal activity and is generally elevated in the Pacific due to activity from the East Pacific Rise. Two plumes of hydrothermal δ^3He originate from the eastern basin and are advected westward. Their maximum enrichments occur at ~10° N and S respectively with semi-depleted values near the equator.

CHAPTER IV – INFLUENCE OF MID-ATLANTIC RIDGE HYDROTHERMAL ACTIVITY ON ^{230}TH AND ^{231}PA SCAVENGING FROM GEOTRACES GA13 FRIDGE

4.1 Abstract

Hydrothermal activity alters the chemistry of the deep ocean and is important in many different global geochemical budgets. This imprint can be surprisingly long-lived and potentially serves as a source or sink of elements up to 1000s of km from its source. While there is much research about the effects of hydrothermal particles on scavenging, or the adsorption and sinking of elements by marine particles, close to vent sites, much less is known about the regional impact of hydrothermal scavenging. Here, we present dissolved seawater concentrations of ^{230}Th and ^{231}Pa, two elements that help indicate scavenging intensity, for 7 hydrothermal sites in the North Mid-Atlantic Ridge as part of GEOTRACES section GA13. Changes in the distribution of ^{230}Th and ^{231}Pa due to hydrothermal activity were estimated by comparison to historical profiles with similar organic particle flux, dust deposition, and water mass aging, then attributing deviation in concentration profile to hydrothermal influence. We find that hydrothermal depletions of ^{230}Th and ^{231}Pa at our site can be explained by simple dispersal of hydrothermal particles from areas with active venting and dilution of this depleted water as it mixes with seawater. Open questions remain, however, about how the precise timing and scale of vent water dispersal impact concentrations of ^{230}Th and ^{231}Pa off the ridge system. We recommend that future modeling parameterize hydrothermal scavenging by predicting ^{230}Th and ^{231}Pa distributions, and potentially other radiotracers, at sub-degree resolution

over the MAR. This would allow basin-scale hydrothermal features to be incorporated into global budgets.

4.2 Introduction

The GEOTRACES program has identified the interactions between oceanic crust and seawater as one if its four main interfaces important in the flux of trace elements and their biogeochemical cycling (Anderson, 2019). Occurring in all ocean basins, hydrothermal activity imprints deep ocean chemistry and potentially impacts global-scale biogeochemical cycles, serving as both a source and as a sink for various trace elements. When hydrothermal vent fluid is discharged at mid-ocean ridges, it reacts with cold, oxygenated bottom waters and forms a range of trace element sulfide/oxide precipitates, such as Fe and Mn oxyhydroxide (German et al., 1991; Lupton et al., 1985). These particle phases become entrained within the rising buoyant waters of the hydrothermal plume and potentially are carried for hundreds of kilometers through progressive mixing, lateral dispersion, and advective transport (German, Fleer, et al., 1991; Lupton et al., 1985). This process potentially impacts global micronutrient budgets by acting as a source of Fe to distal upwelling areas (Fitzsimmons et al., 2014). However, hydrothermal particles can also act as a sink of dissolve elements to the sediment record. The process of scavenging, or the removal of adsorption-prone elements from seawater by sticking to sinking marine particles, is enhanced in areas of strong particle flux like hydrothermal plumes. Hydrothermal effects have been observed to cause strong removal in areas proximal to the active vent site (German, et al., 1991a), and more recently, this effect has been seen up to thousands of kilometers away (Hayes, et al. 2015; Lopez et al., 2015; Pavia et al., 2018). Th and Pa are two elements that are strongly insoluble and will

quickly scavenge to sinking particles, making them valuable for tracing the scavenging process and the burial of other trace elements buried by this process. Th and Pa have been used to show basin-scale enhanced removal from hydrothermal activity observed in the Pacific (Lopez et al., 2015; Pavia et al., 2018, Chapter 2 of this dissertation) and to some degree in the Atlantic (Hayes, et al., 2015). Hydrothermal depletions of Th and Pa observed far from the ridge site have been attributed to *in-situ* scavenging of water at the ocean ridge system (Lopez et al., 2015; Pavia et al., 2018, Chapter 3 of this dissertation), which are then advected to elsewhere in the ocean. The degree of active scavenging by hydrothermal particles at these distal sites is still a subject of debate (Lopez et al., 2015; Pavia et al., 2018). The presence of hydrothermal activity causes our expectation for the burial of scavenging-prone elements to change compared with the case in which hydrothermal activity is absent. It has been hypothesized that, due to the large geographic scale of potential hydrothermal scavenging effects, these processes may represent regional sinks of Th and Pa (Hayes et al., 2015) and other important trace elements.

Our first goal in this study is to see if hydrothermal activity and its effect on particle scavenging can be seen in the distribution of Th and Pa profiles along several sites on the northern Mid-Atlantic Ridge. A large part of identifying hydrothermal scavenging is tied to our ability to predict Th and Pa distributions based on other drivers of scavenging in the North Atlantic. After this, our next goal is to use these distributions to qualitatively describe specifics of scavenging at active vent sites and in the surrounding axial valleys, assessing the potential of these processes to affect the burial rate of trace metals. Finally, we look to understand how these processes impact geochemical cycles both close and away from the ocean ridge system.

Both ^{230}Th (half-life of 75.58 x 10^3 y, Cheng et al., 2013) and ^{231}Pa (half-life of 32.76 x 10^3 y, Robert et al., 1969) are long-lived radionuclides formed from the decay of ^{234}U and ^{235}U, respectively (Andersen et al., 2010; Delanghe et al., 2002; Robinson et al., 2004; Weyer et al., 2008). Due to the uniform distribution of U in well oxygenated areas of the ocean, the input of these elements into seawater is stable and fairly well constrained in the marine system (Costa et al., 2020). The residence time of Th is < 40 y (Bacon & Anderson, 1982) and Pa is < 200 y (Henderson & Anderson, 2003). The distribution of these elements in the water column is primarily set by two parameters; 1. Sinking particle flux / composition, and 2. Redistribution.

If lateral fluxes are neglected, the distribution of Th and Pa are expected to be set by reversible scavenging, an equilibrium of adsorption and desorption of elements onto sinking particles with a constant flux over depth (Bacon & Anderson, 1982). This model predicts that scavenged radionuclides will increase in concentration over depth linearly and that this change is concentration is directly tied to the strength of particle flux (Bacon & Anderson, 1982; Henderson & Anderson, 2003). Examples of this distribution of Th and Pa can be seen in much of the open North Pacific, where the upper water column distribution is dominated by the flux of organic matter (Luo, 2017, Chapter 2 of this Dissertation). As this model assumes a constant particle flux, deviations from reversible scavenging profiles are potentially useful in identifying areas where particle flux changes at depth, such as scavenging from nepheloid layers, or where redistribution is occurring from ocean circulation or lateral flux. Previous studies have used deviations from the linear slope of ^{230}Th and ^{231}Pa to identify hydrothermal scavenging (Deng et al., 2014; Hayes et al., 2015; Lopez et al., 2015; Pavia et al., 2018, Chapter 2 of this Manuscript);

however, this approach alone is inappropriate for use in this study as our sites are impacted by advective transport (Y. Luo et al., 2010; Moran et al., 1997). As hydrothermal particles should have a powerful effect on scavenging intensity, we will instead compare distributions of ^{230}Th and ^{231}Pa to (1) particle beam attenuation coefficient measured by transmissometer (Cp), a proxy for particle concentration, (2) dissolved Fe (dFe), which is a proxy for hydrothermal influence and potentially related to waters of higher scavenging intensity, and (3) ^{3}He/^{4}He, an inert, conservative tracer of hydrothermal influence showing primordial He degassed from the Earth's mantle (Lupton & Craig, 1981; Stuart et al., 1994).

Atlantic Meridional Overturning Circulation significantly affects the dissolved distribution of ^{230}Th and ^{231}Pa in the North Atlantic. Previous studies have demonstrated that distributions of ^{230}Th and ^{231}Pa distributions in deep water are significantly altered by the recent ventilation of North Atlantic Deep Water (Luo et al., 2010; Moran et al., 1997; Van Der Loeff & Berger, 1993). Recently formed deep waters are depleted of ^{230}Th and ^{231}Pa because of vertical mixing of the water column; these lower concentrations are then injected at depth and propagated along deep flow paths. As this water mass ages, concentrations of ^{230}Th and ^{231}Pa increase due to exchange with sinking particles, eventually reaching an equilibrium, resembling reversible scavenging, based on each element's residence time (Moran et al., 1997; Van Der Loeff & Berger, 1993).

4.3 Methods

4.3.1 Cruise Setting and Shipboard Collection

The UK FRidge expedition, also known as GEOTRACES section GA13, or JC156, was a voyage along the northern Mid-Atlantic Ridge between Southampton, UK,

to Guadeloupe, France during the winter of 2017 / 2018 on Royal Research Ship *James Cook*. The main goal of this campaign was to evaluate the mechanisms driving the intensity of hydrothermal trace metal plumes at various hydrothermal sites and the distribution of trace metals within and without of the ridge system. Targeted sampling of buoyant hydrothermal plumes was done by detection with various methods including CTD casts, light scattering, and oxidation reduction potential (Lough et al., 2023). Sites for this study have previously been studied and include (north to south, Fig. 4.1) Menez Gwen (Fouquet et al., 1994; Klischies et al., 2019), Rainbow (German et al., 1990, 2010), S-OH1 (Bideau et al., 1998; Gràcia et al., 2000), Hayes Fracture Zone (Feden et al., 1975), Lost City (Kelley et al., 2005, 2007), Broken Spur (James et al., 1995), TAG (Rona et al., 1993). Shipboard collection of water was done using GEOTRACES standard protocol (Anderson et al., 2012). For each sample, 4 L of 0.45 μm filtered water was collected via Niskin bottles. Th and Pa were sampled in 19 locations total (Fig. 4.1). Four of these sampling stations; S-OH1, Hayes Fracture Zone, TAG, the second north of TAG station, were full profiles from the surface to bottom depth. A partial profile of only surface and deep samples was taken at the valley wall at TAG up to 2500 m. The remaining 10 stations, which included cross-sections around Rainbow and TAG, Menez Gwen, Lost City, and Broken Spur, were taken at depths that targeted hydrothermal activity for that vent site. For the cross-section of Rainbow these depths were between ~1500 – 2600 m and for TAG between ~2400 – 4200 m. Samples were stored filtered and unacidified until returned to the laboratory at USM. They were then acidified to 0.01 M hydrochloric acid (pH = 2) with optima acid and not analyzed until at least 2 months after acidification.

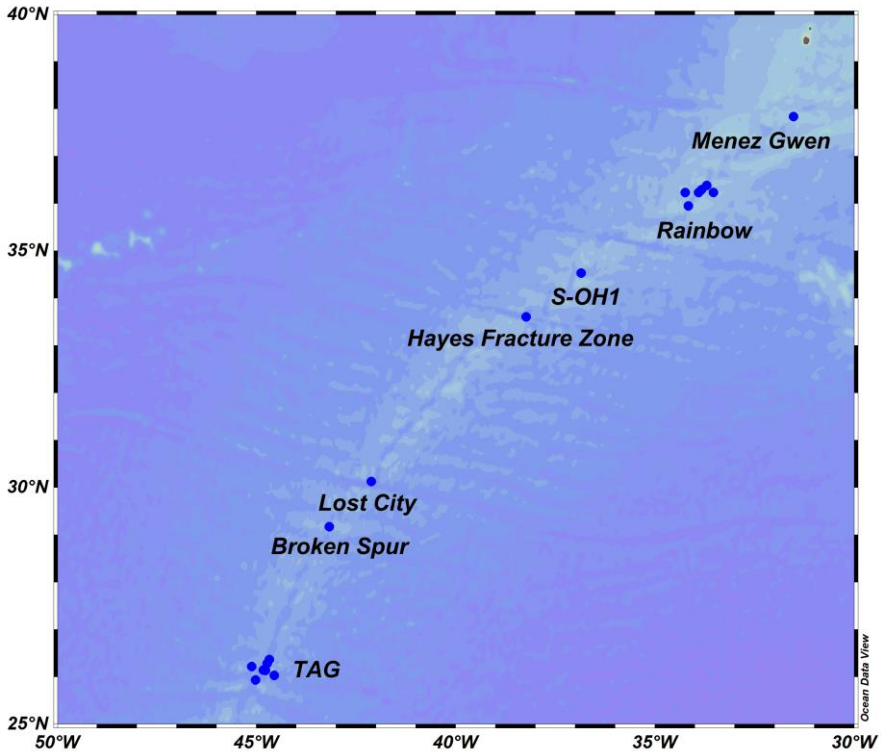

Figure 4.1 *Map of GEOTRACES GA13 FRidge*

Map showing the major vent sites sampled during GA13 for Th and Pa.

4.3.2 Dissolved Th and Pa

The procedure for measuring Th and Pa can be found in the methods of the previous chapter (modified from Anderson et al., 2012; Auro et al., 2012; Hayes et al., 2015c), but is summarized as follows: Th and Pa were concentrations were measured by isotope dilution with inductively coupled plasma-mass spectrometry. Acidified water samples were spiked with aliquots of ^{229}Th and ^{233}Pa and allowed to equilibrate for 1 day. $FeCl_3$ was added to the samples and pH was adjusted with ammonium hydroxide to collect Th and Pa as Fe (oxy)hydroxide particles. This precipitate was digested in a series of OPTIMA grade HCl, HF, and HNO_3. Elements were separated by anion exchange

column chromatography. We encountered two different laboratory errors that reduced the final data resolution. Pa counts at Menez-Gwen (6), S-OH1 (20), Lost City (23), and some of Rainbow (16) were initially below detection limit. We eventually found this was a laboratory error due to incomplete elution of Pa from the resin columns, and methods were adjusted for future samples, although these locations were unable to be redone. Additionally, a small number of samples were unable to be run for either Pa or Th where during the acid digestion step, these samples would form thick solid precipitates, which was unable to be dissolved enough for use with the inductively coupled plasma-mass spectrometer. Of 134 total samples collected, 132 samples was measured for ^{230}Th, 120 samples were measured and above the detection limit for ^{232}Th, and 97 samples were measured for ^{231}Pa.

4.3.3 Transmittance

The particle beam attenuation coefficient (Cp) of 660 nm light as measured by transmissometer has been found to be linearly correlated with particle concentrations for upper water column particulate organic carbon (Bishop, 1999; Gardner et al., 2006) and for benthic nepheloid layers of resuspended sediment (Gardner et al., 1985, 2018). As the relationship between Cp and particle concentration is known to vary with particle size and composition, hydrothermal particles likely have a unique response on beam attenuation. We assume that a change in particle concentration due to hydrothermal particles will correlate with a linear change in beam attenuation coefficient, which is potentially useful in inter-comparing particle concentrations between the two casts taken for each station site. Transmissometers are prone to contamination with prolonged use, potentially shifting baseline transmittance throughout a cruise, by the buildup of

particulate film on the sensor lens. The correction for this is to set some part of the water column to be assumed particulate free, a clear water minimum, as 100% transmittance (Bishop & Wood, 2008). A cruise-wide maximum transmittance of 99.7% occurred around 3 km from the ridge. Using the cruise-wide clear water minimum as a reference, transmittance was shifted +5.7% for all stainless steel rosette casts, except +5.718 for Cast 60 and +5.855 for Cast 69 which were slightly adjusted to match deepwater minimums. For the trace metal rosette, multiple drifts in baseline were observed, which to a degree were grouped by station. These baselines were shifted by matching stainless steel rosette casts from the same station and maintaining a relatively consistent mid-water particle minimum (Tab. S1). The con of this approach is that it makes it difficult to compare different stations for changes to background particle concentration, but should be adequate for identifying changes to beam attenuation from hydrothermal particles. From this corrected transmittance, the particle beam attenuation coefficient was calculated as: Cp = -4 * ln (transmittance) [1/m] for transmissometers with a 25 cm pathlength.

4.3.4 Approach

A fundamental problem this study deals with is determining the degree to which we can separate changes in scavenging intensity due to hydrothermal particles from other processes. This partly arises from limitations in Th/Pa sampling, which was done to reduce project cost. Since prior work had established some context for the Th/Pa in North Atlantic waters (Deng et al., 2014; Hayes et al., 2015; Luo et al., 2010) it was decided on this expedition that Th/Pa sampling would be targeted mainly to hydrothermal plume waters. Unfortunately, at sites with only plume samples, we lack context from the upper

water column which potentially informs us about other scavenging processes. Our goal is to contextualize these hydrothermally targeted measurements by estimating background scavenging regime using complementary information to account for other scavenging factors and combine our expectations of these with historical profiles to assess the background scavenging at our sample sites. In the open North Atlantic, we broadly expect the distribution of Th and Pa concentration to be set by a combination of particle rain, such as from organic particle flux, deposition of aerosol minerals, nepheloid layers, hydrothermal particles, and lateral dispersal of Th and Pa by advection or eddy diffusion, such as the effects of overturning circulation.

To gauge particle rain, we primarily look to organic particle flux. Satellite-derived, annually averaged surface chlorophyll from Aqua MODIS (Fig. 4.2) is generally low across our sampling sites, but has a north-south gradient going from ~0.5 mg/m^3 at Rainbow to ~0.1 mg/m^3 at TAG. Our expectations for this as a proxy for organic particle rain is that concentration distributions of Th and Pa will be lower at northern stations and higher at southern stations. Although our site region exists outside of the primary deposition of Saharan dust, the impact of mineral aerosols potentially is different enough between sites to alter expectations of scavenging intensity. There is a degree of uncertainty in determining annual dust flux in the open North Atlantic as models of the North African dust plume are often constrained by sediment cores and traps close to the African and North American continents. Older models, such as from Mahowald et al., 2005 suggest a bigger change across our sites, ranging from ~1.17 $g/m^2/y$ at Rainbow to ~3.48 $g/m^2/y$ at TAG (Anderson et al., 2016; Jickells et al., 2005.; Luo et al., 2003; Mahowald et al., 2005); however, newer models suggest that both the total particle load

and difference between sites is much smaller, ranging from ~0.32 g/m^2/y at Rainbow to ~0.9 g/m^2/y at TAG (Albani et al., 2015; Hayes & Wallace, 2019). The expectation for differences between sites due to Saharan dust flux is opposite that of organic particle flux, in that it would drive more scavenging in the south than in the north. However, as export production for this region is roughly an order of magnitude higher than dust flux, about ~10 g/m^2/y (DeVries & Weber, 2017), we expect export production to the be the primary factor driving sitewide differences in particle concentration. Transmissometer data is also useful in this context. Although we cannot use it to compare the background particle concentration between stations, it can be used to identify depths where particle concentration is elevated from upper or mid-water values. This is useful for determining where scavenging from hydrothermal particles is occurring *in-situ* as opposed to solely the mixing of water that has been previously scavenged.

The southern transport of Th- and Pa- depleted North Atlantic Deep Water plays a large role in the distribution of these elements throughout the basin (Cochran et al., 1987). Deep circulation near the Mid-Atlantic Ridge below 2000 m is generally parallel with the ridge system (Reid, 1994), and our general expectation is that water age generally increases southward and with water depth at our sampling sites. We use estimates of mean age of seawater, representing the time since a water parcel has been in contact with the surface, from Khatiwala et al., 2012 which is derived from radiocarbon, CFCs, PO_4^*, temperature, and salinity (Figs. 4.3 and 4.4). Because mean age increases with depth, it is important that any reference we use has a similar age and age distribution to our sampling site. The net result of both changes in organic particle rain and NADW

ventilation age throughout our sampling sites is that Th and Pa concentrations and inventories are expected to be less in the north and increase southward.

There is an unfortunate dearth of historical dissolved Th and Pa profiles in the open North Atlantic Ocean that are both near the mid-ocean ridge system and potentially free from hydrothermal effects. We will primarily use KN204-01, a 2011 cruise which was part of GEOTRACES section GA03, also known as GT11 (Hayes et al., 2015), which runs from Massachusetts, United States to Cape Verde/Mauritania, for these references as it has the most proximal stations and an intercalibration at TAG. Additionally, we will use EN328 – 9, a North-Eastern Atlantic site, and a 2-D overturning circulation model of ^{230}Th and ^{231}Pa distribution with latitude from Luo et al., 2010. Full dissolved profiles for this study were limited to TAG and two interridge sites, Hayes Fracture Zone and S-OH1, that have no active venting (Gràcia et al., 2000). These interridge sites are potentially useful in determining the background scavenging intensity; however, even these sites might also reflect a mixed integration of depleted water from within the ridge system (German et al., 2010; Hayes et al., 2015). While we look to historical measurements for this study, we propose that in the future, modeling combining the effects of circulation and organic particle flux effects on ^{230}Th and ^{231}Pa distributions should be used to better approximate the degree of *in-situ* scavenging from hydrothermal sources.

The most northern sites from this study present a problem for choosing potential historical sites to reference background scavenging conditions because they are the most distant from potential reference sites. We believe that GT11-10 is a relatively useful reference for Rainbow and other northern sites as it has a relatively similar mean age at

plume depth (80 – 120 y) and has a similar annual surface chlorophyll content (Fig. 4.3). For TAG and other southern sites, the mean age of plume water is generally hard to gauge as there is a strong dichotomy between mean age of deep water on both sides of the ridge system (Fig. 4.4). To account for potential variability proximal to this site, we can look at both GT11-14 and GT11-18 to show the general range of background scavenging. The upper water column of our measured TAG profile suggests that GT11-14 is the better comparison for these sites as upper distributions of ^{230}Th and ^{231}Pa are nearly identical; nonetheless, we can still use GT11-18 as a theoretical maximum bound for Th and Pa inventories within our sampling sites (Fig. 4.5). Similarly, EN328 – 9 (Y. Luo et al., 2010), which has a much younger mean age than our sites and higher annual chlorophyll, acts as a lower bound for these parameters, in that deeper than 1000 m, ^{230}Th concentrations ~5 μBq/kg and ^{231}Pa concentrations below ~3 – 5 μBq/kg must reflect a scavenging process that is not organic particle rain or ventilation of NADW.

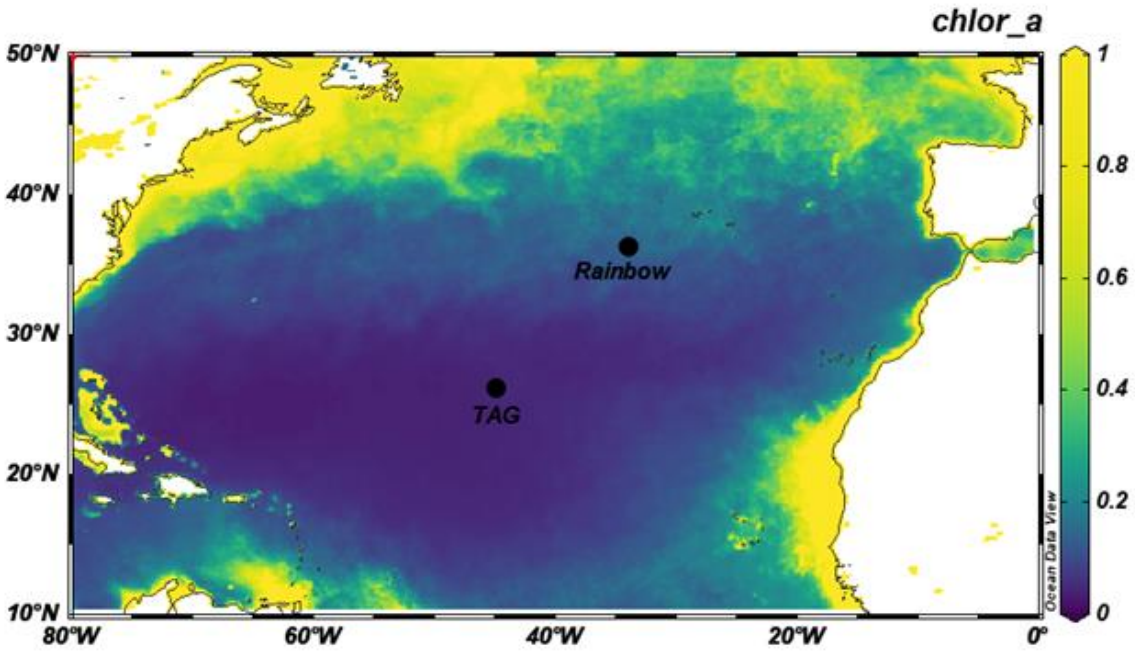

Figure 4.2 *2021 annually averaged surface water chlorophyll a concentrations from Aqua MODIS*

2021 annually averaged surface water chlorophyll a concentrations from Aqua MODIS.

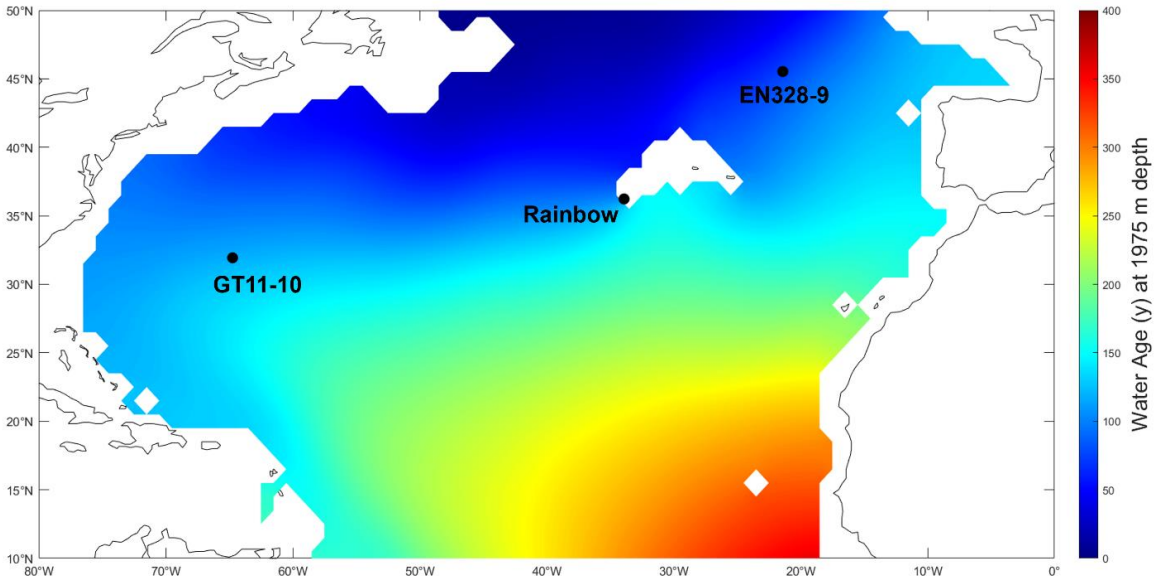

Figure 4.3 *Mean age of seawater at 1975 m*

Mean age of seawater at 1975 m derived from Khatiwala et al., 2012. Station 10 from GEOTRACES GA03 potentially have similar background scavenging to Rainbow because they have similar mean age at this depth and similar flux in organic particles.

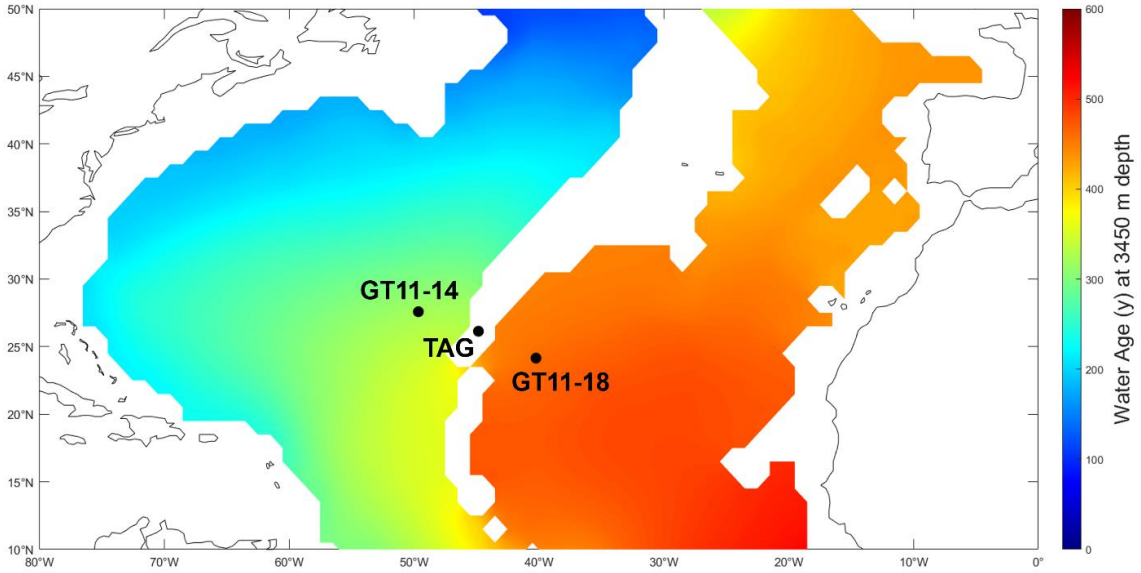

Figure 4.4 *Mean age of seawater at 3450 m*

Mean age of seawater at 3450 m derived from Khatiwala et al., 2012.

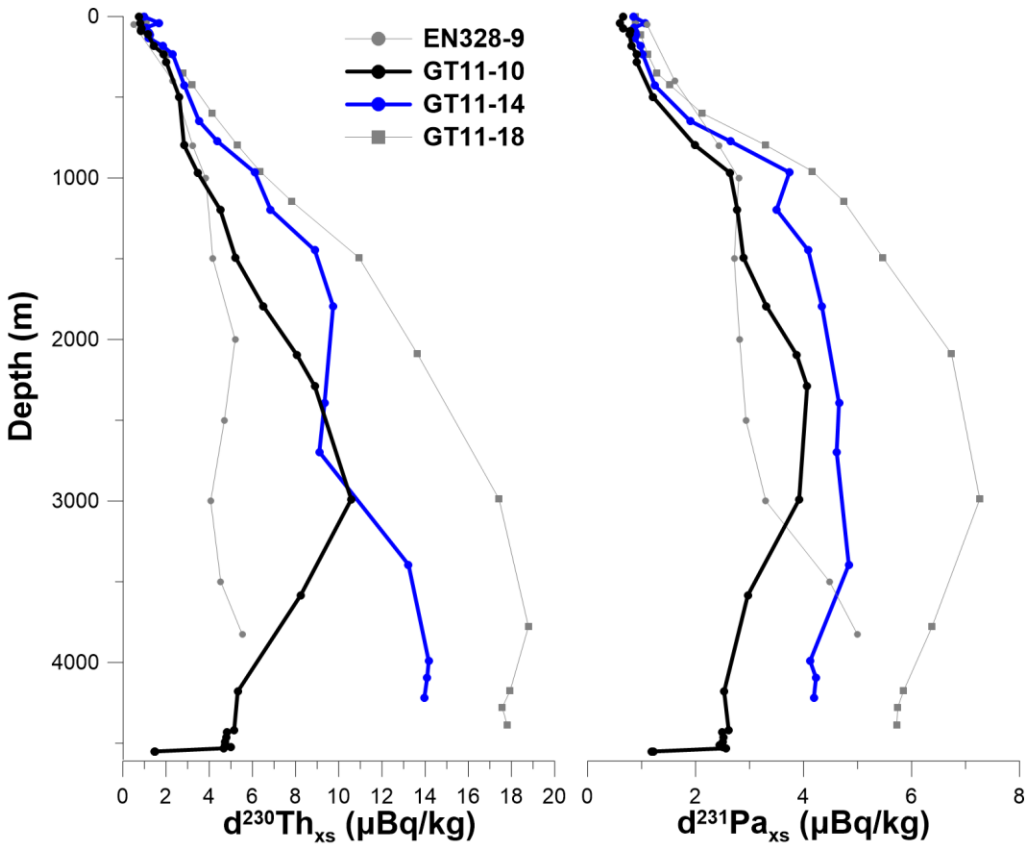

Figure 4.5 *Atlantic reference profiles*

Four previously published profiles used as references for this study. EN328-9 (gray circles, Luo et al., 2010) is the most northward of these sites and shows ^{230}Th and ^{231}Pa concentration inventories that should be generally lower than the background we would expect at Mid-Ocean Ridge sampling sites. GT11-10 (black) and GT11-14 (blue) (Hayes et al., 2015) were chosen as reference stations for Rainbow and TAG respectively. GT11-18 (gray squares, Hayes et al., 2015) is a reference for conditions with slightly higher ventilation age and lower surface chlorophyll than seen at our sampling sites.

4.4 Results

4.4.1 Intercalibration at TAG and Variability in Plume Sampling

The TAG hydrothermal field is a well-studied vent site that functioned as an intercalibration site in the 2017 GA13 expedition between this cruise and previous GEOTRACES cruise GA03, which sampled the same location is 2011. There is

significant similarity between both casts in the dissolved phases of Fe, $^{230}Th_{xs}$, and $^{231}Pa_{xs}$ in the water column above the buoyant plume to 3000 m (Fig. 4.6). Below this, all metrics feature some degree of offset in depth or concentration. Both records of dFe share the same basic distribution where above 3000 m dissolved concentrations are < 2 nmol/kg. Concentrations are elevated to >20 nmol/kg between ~3000 – 3500 m with a slight "dip" to ~30 – 40 nmol/kg near 3400 m. The TAG cast from GA13 shows slight differences in the $^{230}Th_{xs}$ concentrations in that where concentrations are lower is in a narrower depth range, however the overall pattern and degree of concentration changes are similar. There are noticeable differences in the distribution of $^{231}Pa_{xs}$ distributions below 3000 m. In the GA03 cast is between 3000 – 3500 m is ~1 μBq/kg lower than the concentration above it whereas the GA13 cast profile drops at 3200 m by ~4 μBq/kg before the values become relatively similar again at 3500 m.

Some of this variability between both profiles in all measurements might be accounted for by differences in each cast's relative position to the plume or a change in position of the plume relative to the vent site (Lough et al., 2023). During GA13, each station consisted of two casts: (1) a stainless steel rosette of which dFe was measured and (2) a trace metal rosette where He, Th, and Pa were taken. It is plausible that the orientation from each of these casts is capturing a slightly different relative position of the buoyant plume. Different casts at Rainbow seem to support this variability due to sampling technique as 6 casts were made at the vent site where peak particle concentration, determined by transmissometer, varied both in degree and by as much as 400 m in depth (Fig. 4.7). This discrepancy is important to consider for interpretations of dFe and He/Th/Pa as each element group was taken during different casts and are

potentially offset from each other. Applying this potential offset between sites, we may expect variation due to cast position to affect parameter values to some degree even when there are not any environmental factors changing their distribution.

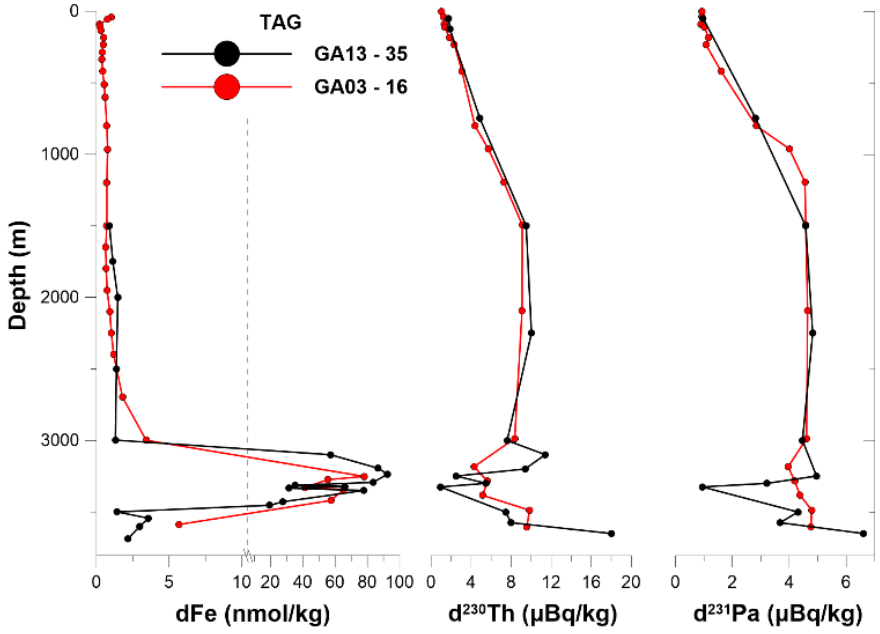

Figure 4.6 *Intercalibrations at TAG between GEOTRACES GA13 and GA03*

Intercalibrations at TAG between GEOTRACES GA13 (black, 2017, this study) and GEOTRACES GA03 (red, 2011).

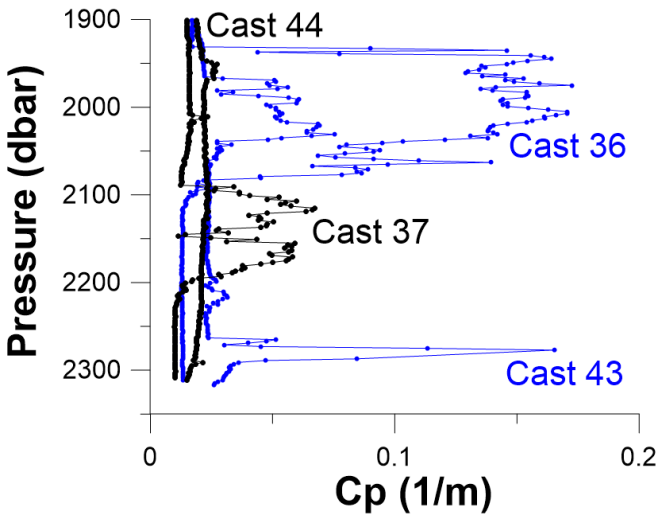

Figure 4.7 *Transmissometer data from Rainbow*

Transmissometer data taken from four casts at Rainbow (stations 16 and 38) showing particle concentration with depth. These casts roughly show the expected variability in measuring particle concentration due to position of the CTD rosette. Th, Pa, and He were taken by a single trace metal rosette cast and are shown in black. dFe was taken by stainless steel rosette and are shown in blue.

4.4.2 Th and Pa at Major Sites

High resolution particle beam attenuation coefficient for each major vent site is shown in Figure 4.8. Relative increases from each station's baseline, which ranged from ~0.10 – 0.15 m^{-1}, show depth ranges where hydrothermal particles are present. Figure 4.8 shows parameters from both casts taken at each station (1) dFe and (2) He isotopes, ^{230}Th, and ^{231}Pa.

Menez Gwen (station 6, Fig. 4.9 red x) is the among the shallowest venting sites in this study (<1000 m), showing relative increases in dFe concentration and ^{3}He/^{4}He at ~750 m depth. Menez Gwen has the youngest expected mean age since ventilation (<100 y) of plume water and is located in the highest area of organic flux amongst our sites. Given this, we might expect the background ^{230}Th distribution for Menez Gwen to have the lowest concentrations amongst our sites and be similar or less than that of GT11-10.

However, measured ^{230}Th concentrations at Menez Gwen are indistinguishable from or slightly exceed concentrations measured at GT11-10 and model estimates of this latitude from Luo et al., 2010. From this, we are unable to ascertain to what degree, if any, scavenging is occurring from hydrothermal particles at this site. Lost City (station 23, Fig. 4.9 light blue diamond) is in a very similar situation. It should be noted that transmissometer data from both sites are taken <1000 m and are indistinguishable from the other upper water column of other sites. Lost City shows very little, if any, increase in dFe or ^{3}He/^{4}He compared to sites without active vents and has ^{230}Th concentrations ~2 μBq/kg. These concentrations are basically indistinguishable from GT11-10 as a background; however, given that the site is significantly further south, it might be more comparable to GT11-14, which suggests a background ~4 – 5 μBq/kg for this depth. The shallow nature of both of these sites makes determination of specifically hydrothermal scavenging difficult as their change from background conditions is potentially much smaller.

The vent site at Rainbow was sampled twice (stations 16 and 38, Fig. 4.8 blue and green Fig. 4.9 orange circle) which yielded slightly different results between the casts (Fig. 4.7). Cp for both trace metal casts increase ~1800 m, however the degree to which is different and cast 44 shows significantly large increases ~2100 m. Dissolved Fe for both casts was ~1 – 2 nmol/kg in the upper 1500 m, gradually increases to ~4 nmol/kg at 1800 m depth, and then increases dramatically to >15 nmol/kg to the bottom. Both ^{230}Th and ^{231}Pa casts are depleted relative to GT11-10, however the degree and distribution varies between casts. For ^{230}Th, the background distribution suggested by GT11-10 gradually increases from ~6 – 8 μBq/kg at the depth of the non-buoyant plume (Fig. 4.5).

The ^{230}Th concentration at station 38 is roughly homogenous between 0.6 – 2 µBq/kg whereas station 16 has similar ^{230}Th concentrations between ~1860 – 1920 m and below ~2200 m, but is relatively increased approaching ~2100 m by up to 4 µBq/kg. The background distribution of ^{231}Pa at GT11-10 increases from ~3 – 4 µBq/kg. The cast from station 38 is again relatively homogenous between ~1 – 1.5 µBq/kg. The ^{231}Pa concentration at station 16 ranges from ~1 – 3 µBq/kg with its lowest value where ^{230}Th concentration is high. Both casts at Rainbow suggest extreme scavenging and are lower or similar in ^{230}Th and ^{231}Pa concentrations than the low bound suggested by EN328-9. However, the difference between these distributions suggest that what was being sampled by these two casts is not necessarily the same. These discrepancies suggest that some of the physical parameters of the plume were different between the casts, such as a different sample orientation, or that there is potential contamination in station 16, such as by incomplete filtration of water samples causing contamination from the particulate fraction. These casts suggest that ^{230}Th is depleted by anywhere between 38 – 92% and ^{231}Pa is depleted by 13 – 75%.

Both S-OH1 (station 20, Fig. 4.8 brown, Fig. 4.9 yellow triangle) and the Hayes Fracture Zone (station 21, Fig. 4.8 gray, Fig. 4.9 green reversed triangle) have low Cp, dFe, and ^{3}He/^{4}He are low compared to areas of active venting, suggesting that these sites show conditions where little *in-situ* hydrothermal particle scavenging is occurring. Concentrations of ^{230}Th and ^{231}Pa at the Hayes Fracture Zone generally increase with depth, ^{230}Th from ~2 – 5.5 µBq/kg and ^{231}Pa from ~1.5 – 2 µBq/kg. Both distributions are entirely lower than EN328-9, suggesting that the entire site is depleted of these isotopes. The ^{230}Th distribution of S-OH1 is roughly homogenous ~ 6 µBq/kg from ~600 – 2300 m

except for at 2100 and 2200 where concentrations are below 4 μBq/kg. This homogenous distribution is not directly comparable to a reference station as it exceeds both bounds having a higher concentration than GT11-18 <700 m depth and a similar or lower ^{230}Th concentration than EN328-9 below 2000 m.

Broken Spur (station 24, Fig. 4.8 red, Fig. 4.9 dark blue square) has ambient dFe <2 nmol/kg above 2500 m and a narrow depth band of elevated dFe and ^{3}He/^{4}He at ~2600 – 2700 m. The ^{230}Th concentrations are between 3.5 – 6 μBq/kg which is lower than the homogenous background of 8 – 9 μBq/kg and generally, but not entirely, below the lower bound set by EN328-9. ^{231}Pa concentrations at Broken Spur were 0.3 – 1.3 μBq/kg which was significantly lower than GT11-14 at ~4.5 μBq/kg and EN328-9 at ~3 μBq/kg.

While there is a slightly more prominent depth offset for the changes in dFe and ^{3}He/^{4}He at TAG (station 35, Fig. 4.7 purple plus), this site also has the largest change to concentration for these two parameters. The general profiles of TAG for both ^{230}Th and ^{231}Pa increase in the upper 1500 m, are relatively homogenous until 3200 m, are dramatically lower until ~3500 m, and then have increased values towards the bottom. These distributions match the reference profile GT11-14 extremely well except in two places; the dramatic decrease between 3200 – 3500 m and at the very bottom sample. For ^{230}Th this decrease in concentration in the hydrothermal plume goes from the homogenous section of ~9 μBq/kg to 1 – 4 μBq/kg and for ^{231}Pa from ~5 μBq/kg to ~1 μBq/kg. As much as 92% of ^{230}Th and 78% of ^{231}Pa was removed from certain depths in TAG's active plume.

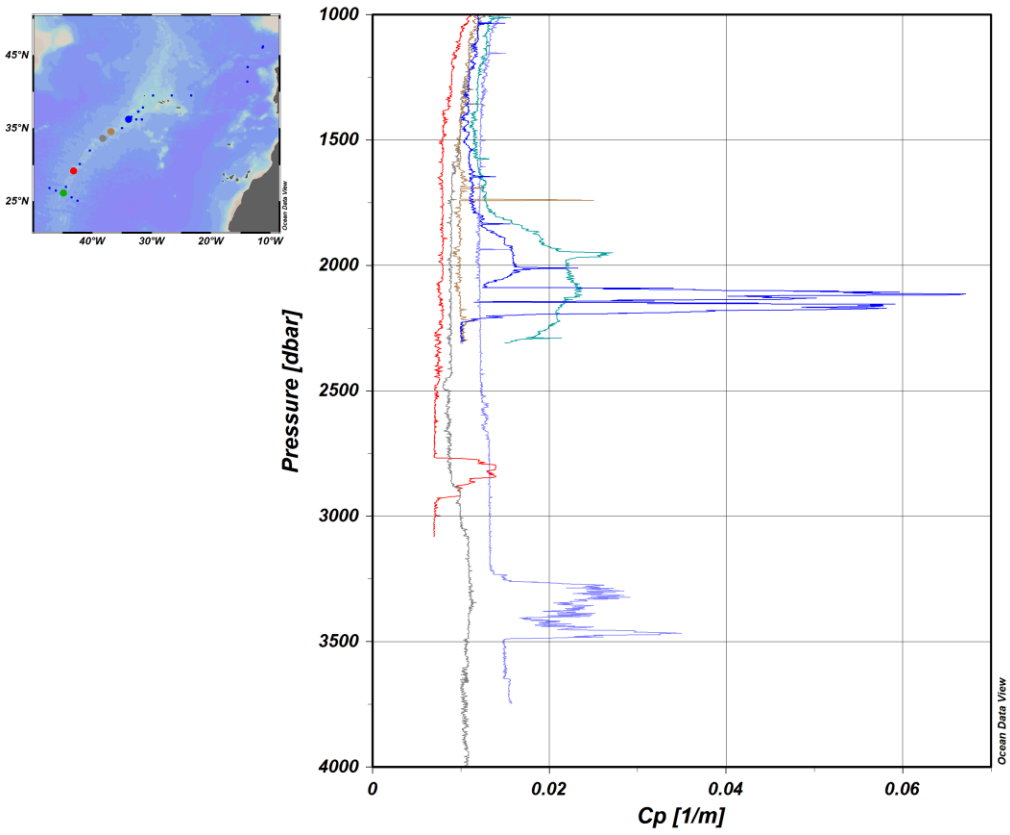

Figure 4.8 *Particle beam attenuation coefficient at each major vent site*

Particle beam attenuation coefficient (Cp) measured by transmissometer at each major vent site. North to south: Rainbow (Blue, cast 36 and Green, cast 44), S-OH1 (Brown, cast 47), Hayes Fracture Zone (Gray, cast 49), Broken Spur (Red, Cast 54), and TAG (Light Blue, cast 76)

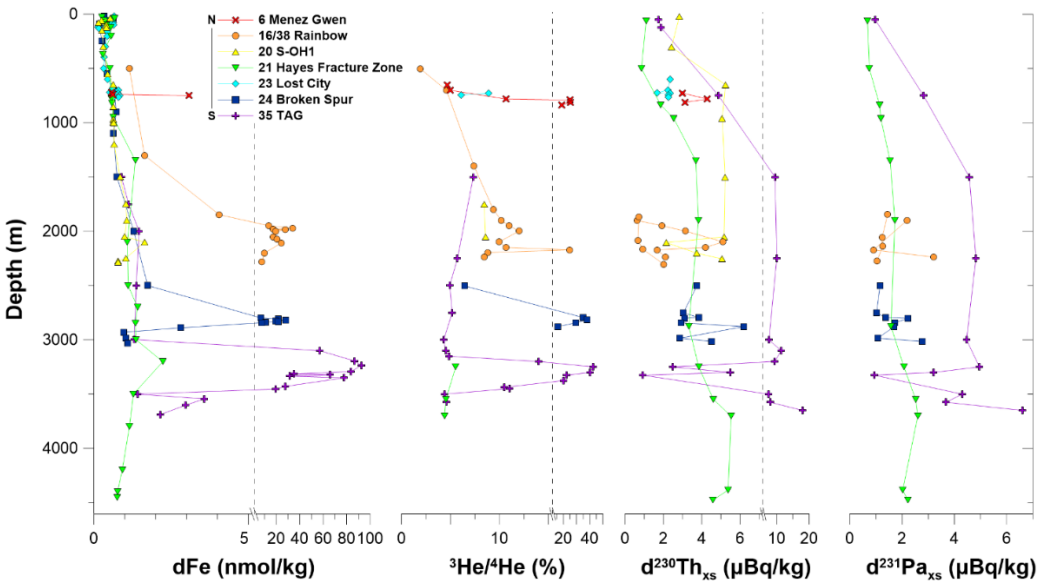

Figure 4.9 *Distribution of hydrothermal activity proxies at major vent sites*

Distribution of dFe, $^{3}He/^{4}He$, $^{230}Th_{xs}$, and $^{231}Pa_{xs}$ at major vent sites.

4.4.3 Rainbow Cross Section

All stations surrounding Rainbow exhibited some type of depletion in ^{230}Th and ^{231}Pa relative to GT11-10 below 1750 m. The four stations surrounding Rainbow share roughly the same dFe distribution, increasing from near 0 to ~2 – 3 nmol/kg at 1800 m depth before leveling off or decreasing slightly and relatively similar $^{3}He/^{4}He$ to the baseline of station 16. On the whole, individual changes in these parameters do not directly correlate to differences in scavenging intensity of ^{230}Th and ^{231}Pa. The site south of Rainbow (station 15) is somewhat different than the other stations in and around the axial valley in that above hydrothermal plume depth, ^{230}Th and ^{231}Pa are nearly identical to the reference at GT11-10. Besides these points at station 16, all other measurements of ^{230}Th and ^{231}Pa are below or within 0.5 µBq/kg of the low bound reference from EN328-9. However, sites vary significantly within hydrothermal depth and the degree can vary as

widely as 6 μBq/kg for ^{230}Th, which obscures the degree of scavenging for these elements. It appears that, to some degree stations east (station 12, Fig. 4.10 light blue triangle) and west (station 13, Fig. 4.10 blue reverse triangle) are more homogeneous and more depleted than stations north (station 14, Fig. 10 red square) or south (station 15, Fig. 4.10 yellow diamond), being closer to the active vent's second cast station 38. The bonus station north of Rainbow (station 18, Fig. 4.10 orange plus) seems to show the effect of the hydrothermal plume as it becomes progressively mixed with seawater. Station 18 shows increased dFe of ~3.5 – 6.5 nmol/kg compared to other stations inside of the axial valley and low ^{230}Th and ^{231}Pa concentrations comparable to Rainbow's second cast station 38.

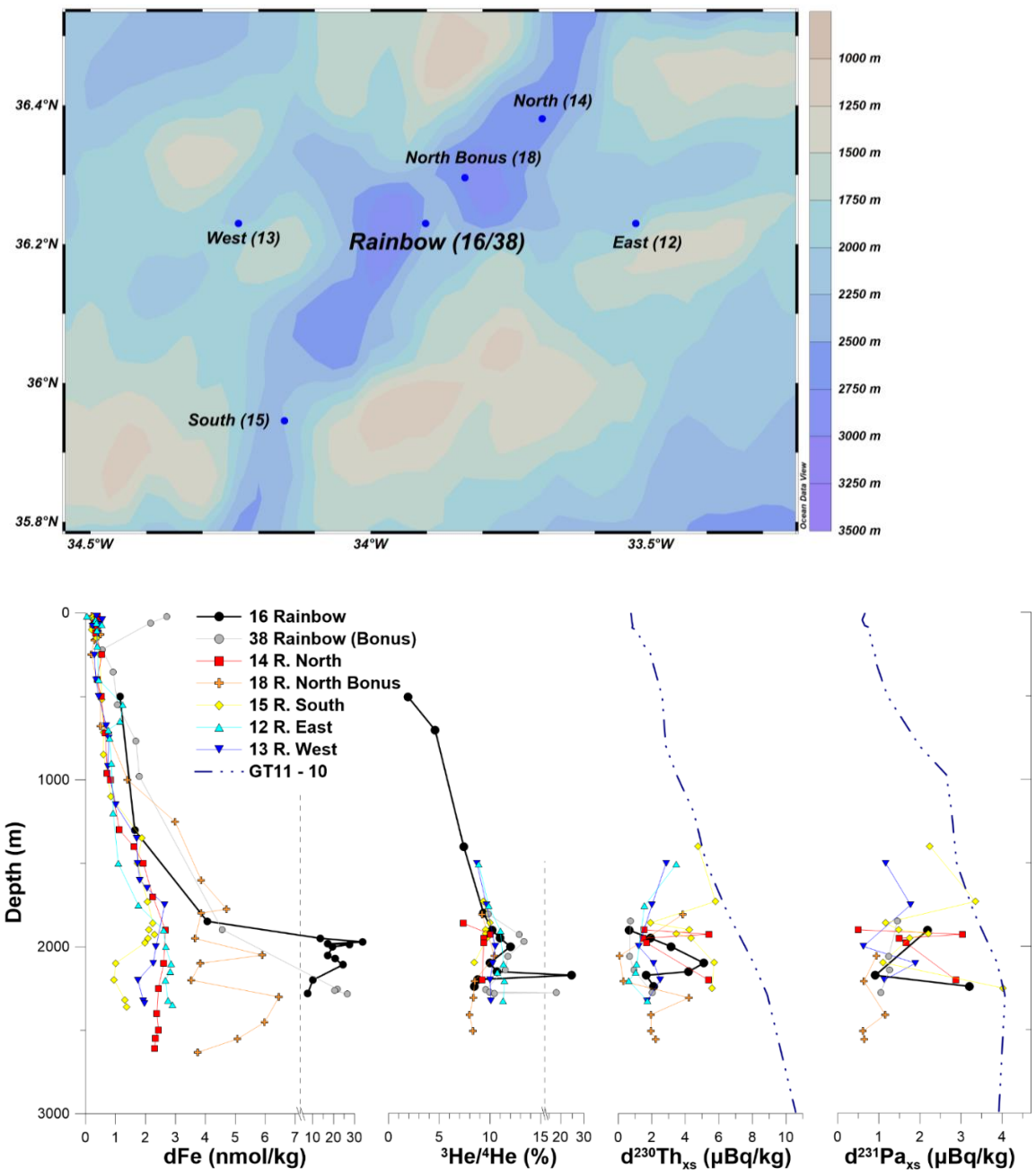

Figure 4.10 *Distribution of elements around Rainbow*

(top) Map of sampling stations near Rainbow. (bottom) Rainbow cross section station profile data from GA17 (location shown in Fig. 4.3). Left to right, dissolved Fe (nmol/kg), $^{3}He/^{4}He$ ratio (%), and dissolved $^{230}Th_{xs}$ (µBq/kg).

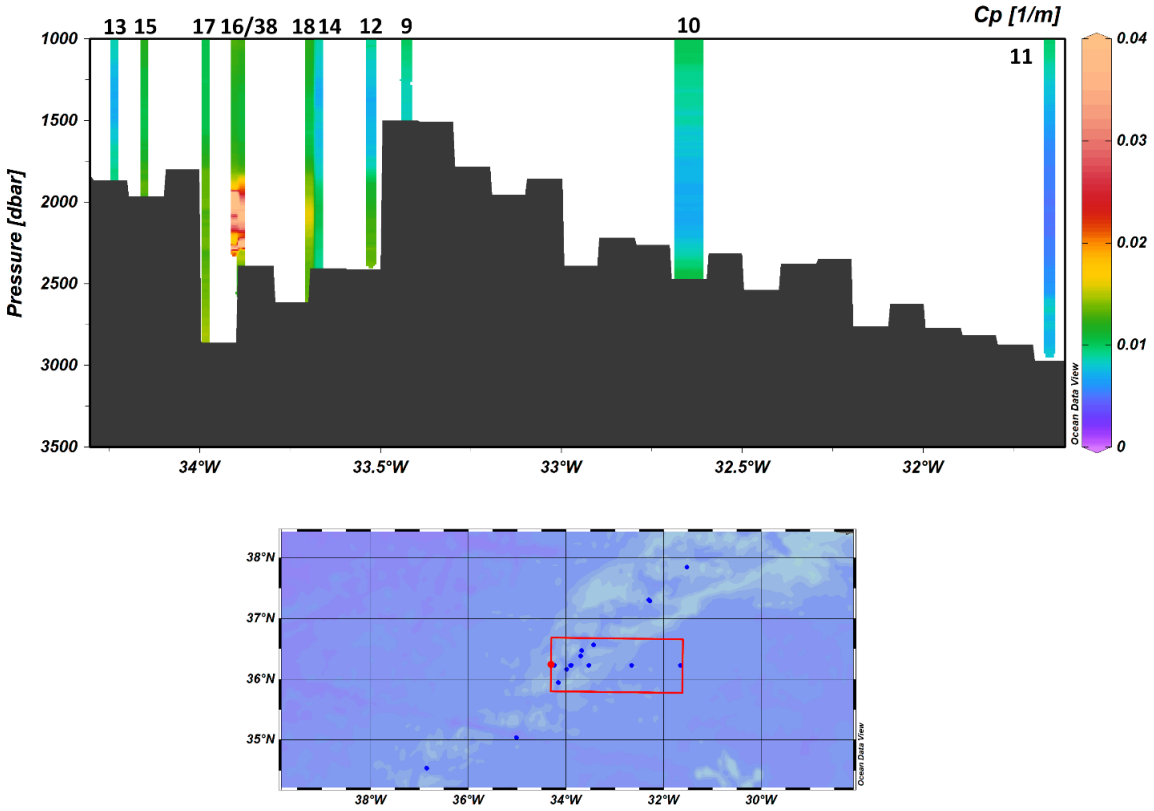

Figure 4.11 *Particle beam attenuation coefficient around Rainbow.*

Particle beam attenuation coefficient for sites near Rainbow.

4.4.4 TAG Cross Section

Generally, the ^{230}Th distribution of stations surrounding TAG can be broken up by stations that are within or outside of the axial valley. Stations inside of the valley are characterized by slightly higher dFe content at plume depth between 2 – 4 nmol/kg, ^{3}He/^{4}He ~2% higher than stations outside of the valley, and overall lower ^{230}Th distributions. The stations within the valley north (station 26 and 36, Fig. 4.9 red squares and orange plus) and south (station 27, Fig. 4.9 yellow diamond) of TAG show relatively homogenous distributions <7 µBq/kg both from 3000 m to the bottom which are relatively on the same scale of depletion as the main vent site. Sites outside of the valley

walls west (station 30, Fig. 4.9 blue reverse triangle) and east (station 31, Fig. 4.9 light blue triangle) of TAG have roughly homogenous ^{230}Th distributions, slightly increasing with a range of ~8 – 12 μBq/kg. This range is very similar to TAG's background distribution between 2500 – 3000 m, but is slightly depleted from the background below 3000 m. ^{231}Pa distribution is generally the same and homogenous among all sites except at the main vent site and ranges from .5 – 2 μBq/kg. For all parameters, the TAG valley wall (station 37, Fig. 4.9 green cross) between ~2000 – 2500 m resembles values for the other stations inside of the axial valley and is relatively depleted in ^{230}Th and ^{231}Pa.

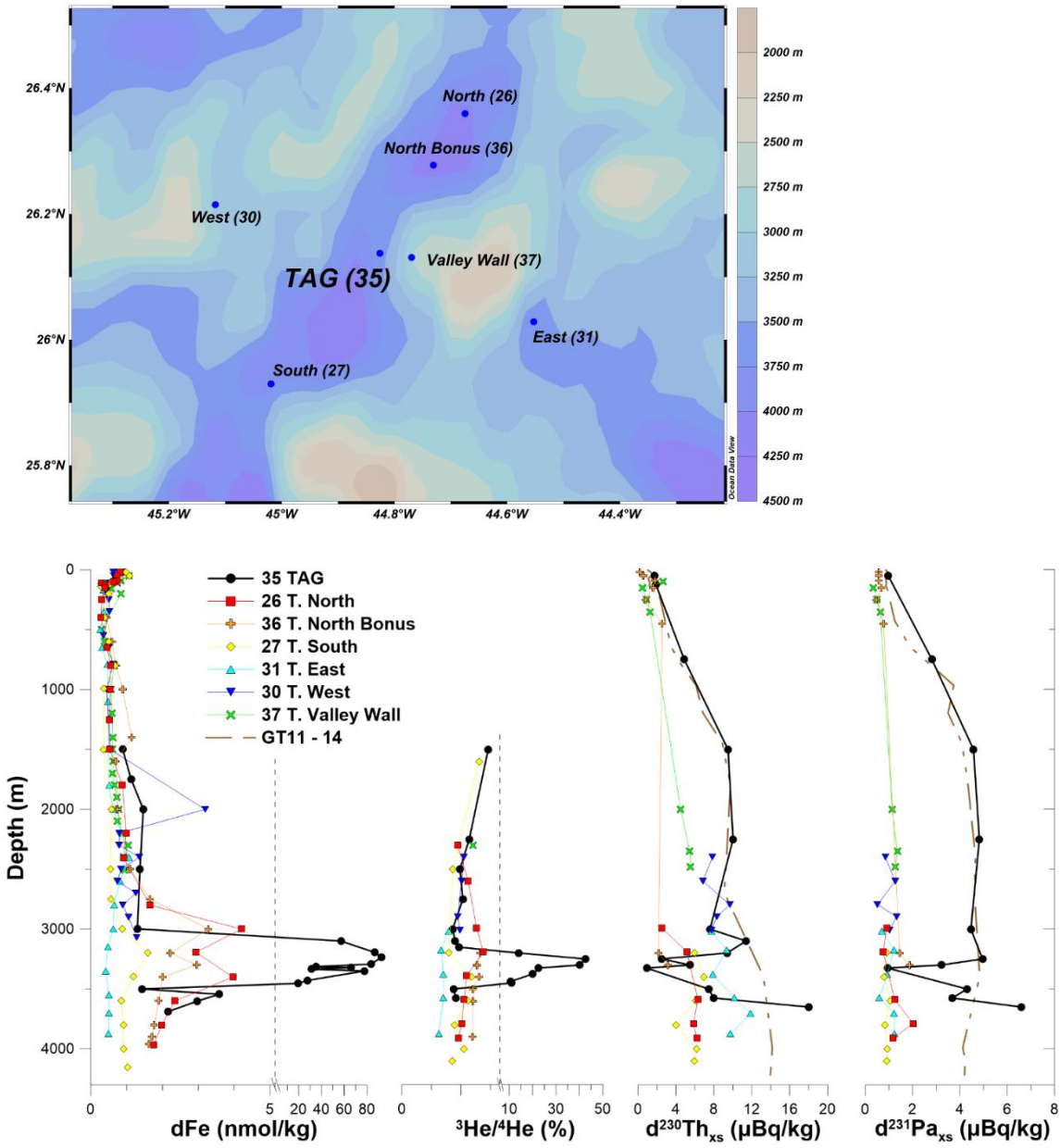

Figure 4.12 *Distribution of elements around TAG*

(top) Map of sampling stations near TAG. (bottom) TAG cross section station profile data from GA17. Left to right, dissolved Fe (nmol/kg), $^{3}He/^{4}He$ ratio (%), and dissolved $^{230}Th_{xs}$ (µBq/kg).

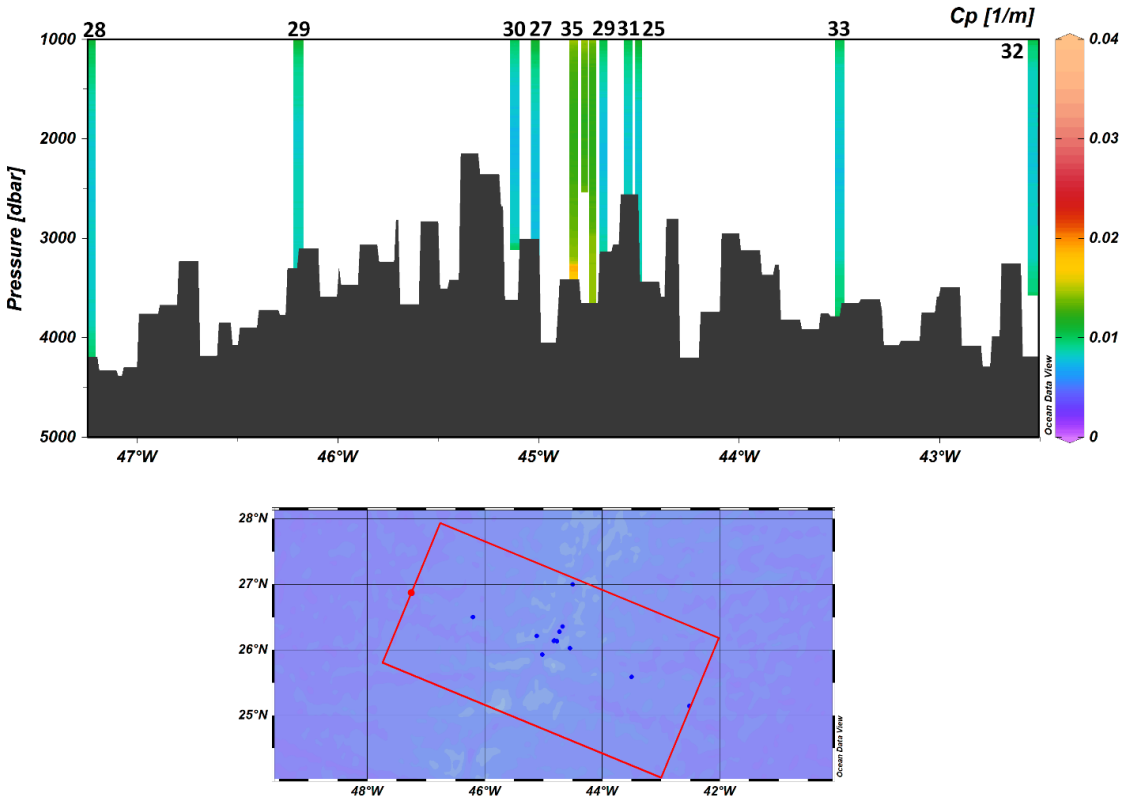

Figure 4.13 *Particle beam attenuation coefficient around TAG*

Particle beam attenuation coefficient for sites near TAG.

4.5 Discussion

4.5.1 Controls on Scavenging Surrounding the Axial Valley

As the distribution of particles is a primary control of scavenging intensity, the dispersal of Fe/Mn-rich particles from hydrothermal vents is a probable driver for ^{230}Th and ^{231}Pa distributions surrounding the axial valley. Until recently, it was thought that Fe from hydrothermal plumes rapidly precipitates and settles at relatively short distance from the vent site. For example, the residence time of Fe^{2+} at TAG is 1 – 130 min and at Rainbow is 20 – 160 min (González-Santana et al., 2021) and about 80% of plume dFe forms large particulates that settle within 10 km (Lough et al., 2023). However, some dFe

is stable as colloidal phases within plume waters during transport for over 6 months (Tagliabue et al., 2022). Lagrangian particle dispersion models for the Lucky Strike hydrothermal field, located just south of Menez Gwen, suggest that plume particles take about 30 days to exit the ridge valley, covering about 100 km from the center of the valley to the ridge flank (Lough et al., 2023; Vic et al., 2018). The timescales are roughly similar for dFe modeled at TAG, taking around 30 – 60 days to exit the valley wall and at least 150 days to reach station 28 at 250 km west of the vent site (Tagliabue et al., 2022). Although these are geologically short processes, their effects on trace metal distributions are much longer lived. Depletions of ^{230}Th and ^{231}Pa will persist for potentially decades to hundreds of years, only growing back in due to the effects of particle rain or mixing with seawater, corresponding with their respective residence times. The distribution of ^{230}Th and ^{231}Pa at the stations surrounding Rainbow and TAG can generally be described by a combination of particle dispersal time and progressive mixing with seawater. Generally, we see scavenged distributions of these elements within the plume water at the vent sites (stations 16 and 35). Sites within the axial valley (stations 14, 15, 18, 26, 27, and 36) have particle dispersal times <60 days. At Rainbow, these axial valley sites show ^{230}Th and ^{231}Pa distributions with a mixture of depths that are as depleted as the vent site and are similar to the reference profile. These distributions are consistent with short particle dispersal times where mixing of the plume water with surrounding seawater is incomplete and relatively heterogeneous. Compared to the sites in the axial valley next to TAG, where particle dispersal times are roughly doubled, the distributions of ^{230}Th and ^{231}Pa at these sites are slightly less depleted than at the vent site and the depth of depletion is slightly expanded. This is consistent with slightly longer mixing times at

TAG, which causes water to be more homogeneous. The timeframe of water from vent sites to stations outside of the axial valley (stations 12, 13, 30, and 31) is on the scale of months. The distribution of ^{230}Th and ^{231}Pa at these stations is depleted only a small degree from reference profiles (the exception being ^{231}Pa at TAG, discussed below) and these depletions occur over a km above and below the original vent water. This is consistent with topographically induced mixing of vent and seawater over months and is likely representative of depleted water that enters the greater Atlantic. The particle beam attenuation coefficient from stations inside and outside of the axial valley surround TAG and Rainbow are elevated near plume depths compared with stations 250 km away, which is evidence that *in-situ* scavenging is still occurring at these sites (Fig. 4.11 and 4.13) and potentially evidences that scavenging by hydrothermal particles might be a factor is trace metal distribution far from vent sites. The depletion of ^{231}Pa stations outside of the axial valley at TAG is unique as it is significantly more depleted than ^{230}Th concentrations. There are two possible explanations for this disconnect between the scavenging of both trace metals. One can be related to the difference in the effects by different particle phases. While all hydrothermal particles strongly scavenge Th and Pa, Th has a greater affinity to Fe-rich phases whereas Pa is more strongly scavenged by Mn-rich phases (Anderson et al., 1983; Hayes, et al., 2015b). It is possible that the composition of particulate phases is different at distal sites than at the vent site, as Mn phases have been proposed to persist in hydrothermal plumes longer than Fe (Mottl & McConachy, 1990; Trocine & Trefry, 1988). Stations 30 and 31, roughly ~30 km from the vent, may be subject to more developed plume water and have comparatively enriched in Mn and thereby a stronger sink of ^{231}Pa. A second explanation for this

disconnect is that the bottom water of the axial valley is scavenged not just by active particle plumes, but also by the benthic resuspension of these particles. This process may preferentially draw down more ^{231}Pa, but is generally difficult to distinguish from hydrothermal scavenging by plume water. There is also the question of the spatial extent of this resuspension, if it occurs at all, in that stations outside of the axial valley around Rainbow do not seem to indicate bottom suspension. This means that additional drawdown of ^{231}Pa by benthic particles might be a localized feature based in part by the topography of the axial valley.

We observed that the Hayes Fracture Zone (21), S-OH1 (20), and the TAG Valley Wall (37) have nearly homogenous sections of low ^{230}Th and ^{231}Pa that are up to 2000 m removed from the depth of active hydrothermal plumes, which implies that these profiles are generally well mixed throughout these depths. Transmissometer data from TAG Valley Wall is nearly indistinguishable from the upper water column of TAG (35); however, ^{230}Th and ^{231}Pa concentrations along the valley wall were on the same scale as those from the stations north and south of TAG, but up to 1000 m shallower in depth. While initially this looks like it can be explained by the same particle dispersal mechanism as the TAG stations inside of the axial valley, the distribution of elements at TAG between 2 – 3 km depth is almost the same as the reference profile, whereas the valley wall is highly depleted. Invoking the same type of dispersal would imply the vertical mixing of the non-buoyant plume water over 1 km vertically over the distance of ~7 km. It also begs the question as to why this vertical/ topographic mixing does not occur over the actual vent site as well. The same processes we invoke to explain the distribution of ^{231}Pa at stations east and west of TAG are potentially in play in regard to

the distribution at the valley wall. The Hayes Fracture Zone and S-OH1 show somewhat homogeneous distributions of Th and Pa which are scavenged with respect to a reference profile. Both stations seemingly have low hydrothermal particle concentrations, with Cp values similar to those of stations far off axis of TAG (not shown in this study), which leads us to believe that these signals are primarily laterally advected from plume dispersal located elsewhere in the ridge.

The combination of element depletion and the appearance of some homogeneity in element distribution implies a degree of strong zone of mixing of depleted plume water with seawater. For example, the Hayes Fracture Zone transform fault forms an inlet for seawater into the axial valley, which depleted hydrothermal water could be funneled into. The mixing of waters at the Hayes Fracture Zone appears to be better integrated than "younger" stations like the ones surrounding Rainbow who also show evidence of mixing, but have significant variations with depth. The mesoscale (10 – 100 km) dynamics of mixing between plume water with seawater ultimately appear to be complicated, however are an integral part in understanding how particles and depletion of some trace metals are carried into the western Atlantic. We propose that future work be done with shorter lived radiotracers, such as ^{228}Th or ^{234}Th, to calculate mixing fractions at various stages of particle dispersal in order to understand how the effects of multiple vents are integrated at the basin-scale.

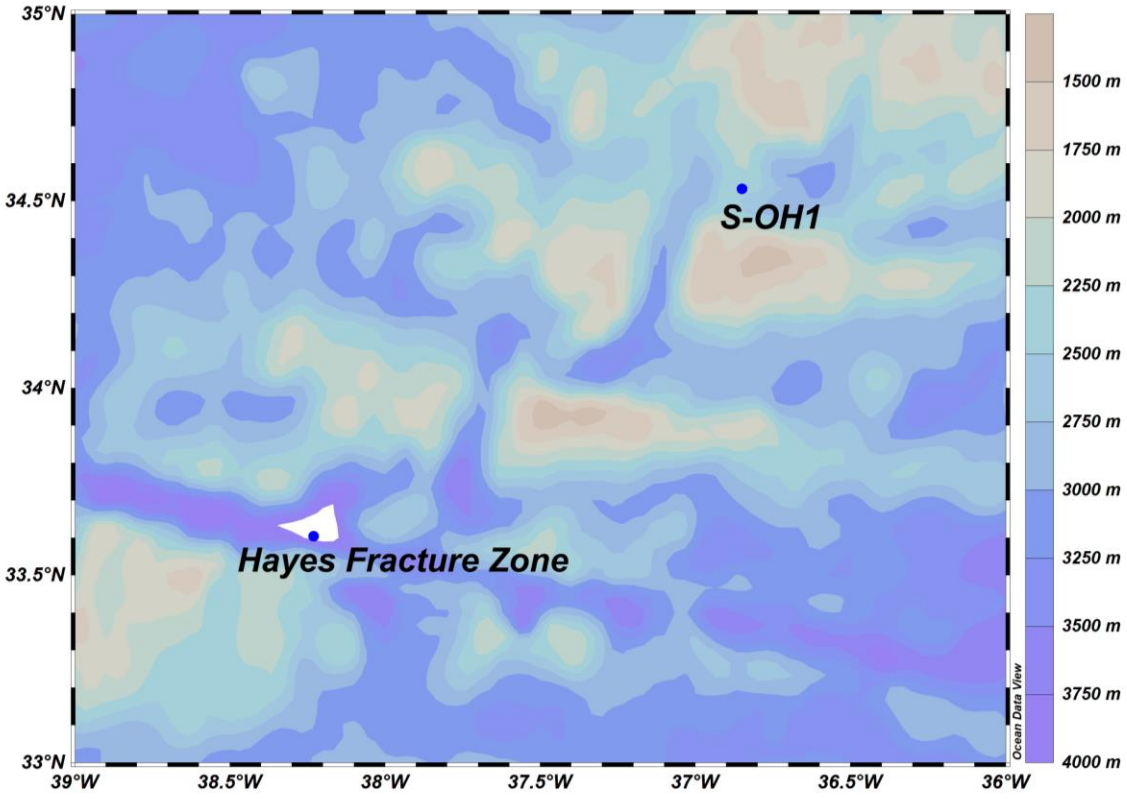

Figure 4.14 *Bathymetry around inactive vents*

Bathymetric features surrounding inactive location S-OH1 and the Hayes Fracture Zone, located within the transform fault.

4.5.2 Expanding Hydrothermal Scavenging to Basin-Scale Budgets

Global ocean measurements of ^{230}Th and ^{231}Pa are relatively sparse and more data is needed to accurately reflect the budgets of these elements and the environmental processes that drive trace metal scavenging. To this regard, recent efforts have focused on modeling the distribution of these radioisotopes, and thereby their scavenging and burial to sediment, using a combination of simple particle proxies and circulation modeling (Plancherel et al., 2016). This issue is in part a result of the effort required to sample dissolved and particulate Th and Pa and other factors for scavenging like particle composition or atmospheric dust flux. The general idea is that existing Th and Pa datasets

can be paired with complimentary data that are cheaper and easier to take during cruises (e.g., sensor data), using them to inform a global distribution model, and opening sampling efforts to areas that specifically need better constraint. For example, compiled global transmissometer data, such as Gardner et al., 2018, is a promising archive of particle effects and is useful in identifying multiple processes that affect scavenging intensity, including the effect of nepheloid layers. However, particle concentration alone is not enough and this data must be coupled with information about the particulate composition and circulation effects to adequately predict distributions. Efforts to "simplify" other scavenging parameters can also be done, such as determination of particle composition by cross-polarizing beam to identify the relative composition of particulate inorganic carbon (Bishop et al., 2022). Problems in these models might arise where the distributions of Th and Pa are not directly correlated with particle effects such as at the downstream effects of hydrothermal venting or nepheloid layers. Because of this, the effects of hydrothermal or benthic scavenging have not been largely considered in regional models, or their effect has been explored to only a basic degree (Luo et al., 2021; Plancherel et al., 2016; Sasaki et al., 2022). However, even if simple particle data is not totally correlated to scavenging intensity for all instances, it is useful if existing archives of Th and Pa are used to train some of these missing quantities in the model. And to this, we believe future models can parameterize hydrothermal and nepheloid scavenging by using the residual between current model output and real data where these features are identified to parameterize downstream effects. The data presented in this study might be useful in constraining models in various ways. For example, the concentrations of Th and Pa measured inside of the axial valley, when combined with

physical parameters for the dispersal of valley water, can be used to obtain the effective endmember for hydrothermal water off the ridge. This endmember can be further constrained by the concentrations of Th and Pa measured outside of the axial valley wall.

4.6 Conclusion

Despite a somewhat limited sampling strategy for ^{230}Th and ^{231}Pa during GEOTRACES GA13 at Mid-Atlantic Ridge vent sites, we use the novel technique of comparing plume water distributions to historical reference profiles similar in scavenging in biogenic particles to determine the degree of scavenging for these elements. This allowed us to examine how the effects of hydrothermal scavenging disperses to sites outside of the active vent and forms the foundation for how these effects eventually enter into the western Atlantic. We found that the dispersal of hydrothermal particles from active vent site through the ridge was the primary control on the distribution of ^{230}Th and ^{231}Pa throughout and within the axial valley. How signals of low ^{230}Th and ^{231}Pa integrate into surrounding ridge water is dependent on the timescales of plume and seawater mixing and is potentially important in creating a scavenged background of elements at sites where no active vents exist. These findings are potentially useful as model training data and can be used to constrain how heterogeneous ridge segments integrate depleted ^{230}Th and ^{231}Pa signals into the western Atlantic. We recommend that future efforts model the downstream effects of hydrothermal scavenging by training with the difference between current output and measured hydrothermal distributions.

4.7 Works Cited

Albani, S., Mahowald, N. M., Perry, A. T., Scanza, R. A., Zender, C. S., Heavens, N. G., Maggi, V., Kok, J. F., & Otto-Bliesner, B. L. (2015). Improved dust representation in the Community Atmosphere Model. *Journal of Advances in Modeling Earth Systems*, *6*(3), 541–570. https://doi.org/10.1002/2013MS000279

Andersen, M. B., Stirling, C. H., Zimmermann, B., & Halliday, A. N. (2010). Precise determination of the open ocean 234U/238U composition. *Geochemistry, Geophysics, Geosystems*, *11*(12). https://doi.org/10.1029/2010GC003318

Anderson, R. F. (2019). *GEOTRACES: Accelerating Research on the Marine Biogeochemical Cycles of Trace Elements and Their Isotopes*. https://doi.org/10.1146/annurev-marine-010318

Anderson, R. F., Bacon, M. P., & Brewer, P. G. (1983). Removal of 230Th and 231Pa from the open ocean. *Earth and Planetary Science Letters*, *62*(1), 7–23.

Anderson, R. F., Cheng, H., Edwards, R. L., Fleisher, M. Q., Hayes, C. T., Huang, K. F., Kadko, D., Lam, P. J., Landing, W. M., Lao, Y., Lu, Y., Measures, C. I., Moran, S. B., Morton, P. L., Ohnemus, D. C., Robinson, L. F., & Shelley, R. U. (2016). How well can we quantify dust deposition to the ocean? *Philosophical Transactions of the Royal Society A: Mathematical, Physical and Engineering Sciences*, *374*(2081). https://doi.org/10.1098/rsta.2015.0285

Anderson, R. F., Fleisher, M. Q., Robinson, L. F., Edwards, R. L., Hoff, J. A., Moran, S. B., van der Loeff, M. R., Thomas, A. L., Roy-Barman, M., & Francois, R. (2012). GEOTRACES intercalibration of 230th, 232Th, 231Pa, and prospects: For10be.

Limnology and Oceanography: Methods, *10*(APRIL), 179–213. https://doi.org/10.4319/lom.2012.10.179

Auro, M. E., Robinson, L. F., Burke, A., Bradtmiller, L. I., Fleisher, M. Q., & Anderson, R. F. (2012). Improvements to 232-thorium, 230-thorium, and 231-protactinium analysis in seawater arising from GEOTRACES intercalibration. *Limnology and Oceanography: Methods*, *10*(JULY), 464–474. https://doi.org/10.4319/lom.2012.10.464

Bacon, M. P., & Anderson, R. F. (1982). Distribution of Thorium Isotopes Between Dissolved and Particulate Forms in The Deep Sea. *Journal of Geophysical Research*, *87*(1), 2045–2056. https://doi.org/10.1029/JC087iC03p02045

Bideau, D., Hékinian, R., Sichler, B., Gràcia, E., Bollinger, C., Constantin, M., & Guivel, C. (1998). Contrasting volcanic-tectonic processes during the past 2 Ma on the Mid-Atlantic Ridge: Submersible mapping, petrological and magnetic results at lat. 34°52' N and 33°55' N. *Marine Geophysical Research*, *20*(5), 425–458. https://doi.org/10.1023/A:1004760111160

Bishop, J. (1999). Transmissometer measurement of POC. *Deep Sea Research Part 1: Oceanographic Research Papers*, *46*(2), 353–369.

Bishop, J. K. B., Amaral, V. J., Lam, P. J., Wood, T. J., Lee, J.-M., Laubach, A., Barnard, A., Derr, A., & Orrico, C. (2022). Transmitted Cross-Polarized Light Detection of Particulate Inorganic Carbon Concentrations and Fluxes in the Ocean Water Column: Ships to ARGO Floats. *Frontiers in Remote Sensing*, *3*. https://doi.org/10.3389/frsen.2022.837938

Bishop, J. K. B., & Wood, T. J. (2008). Particulate matter chemistry and dynamics in the

twilight zone at VERTIGO ALOHA and K2 sites. *Deep Sea Research Part I: Oceanographic Research Papers*, *55*(12), 1684–1706.

Cheng, H., Lawrence Edwards, R., Shen, C. C., Polyak, V. J., Asmerom, Y., Woodhead, J., Hellstrom, J., Wang, Y., Kong, X., Spötl, C., Wang, X., & Calvin Alexander, E. (2013). Improvements in 230Th dating, 230Th and 234U half-life values, and U-Th isotopic measurements by multi-collector inductively coupled plasma mass spectrometry. *Earth and Planetary Science Letters*, *371–372*, 82–91. https://doi.org/10.1016/j.epsl.2013.04.006

Cochran, J. K., Livingston, H. D., Hirschberg, D. J., & Surprenant, L. D. (1987). Natural and anthropogenic radionuclide distributions in the northwest Atlantic Ocean. *Earth and Planetary Science Letters*, *84*(2–3), 135–152.

Costa, K. M., Hayes, C. T., Anderson, R. F., Pavia, F. J., Bausch, A., Deng, F., Dutay, J. C., Geibert, W., Heinze, C., Henderson, G., Hillaire-Marcel, C., Hoffmann, S., Jaccard, S. L., Jacobel, A. W., Kienast, S. S., Kipp, L., Lerner, P., Lippold, J., Lund, D., Zhou, Y. (2020). 230Th Normalization: New Insights on an Essential Tool for Quantifying Sedimentary Fluxes in the Modern and Quaternary Ocean. *Paleoceanography and Paleoclimatology*, *35*(2), 1–36. https://doi.org/10.1029/2019PA003820

Delanghe, D., Bard, E., & Hamelin, B. (2002). New TIMS constraints on the uranium-238and uranium-234 in seawaters from the main ocean basins and the Mediterranean Sea. *Marine Chemistry*, *80*, 79–93.

Deng, F., Thomas, A. L., Rijkenberg, M. J. A., & Henderson, G. M. (2014). Controls on

seawater 231Pa, 230Th and 232Th concentrations along the flow paths of deep waters in the Southwest Atlantic. *Earth and Planetary Science Letters*, *390*, 93–102.

DeVries, T., & Weber, T. (2017). The export and fate of organic matter in the ocean: New constraints from combining satellite and oceanographic tracer observations. *Global Biogeochemical Cycles*, *31*(3), 535–555. https://doi.org/10.1002/2016GB005551

Feden, R. H., Fleming, H. S., Perry, R. K., & Phillips, J. D. (1975). The Mid-Atlantic Ridge at 33°N: the Hayes Fracture Zone. *Earth and Planetary Science Letters*, *26*(3), 292–298.

Fitzsimmons, J. N., Boyle, E. A., & Jenkins, W. J. (2014). Distal transport of dissolved hydrothermal iron in the deep South Pacific Ocean. *Proceedings of the National Academy of Sciences of the United States of America*, *111*(47), 16654–16661. https://doi.org/10.1073/pnas.1418778111

Fouquet, Y., Charlou, J., Donval, J., Radford-Knoery, J., Pelle, P., Ondreas, H., Lourenco, N., Segonac, M., & Tivey, M. (1994). A detailed study of the Lucky-Strike hydrothermal site and discovery of a new hydrothermal site: « Menez-Gwen ». Preliminary results of DIVA 1 cruise (5-29 May, 1994). *Inter-Ridge News*, *3*(2), 14–17.

Gardner, W. D., Mishonov, A. V., & Richardson, M. J. (2006). Global POC concentrations from in-situ satellite data. *Deep Sea Research II: Topical Studies in Oceanography*, *53*(5–7), 718–740.

Gardner, W. D., Richardson, M. J., Mishonov, A. V., & Biscaye, P. E. (2018). Global

comparison of benthic nepheloid layers based on 52 years of nephelometer and transmissometer measurements. *Progress in Oceanography*, *168*, 100–111. https://doi.org/10.1016/j.pocean.2018.09.008

Gardner, W. D., Southard, J. B., & Hollister, C. D. (1985). Sedimentation, resuspension and chemistry of particles in the northwest Atlantic. *Marine Geology*, *65*(3–4), 199–242.

German, C. R., Campbell, A. C., & Edmond, J. M. (1991). Hydrothermal scavenging at the Mid-Atlantic Ridge: Modification of trace element dissolved fluxes. *Earth and Planetary Science Letters*, *107*(1), 101–104.

German, C. R., Fleer, A. P., Bacon, M. P., & Edmond, J. M. (1991). Hydrothermal scavenging at the Mid-Atlantic Ridge" radionuclide distributions. In *Earth and Planetary Science Letters* (Vol. 105).

German, C. R., Klinkhammer, G. P., Edmond, J. M., Mitra, A., & Elderfield, H. (1990). Hydrothermal scavenging of rare-earth elements in the ocean. *Nature*, *345*, 516–518.

German, C. R., Thurnherr, A. M., Knoery, J., Charlou, J. L., Jean-Baptiste, P., & Edmonds, H. N. (2010). Heat, volume and chemical fluxes from submarine venting: A synthesis of results from the Rainbow hydrothermal field, 36°N MAR. *Deep-Sea Research Part I: Oceanographic Research Papers*, *57*(4), 518–527. https://doi.org/10.1016/j.dsr.2009.12.011

González-Santana, D., González-Dávila, M., Lohan, M. C., Artigue, L., Planquette, H., Sarthou, G., Tagliabue, A., & Santana-Casiano, J. M. (2021). Variability in iron (II) oxidation kinetics across diverse hydrothermal sites on the northern Mid

Atlantic Ridge. *Geochimica et Cosmochimica Acta*, *297*, 143–157. https://doi.org/10.1016/j.gca.2021.01.013

Gràcia, E., Luc Charlou, J., Radford-Knoery, J., & Parson, L. M. (2000). *Non-transform offsets along the Mid-Atlantic Ridge south of the Azores (38°N - 34°N): ultramafic exposures and hosting of hydrothermal vents*. www.elsevier.com/locate/epsl

Hayes, C. T., Anderson, R. F., Fleisher, M. Q., Huang, K. F., Robinson, L. F., Lu, Y., Cheng, H., Edwards, R. L., & Moran, S. B. (2015). 230Th and 231Pa on GEOTRACES GA03, the U.S. GEOTRACES North Atlantic transect, and implications for modern and paleoceanographic chemical fluxes. *Deep-Sea Research Part II: Topical Studies in Oceanography*, *116*, 29–41. https://doi.org/10.1016/j.dsr2.2014.07.007

Hayes, C. T., Anderson, R. F., Fleisher, M. Q., Vivancos, S. M., Lam, P. J., Ohnemus, D. C., Huang, K. F., Robinson, L. F., Lu, Y., Cheng, H., Edwards, R. L., & Moran, S. B. (2015). Intensity of Th and Pa scavenging partitioned by particle chemistry in the North Atlantic Ocean. *Marine Chemistry*, *170*, 49–60. https://doi.org/10.1016/j.marchem.2015.01.006

Hayes, C. T., Fitzsimmons, J. N., Boyle, E. A., McGee, D., Anderson, R. F., Weisend, R., & Morton, P. L. (2015). Thorium isotopes tracing the iron cycle at the Hawaii Ocean Time-series Station ALOHA. *Geochimica et Cosmochimica Acta*, *169*, 1–16. https://doi.org/10.1016/j.gca.2015.07.019

Hayes, C. T., & Wallace, D. J. (2019). Exploring records of Saharan dust transport and

hurricanes in the western North Atlantic over the Holocene. In *Quaternary Science Reviews* (Vol. 205, pp. 1–9). Elsevier Ltd. https://doi.org/10.1016/j.quascirev.2018.11.018

Henderson, G. M., & Anderson, R. F. (2003). The U-series toolbox for paleoceanography. *Uranium-Series Geochemistry*, *52*, 493–531. https://doi.org/10.2113/0520493

James, R. H., Elderfield, H., & Palmer, M. R. (1995). The chemistry of hydrothermal fluids from the Broken Spur site, 29"N Mid-Atlantic Ridge. In *Geochimlca et Cosmochimica Acta* (Vol. 59, Issue 4).

Jickells, T. D., An, Z. S., Andersen, K. K., Baker, A. R., Bergametti, G., Brooks, N., Cao, J. J., Boyd, P. W., Duce, R. A., Hunter, K. A., Kawahata, H., Kubilay, N., Laroche, J., Liss, P. S., Mahowald, N., Prospero, J. M., Ridgwell, A. J., Tegen, I., & Torres, R. (n.d.). *Global Iron Connections Between Desert Dust, Ocean Biogeochemistry, and Climate*. https://www.science.org

Kelley, D. S., Früh-Green, G. L., Karson, J. A., & Ludwig, K. A. (2007). The Lost City Hydrothermal Field Revisited. *Source: Oceanography*, *20*(4), 90–99. https://doi.org/10.2307/24860149

Kelley, D. S., Karson, J. A., Früh-Green, G. L., Yoerger, D. R., Shank, T. M., Butterfield, D. A., Hayes, J. M., Schrenk, M. O., Olson, E. J., Proskurowski, G., Jakuba, M., Bradley, A., Larson, B., Ludwig, K., Glickson, D., Buckman, K., Bradley, A. S., Brazelton, W. J., Roe, K., … Sylva, S. P. (2005). A serpentinite-hosted ecosystem: the Lost City hydrothermal field. *Science*, *307*(5714), 1428–1434.

Khatiwala, S., Primeau, F., & Holzer, M. (2012). Ventilation of the deep ocean

constrained with tracer observations and implications for radiocarbon estimates of ideal mean age. *Earth and Planetary Science Letters*, *325–326*, 116–125. https://doi.org/10.1016/j.epsl.2012.01.038

Klischies, M., Petersen, S., & Devey, C. W. (2019). Geological mapping of the Menez Gwen segment at 37°50′N on the Mid-Atlantic Ridge: Implications for accretion mechanisms and associated hydrothermal activity at slow-spreading mid-ocean ridges. *Marine Geology*, *412*, 107–122. https://doi.org/10.1016/j.margeo.2019.03.012

Lopez, G. I., Marcantonio, F., Lyle, M., & Lynch-Stieglitz, J. (2015). Dissolved and particulate 230Th-232Th in the Central Equatorial Pacific Ocean: Evidence for far-field transport of the East Pacific Rise hydrothermal plume. *Earth and Planetary Science Letters*, *431*, 87–95. https://doi.org/10.1016/j.epsl.2015.09.019

Lough, A. J. M., Tagliabue, A., Demasy, C., Resing, J. A., Mellett, T., Wyatt, N. J., & Lohan, M. C. (2023). Tracing differences in iron supply to the Mid-Atlantic Ridge valley between hydrothermal vent sites: implications for the addition of iron to the deep ocean. *Biogeosciences*, *20*(2), 405–420. https://doi.org/10.5194/bg-20-405-2023

Luo, C., Mahowald, N. M., & del Corral, J. (2003). Sensitivity study of meteorological parameters on mineral aerosol mobilization, transport, and distribution. *Journal of Geophysical Research: Atmospheres*, *108*(15). https://doi.org/10.1029/2003jd003483

Luo, Y. (2017). Reinterpretation of oceanic 230 Th profiles based on decadal export

productivity (2003-2010). *Scientific Reports*, *7*(1). https://doi.org/10.1038/s41598-017-00604-y

Luo, Y., Francois, R., & Allen, S. E. (2010). Sediment 231 Pa/ 230 Th as a recorder of the rate of the Atlantic meridional overturning circulation: insights from a 2-D model. In *Ocean Sci* (Vol. 6). www.ocean-sci.net/6/381/2010/

Luo, Y., Lippold, J., Allen, S. E., Tjiputra, J., Jaccard, S. L., & Francois, R. (2021). The influence of deep water circulation on the distribution of 231Pa and 230Th in the Pacific Ocean. *Earth and Planetary Science Letters*, *554*. https://doi.org/10.1016/j.epsl.2020.116674

Lupton, J. E., & Craig, H. (1981). A Major Helium-3 Source at 15°S on the East Pacific Rise. *Science*, *214*(4516), 13–18.

Lupton, J. E., Delaney, J. R., Johnson, H. P., & Tivey, M. K. (1985). Entrainment and vertical transport of deep ocean water by buoyant hydrothermal plumes. *Nature*, *316*, 621–623.

Mahowald, N. M., Baker, A. R., Bergametti, G., Brooks, N., Duce, R. A., Jickells, T. D., Kubilay, N., Prospero, J. M., & Tegen, I. (2005). Atmospheric global dust cycle and iron inputs to the ocean. In *Global Biogeochemical Cycles* (Vol. 19, Issue 4). https://doi.org/10.1029/2004GB002402

Moran, S. B., Charette, M. A., Hoff ', J. A., Edwards, R. L., & Landihg ' A, W. M. (1997). EPSL Distribution of 230Th in the Labrador Sea and its relation ito ventilation. In *Earth and Planetary Science Letters* (Vol. 50).

Mottl, M. J., & McConachy, T. F. (1990). Chemical processes in buoyant hydrothermal

plumes on the East Pacific Rise near 21°N. *Geochemica et Cosmochimica Acta*, *54*(7), 1911–1927.

Pavia, F. J., Anderson, R., Vivancos, S., Fleisher, M., Lam, P., Lu, Y., Cheng, H., Zhang, P., & Lawrence Edwards, R. (2018). Intense hydrothermal scavenging of 230Th and 231Pa in the deep Southeast Pacific. *Marine Chemistry*, *201*(April 2017), 212–228. https://doi.org/10.1016/j.marchem.2017.08.003

Plancherel, Y., Basak, C., & Khatiwala, S. (2016). The influence of nepheloid layers on global model simulations of 231Pa and 230Th. *AGU Fall Meeting 2016*.

Reid, J. L. (1994). *On the total geostrophic circulation of the North Atlantic Ocean: Flow patterns, tracers, and transports* (Vol. 33).

Robert, J., Miranda, C. F., & Muxart, R. (1969). Mesure de la periode du protactinium-231 par microcalorimetrie. *Radiochimica Acta*, *11*, 104–108.

Robinson, L. F., Belshaw, N. S., & Henderson, G. M. (2004). U and Th concentrations and isotope ratios in modern carbonates and waters from the Bahamas. *Geochimica et Cosmochimica Acta*, *68*(8), 1777–1789. https://doi.org/10.1016/j.gca.2003.10.005

Rona, P. A., Bogdanov, Y. A., Gurvich, E. G., Rimski-Korsakov, N. A., Sagalevich, A., Hannington, M. D., & Thompson, G. (1993). Relict hydrothermal zones in the TAG hydrothermal field, Mid- Atlantic Ridge 26°N, 45°W. *Journal of Geophysical Research*, *98*(B6), 9715–9730. https://doi.org/10.1029/93JB00552

Rutgers Van Der Loeff, M. M., & Berger~, G. W. (1993). Scavenging of 23°Th and 231pa near the Antarctic Polar Front in the South Atlantic. In *Deep-Sea Research* (Vol. 1, Issue 2).

Sasaki, Y., Kobayashi, H., & Oka, A. (2022). Global simulation of dissolved 231Pa and 230Th in the ocean and the sedimentary 231Pa⁄230Th ratios with the ocean general circulation model COCO ver4.0. *Geoscience Model Development*, *15*(5), 2013–2033.

Stuart, F. M., Turner, G., Duckworth, R. C., & Fallick, A. E. (1994). Helium isotopes as tracers of trapped hydrothermal fluids in ocean-floor sulfides. *Geology*, *22*(9), 823–829.

Tagliabue, A., Lough, A. J. M., Vic, C., Roussenov, V., Gula, J., Lohan, M. C., Resing, J. A., & Williams, R. G. (2022). Mechanisms Driving the Dispersal of Hydrothermal Iron From the Northern Mid Atlantic Ridge. *Geophysical Research Letters*, *49*(22). https://doi.org/10.1029/2022GL100615

Trocine, R. P., & Trefry, J. H. (1988). Distribution and chemistry of suspended particles from an active hydrothermal vent site on the Mid-Atlantic Ridge at 26°N. *Earth and Planetary Science Letters*, *88*(1–2), 1–15.

Vic, C., Gula, J., Roullet, G., & Pradillon, F. (2018). Dispersion of deep-sea hydrothermal vent effluents and larvae by submesoscale and tidal currents. *Deep-Sea Research Part I: Oceanographic Research Papers*, *133*, 1–18. https://doi.org/10.1016/j.dsr.2018.01.001

Weyer, S., Anbar, A. D., Gerdes, A., Gordon, G. W., Algeo, T. J., & Boyle, E. A. (2008). Natural fractionation of 238U/235U. *Geochimica et Cosmochimica Acta*, *72*, 345–359.

4.8 Supplemental Material

TM Cast No.	Transmittance correction (%)
7	-1.47
9	-1.55
10	-1.43
11, 20, 23, 27	-1.35
13	-1.24
14	-1.26
17, 18	-1.302
25	-1.32
29, 31	-1.312
34	-0.726
36	-0.87
38	+1.899
40	+0.7
43	-0.16
45	-0.82
46	-0.939
48	-1.055
50	-1.12
51	-1.12
53	-1.108
55	-0.821
57	-0.97
59	+2.567
61	+1.563
63	+1.354
65	+1.227
68	+1.206
70	+1.61
71	+1.427
73	+1.191
76, 78, 80	+0.96
83	+0.84

Table 4.1 *Correction for trace metal rosette casts transmittance*

Correction for trace metal rosette casts transmittance.

CHAPTER V – CONCLUSIONS AND FRAMEWORK FOR FUTURE STUDY OF HYDROTHERMAL SCAVENGING

5.1 Conclusions

Although the conclusions from Chapter 2 are reasonably standalone, we find that follow up is required to synthesize the conclusions from Chapters 3 and 4. In this synthesis, we focus on future efforts and community strategies to better understand Th and Pa cycling as learned through these studies.

5.1.1 Synthesizing Th and Pa Cycling using Models

One of the primary goals of programs like GEOTRACES is to address the growing community need to synthesize trace element distributions, budgets, and processes at the global level (Anderson, 2019). As discussed in Chapter 4, the scarcity and complexity of sampling dissolved and particulate Th and Pa necessitate new sampling strategies and the incorporation of other data sets in order to synthesize what we know about each element's global cycling. Generally, modeling the distribution of Th and Pa distributions can be done using a combination of physical parameters (decay, reversible scavenging, circulation, and dispersal) and particle parameters (concentration and composition) (Plancherel et al., 2016). For the most part, this type of general model is useful for basin dynamics; however, they struggle to capture certain features such as nepheloid layers and hydrothermal plumes (Luo et al., 2010). The main goal of the Th/Pa scavenging community should be to create a generalized model, use existing Th/Pa and tertiary data to parameterize scavenging processes, and target future studies for creating a better learning set. A general list of strategies might be as follows:

(1) Continue higher resolution cruise sampling where possible, such as through the GEOTRACES program.

(2) Development of new sampling methods for different scales, for example, using Remotely Operated Vehicles (ROVs) to remotely target shallow or specific features without needing water column measurements.

(3) Identification of sensor data useful for particle parameterization.

(4) Collecting/compiling/application of sensor data and connecting it with Th/Pa through models

(5) Target future samples specifically for model input

5.1.2 Remotely Operated Vehicles, Unmanned Floats, and Sensor Data

The broad concepts learned by cruise-based sampling can be applied to developing smaller scale, cheaper, or more targeted sampling strategies. For example, unmanned and autonomous vehicles are currently underutilized in the marine particle scavenging space. Sampling of Th and Pa has historically been done using depth profiles; however, as the distribution of Th and Pa in the open ocean is primarily an integration of multi-year timescales, the use of autonomous vehicles and Lagrangian floats should capture similar information at any given location. Conceptually, the main goal of incorporating unmanned vehicles is to capitalize on where they can be easier or an improvement from cruise-based pumping. One of these niches is in scenarios where general context for scavenging is already established and the rest of the water column does not need to be measured, but details within a certain feature of the water column are unknown. A current limitation of this technology is that autonomous floats do not generally have the operational range to study many features of scavenging. For example,

Argo floats are not designed to work below 2000 m, which is shallower than needed to categorize many scavenging effects. More recent programs like Deep Argo, are making floats that operate to ~4000 m which means that the technology to close this gap may come soon (Gasparin et al., 2020).

ROVs are also appealing in that they may be designed and outfitted with both a system to directly measure Th/Pa and have tertiary sensors for particle analysis. For example, it is not unreasonable that unmanned crafts be equipped with an *in-situ* pumping system and/or sensors that are also useful in the context of scavenging. For example, an optical/ scattering sensor may show relative changes in particle concentration or chemical composition. A filtration system might be designed/implemented so that ~200 L worth of particulates from seawater are collected through a filter, replaced, and then sent to temporary storage. Even a low sample capacity (~30) is particularly useful as the goal will not be to establish high resolution profiles, but to target and track changes within individual features. The downside is that many ROV's are operated while tethered to a ship, which in many cases overrides many benefits it may have over pumping with a CTD rosette. The benefit of using a tethered ROV is probably more of a question of scale. For example, an ROV and smaller vessel might be suited to measure Th/Pa distributions leaving the continental shelf or at areas with submarine volcanism. The small scale of maneuverability might be useful in areas where there are large vertical changes to scavenging, such as offsetting the differences between CTD rosette casts of a hydrothermal plume. This ultimately means that the most useful information unmanned craft can give us about basin-wide scavenging features will likely be (1) autonomous to some degree and (2) based on optical sensors and other scavenging proxies instead of

measuring Th or Pa concentrations directly. Floats solve this problem to some degree but they have their own caveats. Generally, floats have limited sensor capacity and can only control buoyancy, meaning they are useful in cases where there is a need to measure "down-stream". The loadout of a float may not be as useful as a larger ROV, so floats would require specific design choices to make them useful for proxying particle concentration and composition. Specifically for basin-scale hydrothermal scavenging and potentially other features like nepheloid layers, float-based sampling might help to characterize the spatial extent of plume influence since other parameters can establish "baseline" scavenging conditions in the upper water column. Unmanned vehicles of any kind are unlikely to replace cruise-based sampling; however, might be useful supplements with studies that are smaller in scale or to gather an archive of passive supplementary data. While sampling design can accommodate specialized use of an ROV/float that is useful to filling in gaps for Th/Pa distribution, this will more likely be useful on small scales. For basin-scale efforts, we recommend that optical sensors can be put on ROVs/casts as a supplementary feature that would ultimately help the study of scavenging less directly.

5.1.3 Application of Tertiary and Sensor Data

Chapter 4 discusses the potential application and use for certain instrumentations, such as transmissometer measurements, as important factors in helping to determine Th and Pa distribution where there is currently no data. These tertiary data sets are important for informing our general model and are potentially useful in identifying certain processes, like nepheloid layers, which can be the basis for a targeted study. This dissertation looked for specific relationships between ^{230}Th and ^{231}Pa scavenging and

dFe, He isotopes, and transmittance that would be useful to predict ^{230}Th and ^{231}Pa distributions due to hydrothermal influence at different scales (Chapters 3 vs Chapter 4). Near the Mid-Atlantic Ridge we found that although higher dFe and ^{3}He/^{4}He were often observed within hydrothermal depths with high Cp, these factors were not always present wherever ^{230}Th and ^{231}Pa were depleted. This in part can be explained by variations in sampling casts, but more likely is evidence that, although these metrics are proxies for hydrothermal influence in seawater, they do not necessarily act as a proxy for the presence of hydrothermal particles that cause scavenging. There was a relatively similar story far from the plume in the equatorial Pacific. There was no direct correlation between δ^{3}He and the concentration of ^{230}Th or ^{231}Pa; however, the highest δ^{3}He values were useful in identifying the where distributions of scavenged elements began to diverge. At GP16, there was a relationship between He and depletion of ^{230}Th and ^{231}Pa at the hydrothermal plume depth; however, the reason our data seems to differ is that, at GP15 where we also looked outside of the plume, the processes that control He (advection and conservative mixing) are not the same that control ^{230}Th and ^{231}Pa distribution (particle dynamics). Both Chapters 3 and 4 show that the relationship between hydrothermal plumes and their relationship to scavenging can be contextual, which is ultimately problematic when using them to parameterize hydrothermal scavenging in a global model. We recommend that in these cases where supplementary data sets cannot adequately predict Th and Pa scavenging, future efforts should focus on taking samples where features like hydrothermal or nepheloid influence can be constrained. These observations can ultimately be used with a general model as a learning set to parameterize these other scavenging processes.

5.1.4 Targeting Future Studies for Basin-Scale Hydrothermal Influence

Futures studies should be used to fill gaps in our conceptual model, and for this purpose, we would like to give examples of targeted study locations which would be useful for the parameterization of hydrothermal plumes as basin-scale sinks of Th and Pa. Given the enormous scale of the global mid-ocean ridge system, over 65,000 km, and the significant variability between different spreading centers, we cannot reasonably expect to directly measure the entire system and surrounding basin. However, if we can target sampling to initially train a model to its broad-scale effects and then work to incorporate more variability in further studies.

For the North Atlantic, we have identified three areas for future research that would improve model capability for predicting ^{230}Th and ^{231}Pa distributions. (1) We recommend higher resolution sampling through/within the axial valley and across/perpendicular to it. The primary focus of this would be to understand the dynamics for water mixing in the ridge and how this water ultimately integrates and travels off-ridge. This type of study might allow us to constrain and model variability between ridge segments as it gets incorporated into a regional model. (2) We recommend similar higher resolution sampling across a major transform fault, such as the Hayes Fracture Zone. In addition to potential variability in scavenging at different ridge segments/types, we want to understand how depleted water "leaks" our of the axial valley and into the greater Atlantic. The goal of this sampling would be to determine the mixing and circulation timescales at these locations to see if they provide pathways for integration with the Atlantic. (3) Finally, we recommend further sampling off-axis of the MAR in the western Atlantic. A major problem with understanding potential hydrothermal sink in the Atlantic

is that we have very little constraints for the spatial scale of these effects. The goal of this sampling would be to capture the distal end of this plume (much like GP15 capturing the tail of the EPR plumes) to constrain the northern and western extents of plume water. This could be done by either: a transect traveling off axis of the ridge into the western Atlantic at a location far north of GA03, or a transect parallel to the ridge roughly halfway in the western Atlantic, like has been proposed above with unmanned vehicles.

For the equatorial Pacific, a driving question that still remains the degree of contrast in ^{230}Th concentration, and thereby transport, with proximity to the EPR. Although we expect water close to the EPR to be more depleted, He isotopes may suggest that hydrothermal water tends to perturb farther north close to the ridge before eventually being concentrated by equatorial currents. Although GP15 and JGOFS provide some context for ^{230}Th concentration gradients between plumes and gyres, it would be useful to have another transect farther to the east along the 130° W meridian, from 20° N to 35° S. The reason this specific transect is useful is that it would allow a basin-wide calculation of ^{230}Th gradient within the plume as well as resolve the gradient with the outside gyres. The use for models in this case might not just be to show where variations in ^{230}Th distribution occur, but are potentially useful for constraining regional changes in ^{230}Th transport, which can be impactful on its use as a paleoproxy. An example of a targeted study in this region, collecting a limited number of samples and establishing the background with other techniques, could be done at the EPR plume in the north equatorial Pacific. Our expectations from GP15 (Chapter 3 of this dissertation) and GP16 suggest that, like in the southern equatorial Pacific, this northern plume should have a gradient in Th and Pa concentration, being more deplete near the EPR and increasing in

concentration as you go westward. As we expect the general scavenging background, shown in the upper water column, to be set by biogenic particle flux and relatively invariant along this transect, a float traveling along a density surface within hydrothermally influenced water should be sufficient to capture the changes to Th and Pa concentration over this region and can be directly compared with GP16.

5.1.5 Combining Techniques

The current state of Th and Pa sampling is not enough to entirely constrain the basin-scale processes that define these elements' distribution. Ultimately, the community looks to comprehensively model global distribution of Th and Pa, but some marine processes, such as hydrothermal activity and nepheloid layers, are fairly unconstrained. The scale of these features is potentially too large to capture its variation and effects throughout different basins, creating the need to model these features with a combination of scavenging proxies. With a general distribution model, we might interpret differences between observed data and the model as effects from one of these unmodelled scavenging processes. This gives us the ability to parameterize the effects and to relate these parameters to proxies which may be useful indicators of these effects. The relationship to other scavenging proxies is an important point of follow up because we ideally want to minimize the sampling needed to inform models of this process moving forward. We recommend that future studies look into identifying and parameterizing marine scavenging processes and that the findings from this be used to guide the location of future sampling so that these unmodelled processes can be incorporated into the global Th/Pa budgets.

5.2 Works Cited

Anderson, R. F. (2019). *GEOTRACES: Accelerating Research on the Marine Biogeochemical Cycles of Trace Elements and Their Isotopes*. https://doi.org/10.1146/annurev-marine-010318

Gasparin, F., Hamon, M., Rémy, E., & Le Traon, P. (2020). How Deep Argo Will Improve the Deep Ocean in an Ocean Reanalysis. *Journal of Climate*, *33*(1), 77–94.

Luo, Y., Francois, R., & Allen, S. E. (2010). Sediment 231 Pa/ 230 Th as a recorder of the rate of the Atlantic meridional overturning circulation: insights from a 2-D model. In *Ocean Sci* (Vol. 6). www.ocean-sci.net/6/381/2010/

Plancherel, Y., Basak, C., & Khatiwala, S. (2016). The influence of nepheloid layers on global model simulations of 231Pa and 230Th. *AGU Fall Meeting 2016*.